Imperial College London
Department of Physics

Topological insulator nanoparticles and their photonic analogues

Gleb Siroki

Submitted in part fulfilment of the requirements for the degree of
Doctor of Philosophy in Physics of Imperial College London
and the Diploma of Imperial College London, March 2018

Abstract

The exploration of topological insulators has been a remarkable success of band theory. Topological insulators are distinguished from ordinary ones by the boundary states which exist at the edge of those materials and are robust against disorder. Moreover, for these states the propagation direction depends on the spin in the absence of time-reversal breaking. This makes topological insulators promising candidates for spintronics as well as some optical applications. Because the their unique properties from single-particle band structure the analogous topological phases also exist for photons. Photonic crystals displaying topological properties promise to deliver waveguides where light can be guided without scattering and its direction – controlled by polarization. Following the drive for miniaturization one would like to make use of the described effects at the smallest scale possible. This conserves energy as well as materials and serves as the main motivation for the current work.

The properties of boundary states have been largely explored in infinite (macroscopic) samples but not in finite ones. In the first half of this thesis we study quantum-confined topological nanoparticles. In particular, we use the tight-binding method to show that discrete surface states in the nanoparticles have the same protection from disorder as continuous bands in macroscopic samples. In addition, we analytically show that the surface states strongly affect the optical properties of such nanoparticles compared with those made from ordinary insulators.

The second part of this thesis is devoted to topological photonics. Here we show both analytically and with numerical simulations that confined samples of photonic topological insulators have edge states supporting unidirectional propagation. Furthermore, we explore two designs – a 3D crystal and a 2D metasurface, which display topological properties and have not received any attention in the literature so far.

Copyright declaration

Declaration of originality

Except where otherwise stated, the work contained in this thesis is my own. This thesis has not been submitted in part or in whole for any other award at this or any other university. Parts of this work appear in the following publications:

- Topological photonics: from crystals to particles, G Siroki, P A Huidobro, V Giannini, Physical Review B 96, 041408(R) 2017
- Protection of surface states in topological nanoparticles, G Siroki, P D Haynes, D K K Lee, V Giannini, Physical Review Materials 1, 024201, 2017
- Single electron induced surface plasmons on a topological nanoparticle surface, G Siroki, D K K Lee, P D Haynes, V Giannini, Nature Communicatons 7, 12375, 2016

Contents

List of Tables

List of Figures

Acknowledgements

"Nobody can be anybody without somebodies around"

John A. Wheeler

I am grateful to the founders of the TSM CDT – Adrian Sutton, Peter Haynes and Arash Mostofi. They have worked hard creating and running a program which invests in students and lets them grow professionally and personally. Also, Miranda Smith has always been there to help with administrative questions. Many thanks to Michael Bearpark for mentoring our cohort. Finally, I am grateful to everybody from the cohort six, especially to Iacopo Rovelli, Hikmatyar Hasan, Eduardo Ramos Fernandez for their company, the things we did and holding the line on many occasions. I was lucky to be a part of the CMTH group at the time when it was headed by Matthew Foulkes. The help of Eamonn Murray with computing issues has always been prompt and to the point. On the electronic side, I am thankful to Max Boleininger, Fabiano Corsetti and Michael Rutter for their input. On the photonic side, I am grateful to Paloma Arroyo Huidobro and Yulia Dautova for rewarding collaborations. In addition, I should thank the developers of the open-source codes "MPB" and "MEEP" which were used for numerical studies. Many thanks to Simon Lieu for starting interesting physics discussions during lunch and Marie Rider – for proofreading this thesis and taking the research on topological nanoparticles to a whole new level. Finally, it is a great pleasure to thank my supervisors – Vincenzo Giannini, Peter Haynes and Derek Lee working with whom was a privilege. Thank you for all your contributions and guidance as well as proofreading the thesis and providing many helpful suggestions on how to improve it. Derek has offered his help many times with quantum mechanics and localization always pushing to make our work as rigorous as possible. Peter has helped greatly with first-principles studies of topological nanoparticles. His attention to details has been invaluable. At last, I am greatly indebted to Vincenzo for many hours spent discussing the present research, suggesting new routes, solving technical problems and advising on how to write it up comprehensively as well as his generous guidance and boundless enthusiasm. On the non-academic side, I am grateful to Imperial Chaplain Hogetsu Baerndal for her lunch-time meditation sessions as well as masters Mark Sargeant (St' Katherine's TKD) and Christopher Dancel (ICUTKD) for their classes which provided breaks when most needed and helped grow in other directions. Many thanks to my friend Themistoklis Mavrogordatos for his willingness to discuss physics and many other subjects. None of the present work would be possible without my parents. I am very thankful to them for the hard work and devotion to give their children the best possible education. This thesis is dedicated to Niina and Aleksandr Siroki.

Chapter 1

Introduction

"There is plenty of room at the bottom"

Richard P. Feynman

1.0.1 Motivation and Overview

Miniaturisation has always been a goal of techonology: smaller constituent parts require less material and make the overall product faster and more convenient to use. Let us define the number of possible designs of the final product as N. Then, N depends on the ratio of the product size to that of the smallest building block, R, and the number of different blocks available, B, as $N \approx R!/(R/B)!$. For these reasons we want the building blocks to be as tiny and varied as possible.

One the most active miniaturisation directions today is nanophotonics. The purpose of nanophotonics put broadly is to manipulate light at the nanoscale. This is required, for example, in integrated optical and optoelectronic circuits – an attractive alternative to lossy metallic wires [6]. To achieve this we need to create nanodevices with desired optical properties and this is where topological insulators come in. These materials were discovered in 2005 (see [7–9] - for review) and are famous because some of their properties are remarkably stable – over half a century ago, Richard Feynman famously said that the quantum electrodynamics theory agrees with experiment to one part in a billion when predicting the g-factor of the electron. In the Quantum Hall effect, the transverse conductivity plateaus are also flat to within one part in a billion. This is remarkable because the latter phenomenon involve a macroscopic sample with numerous imperfections - not just a single electron. The robustness against

disorder is characteristic of the boundary states for topological materials. Here our focus will be on topological insulators (see Fig. 1.1) which conduct on the surface despite the insulating bulk (in 2D they are known as the "Quantum Spin Hall effect"). Their surface states are spin-filtered meaning, that the right- and left-moving states have opposite spins. This provides an additional degree of freedom in tuning the optical properties of a device made from such materials. Moreover, being a surface effect, it will be more pronounced in nanoparticles which have large surface-to-volume ratios compared to bulk samples. The present thesis aims to study the use of confined topological insulators to manipulate light. The first chapter of this thesis is devoted to the theoretical background and introduces the topological insulators more formally. It also contains discussions of theoretical and computational methods from solid state physics and photonics used in subsequent chapters.

Chapters 2 and 3 are devoted to nanowires and nanoparticles made from topological insulators. In particular, we demonstrate the robustness of the states against disorder using analytical and tight-binding models. This is followed by studying how the nanostructures interact with light. Our main finding is that the delocalized surface states interact with bulk optical phonons of the constituent material to give a previously unreported absorption mode. Interestingly, this mode occurs in the region of 0.1-10 THz, where no efficient sources and receivers exist [10,11]. The studied nanostructures may prove useful at these frequencies and are of potential use for telecommunication, spectroscopic and security screening applications.

Chapters 4 and 5 describe our studies of photonic topological insulators. These have spin-filtered edge states which permit unidirectional propagation of light (rather than electrons). Chapter 4 introduces two new photonic topological insulators. One of them can be made from a dielectric and has not yet been realized experimentally. The other is a metallic metasurface invented by our collaborators to which we contributed by understanding its edge states, their frequencies and polarizations. The next chapter considers what happens in a confined topological photonic crystal. We find that the discrete edge states still support unidirectional propagation and can bend around sharp corners without scattering. These findings are of use for practical realizations of photonic crystals which often comprise several hundred unit cells and display the finite size effects. The final chapter gives an overview of the presented results and discusses promising directions for future work.

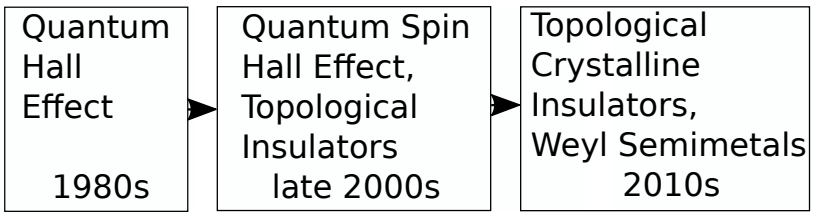

Figure 1.1: Discovery timeline of eletronic topological phases. The Quantum Hall effect relies on an external magnetic field. Topological insulators and the Quantum Spin Hall effect require time-reversal symmetry to realize a topological phase whereas for topological crystalline insulators the analogous role is played by the spatial symmetries of the lattice. Finally, to realize a Weyl semimetal one needs to break either the time-reversal symmetry or the inversion symmetry of the system.

1.0.2 Bulk Topological Insulators

Topological insulators are a very young class of materials [12] yet they have attracted a lot of attention in the research community. The got their name from the peculiar topology of their bandstructure which leads to physical phenomena that are remarkably stable against perturbations. The Quantum Hall effect was the first topological phenomenon to be discovered. There the non-trivial topology of the 2D material's band structure is caused by a strong external magnetic field. It results in the remarkable flatness of the transverse conductivity, σ_{xy}, plateaus as a function of the applied field. The steps in these plateaus are given by a topological invariant - a number that is insensitive to details of the material according to

$$\sigma_{xy} = ne^2/h \tag{1.1}$$

where n is an integer as discovered by Thouless *et al.* [13]. The conducting behavior occurs at the edge whereas the value of n depends on the bulk band structure. As a result any edge perturbations do not have an effect on the conductivity.

In recent years it was realised that an external magnetic field is not necessary and a topogical phase can exist in materials with strong spin-orbit coupling [12]. The latter can be seen as a magnetic field that points in one direction for spin-up electrons and in the opposite direction for spin-down electrons. These materials became known as topological insulators. Up to date there have been several dozens of TI materials discovered [9]. Many of the predictions were made using DFT [14–16] though some later proved to be false positives. Among successful examples Bi_2Se_3 was predicted and confirmed to have a relatively large bulk band gap of 0.3 eV and a simple surface spectrum [14]. It's topological bulk band structure gives rise to the single Dirac cone of surface states. Dirac cone is centered at the Γ-point

of the surface 2D Brillouin zone in Bi_2Se_3. As in other TIs, these surface states are spin-momentum locked, meaning that spin lies in-plane perpendicular to the 2D **k**-vector of the state. This feature is found both with DFT [17] and experimentally confirmed using spin-ARPES [18]. The states survive prolonged exposure to air [19] as expected from their topological protection and are readily observed at room temperature [21, 22].. Non-magnetic impurities can only shift the Dirac cone but cannot remove the states [20] which is also observed experimentally [19].

One of then main anticipated applications for the spin-momentum locked (aka helical) states is spintronics, i.e. electronics where electron spin is used as a primary carrier of information. However, numerous attempts to study the transport properties of these surface states have been significantly hindered by the bulk defects in Bi_2Se_3. These bulk carriers arising from the numerous defects dominate the transport making the contribution of the surface states difficult to distinguish [1] in bulk samples. One study tried to circumvent the problem using thin films [23] – these indeed showed thickness-independent transport however it is not clear whether the topological states or surface accumulation layer was responsible for it.

1.0.3 Topological Insulators Interacting with Light

The interaction of topological insulators with light was studied mostly in bulk samples. As such illuminating the surface of a topological insulator with circularly polarised light pulse was found to produce a surface photocurrent due to the helical, i.e. spin-momentum locked nature of the Dirac surface states [24]. Another consequence of helicity, namely, the transient magnetisation caused when the Dirac electrons are excited by circularly polarised pulses was found by [25] who studied relaxation processes following the photoexcitation. Yet another study found that THz light can be used to produce direct current in topological insulators (aka the photogalvanic effect) [26]. The effect was attributed to the surface electrons [26] based on the argument that the bulk has inversion symmetry while the surface – does not.

The effect of topological surface states on the light has received somewhat more attention. Here it is important to mention the topological magnetoelectric effect – which is a quantised electromagnetic response of 3D topological insulators, c.f. the quantised conductance of the Quantum Hall effect. This effect occurs when time-reversal symmetry is broken on the topological insulator surface but not in

the bulk [8]. The resultant conductance is half of that in the Quantum Hall effect

$$\sigma_{xy} = e^2/2h \tag{1.2}$$

This quantised conductance can be probed with light [8] where it results in coupling between electric and magnetic fields. This coupling manifests through Kerr rotation which is a change in polarisation plane of linearly polarised light on reflection [27]. The Kerr effect was observed in topological insulator thin films [27] where the resultant Kerr rotation found now holds a record among all known materials.

Another experimental study of Bi_2Se_3 microribbons claimed that their optical extinction is modified by Dirac electrons [28]. However, it might be that the behaviour attributed to the Dirac electrons is due to the ubiquitous bulk carriers mentioned previously. This was the case in a study on large nanoplates [29] where plasmon modes due to bulk carriers were observed. Another study of nm-size topological insulator crystals found that they have a large band-gap [30] presumably due to a combination of lattice strain and quantum confinement. On the theoretical side, one study predicted a divergent absorption cross section of topological insulator thin films [31]. Another interesting finding was that of a second surface Dirac cone which was predicted in Bi_2Se_3 to lie 1.5 eV directly above the first one using DFT calculations [16]. This was confirmed experimentally using two-photon photoemission technique [32] where the electron is first excited in to the unoccupied state and subsequently photoemitted. These discoveries suggest that topological surface states may also find a use in manipulating light in the visible region. Finally, there were studies investigating how surfaces are modified under the influence of high intensity laser pulses [33, 34]. In particular, it was found that the Dirac cone is transformed into a set of Floquet-Bloch bands which represent a sequence of Dirac cones stacked on top of each other and separated by frequency of incident light [34].

1.0.4 Topological Insulator Nanostructures

For the TI nanostructures there are two important factors to consider – quantum confinement and geometry. The first manifests in the discreteness of states as the sample reaches nanoscale sizes. In fact, for very small sizes the surface states disappear - in Bi_2Se_3 thin films this happens for thicknesses below 5 nm [35] due to the hybridisation of the surface states (decay length $\sim$ 1 nm). Simply speaking, there becomes not enough 'bulk' to have a band structure (which in turn gives rise to the surface states). Considering geometry it should be noted that the overwhelming majority of the experiments

described above focused on the (111) surface of Bi_2Se_3 (or a material from its family) which is explained by its layered structure. Also theoretically it is easiest to find the surface spectrum for the surface perpendicular to a principal axis of the material [36]. However, there also exist theoretical studies of how the surface Dirac cone changes with termination [20, 37]. The latter studies have found that the cone only gets moderately distorted for different planar terminations.

The first nanostructres to be investigated were topological insulator nanowires (cylinders). We will describe the surface states on the nanowire surface later but the main difference from the planar surface is that there are now several bands due to quantisation of motion in azimuthal direction [3, 38–40]. These bands reduce to a single Dirac cone in the limit of large radii. The ideal cylindrical shape is not important as qualitatively the same results were obtained for rectangular nanowires – with tight-binding [3,39] and an analytical approach of separating different rectangular regions into patches [36].

In case of a spherical nanoparticle the quantum confinement leads to a discrete spectrum of surface states [4,41] - these analytical solutions have been confirmed with tight-binding calculations in [4] and the present work. In analogy with a 3D quantum well the momentum labels for the surface states are now discrete.

To summarise, the existence of surface states is guaranteed by the non-trivial topology of the bulk band structure and time-reversal symmetry. Inverted band gap in the topological insulator on one side and normal band gap in the trivial insulator on the other is what gives rise to the states appearing across the boundary. In addition to spin-momentum locking, another general argument suggesting protection of the surface states against non-magnetic disorder follows from the fact that they occupy an area A_k which is a fraction of the 2D first Brillouin zone (for planar surface). This implies that in real space the surface wavefunction will be delocalised over surface areas larger than $\sim (2\pi)^2/A_k$ making the states insensitive to atomic scale disorder [42].

1.0.5 Photonic Topological Insulators

Advances in studying the topological phenomena of electronic bandstructures prompted researchers to reconstruct their analogues with bandstructures of light. Here the main role is played by photonic crystals – media with periodic variation of ϵ and μ. The resultant bandstructures are subject to the same topological considerations as in the electronic case. As a result the bulk band structure can give rise to the boundary states of photons which support unidirectional propagation. The latter would

allow to decrease scattering losses in waveguides [43] and were realised experimentally in a number of works – [44–50]. The main difference with the electronic case is that photons have integer spin which leads to different behaviour when applying a time-reversal operation. In particular one cannot make a topological insulators based solely on time reversal symmetry as for electrons. However there are other tricks that one can use to achieve a topological phase with photons. As such, one can break time-reversal symmetry [46, 47] or use lattice symmetry [48–51]. The main difficulty with the proposed designs is scaling them to visible wavelengths. In this respect designs based on the crystalline symmetry appear attractive as they involve simple dielectric materials and their operating frequency range scales with size. More generally, the unidirectional propagation which depends on the spin or pseudo-spin of light can be used to filter one polarization from the other. Moreover, the spin provides an additional degree of freedom interesting for using topological photonic crystals for quantum information applications [52, 53].

Chapter 2

Theoretical background

Throughout this thesis we will be concerned with single-particle effects. Many of the topological insulators discovered to date are well described using the conventional band theory where the interaction effects between electrons are considered as an effective potential. This allows to treat each particle as governed by the single-particle Schrodinger equation. The latter can be further approximated as shown in this chapter. Analogous results derived from Maxwell's equations and leading to photonic band structures are also presented. We also give a brief overview of necessary results from group theory as well as introduce the main concepts from the theory of topological insulators.

2.1 Methods from quantum mechanics

2.1.1 Schrodinger equation and Bloch's theorem

In quantum mechanics the behaviour of an electron is governed by the Schrodinger equation

$$\hat{H}\Psi(\mathbf{r},t) = \frac{\hat{\mathbf{p}}^{\mathbf{2}}}{2m}\Psi(\mathbf{r},t) + V(\mathbf{r})\Psi(\mathbf{r},t) = i\hbar\partial_t\Psi(\mathbf{r},t) \tag{2.1}$$

where $\hat{\mathbf{p}} = -i\hbar\nabla$ and the other terms have their usual meaning. For an eigenstate with energy E of the above Hamiltonian, $\hat{H}$ given by

$$\Psi(\mathbf{r},t) = \psi(\mathbf{r})e^{-iEt/\hbar} \tag{2.2}$$

the Schrodinger equation turns becomes time-independent (stationary):

$$\hat{H}\psi(\mathbf{r}) = \frac{\hat{\mathbf{p}}^{\mathbf{2}}}{2m}\psi(\mathbf{r}) + V(\mathbf{r})\psi(\mathbf{r}) = E\psi(\mathbf{r}) \tag{2.3}$$

In case of a crystalline solid the above problem simplifies [54]. Namely, the potential is periodic, $V(\mathbf{r}+\mathbf{R}) = V(\mathbf{r})$ for some lattice vector $\mathbf{R}$, and can be Fourier-expanded:

$$V(\mathbf{r}) = \sum_{\mathbf{G}} V_{\mathbf{G}} e^{i\mathbf{G}\cdot\mathbf{r}} \tag{2.4}$$

where the sum is over reciprocal lattice vectors, $\mathbf{G}$. This together with the expansion of the wave-function

$$\psi(\mathbf{r}) = \sum_{\mathbf{q}} c_{\mathbf{q}} e^{i\mathbf{q}\cdot\mathbf{r}} \tag{2.5}$$

allows to rewrite the Schrodinger Eq. 2.3 as

$$\left(\frac{\hbar^2 q^2}{2m} - E\right) c_{\mathbf{q}} + \sum_{\mathbf{G}} V_{\mathbf{G}} c_{\mathbf{q}-\mathbf{G}} = 0 \tag{2.6}$$

Here we can substitute $\mathbf{q} = \mathbf{k}+\mathbf{G}$ with $\mathbf{k}$ confined to the first Brillouin zone (1BZ). The above Eq. 2.6 shows that the potential's Fourier components, $V_{\mathbf{G}}$, link the coefficients $c_{\mathbf{k}}$ with those at $c_{\mathbf{k}+\mathbf{G}}$. The solution for a given wavevector $\mathbf{k}$ then becomes

$$\psi(\mathbf{r}) \to \psi_{\mathbf{k}}(\mathbf{r}) = \sum_{\mathbf{G}} c_{\mathbf{k}+\mathbf{G}} e^{i(\mathbf{k}+\mathbf{G})\cdot\mathbf{r}} = e^{i\mathbf{k}\cdot\mathbf{r}} \sum_{\mathbf{G}} c_{\mathbf{k}+\mathbf{G}} e^{i\mathbf{G}\cdot\mathbf{r}} \tag{2.7}$$

which is often rewritten as

$$\psi_{\mathbf{k}}(\mathbf{r}) = e^{i\mathbf{k}\cdot\mathbf{r}} u_{\mathbf{k}}(\mathbf{r}) \tag{2.8}$$

where $u_{\mathbf{k}}(\mathbf{r}) = u_{\mathbf{k}}(\mathbf{r}+\mathbf{R})$. Correspondingly, its energy also depends on $\mathbf{k}$: $E \to E_{\mathbf{k}}$. The allowed energy levels of electrons in a crystal are then represented as a function of $\mathbf{k}$. Each continuous line of energy forms a band. These levels are filled starting from the lowest possible (subject to the exclusion principle). The energy of the highest occupied level is known as the Fermi energy and the energy regions in which no states exist for any $\mathbf{k}$ are known as "band gaps".

2.1.2 $\mathbf{k}\cdot\mathbf{p}$ approximation

Bloch's theorem (2.1.1) simplifies the Schrodinger equation however in most cases it remains too difficult to be solved exactly. For this reason, a number of approximations have been developed both for analytical and computational treatment. On the analytical side the $\mathbf{k}\cdot\mathbf{p}$ method is often used. For simplicity, we will not include the spin label and ignore the spin-orbit coupling terms – the interested reader can find the full derivation in [55]. Substituting Eq. 2.8 into the stationary version of the Schrodinger Eq. 2.3 yields

$$\left(\frac{\hat{\mathbf{p}}^2}{2m}+\frac{\hbar}{m}\mathbf{k}\cdot\hat{\mathbf{p}}+\frac{\hbar^2k^2}{2m}+V\right)u_{n\mathbf{k}}(\mathbf{r})=E_{n\mathbf{k}}u_{n\mathbf{k}}(\mathbf{r}) \tag{2.9}$$

where we introduced the band index, n. The idea is then to find a solution perturbatively around $\mathbf{k}=\mathbf{0}$ using an expansion in $u_{n'\mathbf{0}}(\mathbf{r})$:

$$u_{n\mathbf{k}}(\mathbf{r})=\sum_{n'}c_{n'}(\mathbf{k})u_{n'\mathbf{0}} \tag{2.10}$$

The cellular wavefunctions satisfy

$$\int_\Omega d\Omega u^*_{n\mathbf{0}}(\mathbf{r})u_{n'\mathbf{0}}(\mathbf{r})=\delta_{nn'} \tag{2.11}$$

where the integration is performed over one unit cell's volume, Ω. Substituting the expansion (2.10) into the Eq. 2.9 then multiplying Eq. 2.9 by $u_{n\mathbf{0}}$ and integrating over one unit cell yields

$$\left(E_{n\mathbf{0}}+\frac{\hbar^2k^2}{2m}-E_{n\mathbf{k}}\right)c_n(\mathbf{k})+\sum_{n'}\frac{\hbar}{m}\mathbf{k}\cdot\langle u_{n\mathbf{0}}|\,\hat{\mathbf{p}}\,|u_{n'\mathbf{0}}\rangle\,c_{n'}(\mathbf{k})=0 \tag{2.12}$$

To find the solution it is required that we solve the matrix Eq. 2.12 for coefficients. In practice the basis used is truncated to a few states with energies close to that of the state we are expanding. For topological insulators the most important are the two bands below and two above the band gap. Therefore in this thesis, we will be concerned with four basis states for each system and hence often speak about 4×4 $\mathbf{k}\cdot\mathbf{p}$ Hamiltonians.

2.1.3 Envelope function approximation

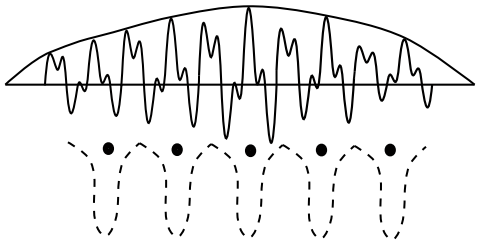

Figure 2.1: The envelope function approximation modulates the quick oscillations of cellular wavefunctions by slowly varying envelopes. Because the envelopes are coarse grained and are only sensitive to details on the scale of a few unit cells, one can often obtain them analytically. Points represent atomic nuclei and the dashed line – their combined potential.

The $\mathbf{k}\cdot\mathbf{p}$ method described in the previous section is suitable for describing periodic structures. But what happens if a sample is finite? The idea here is to again expand in the periodic parts of the cellular wavefunctions, $u_{n\mathbf{0}}$. However, instead of using coefficients that depend on $\mathbf{k}$ as in Eq. 2.10 we use real-space coefficients that depend on $\mathbf{r}$. Then some state $\psi(\mathbf{r})$ is expanded as [55]:

$$\psi(\mathbf{r}) = \sum_{n'} f_{n'}(\mathbf{r}) u_{n'\mathbf{0}}(\mathbf{r}) \tag{2.13}$$

where the envelope functions $f_n(\mathbf{r})$ are assumed to vary slowly on the scale of a lattice constant – see Fig. 2.1. If we substitute the expansion (2.13) into the Schrodinger Eq. 2.3 then multiply by $u_{n\mathbf{0}}$ and integrate over one unit cell then we obtain [55]:

$$\left(E_{n\mathbf{0}} + \frac{\hat{\mathbf{p}}^{\mathbf{2}}}{2m} - E\right) f_n + \sum_{n'} \frac{\langle u_{n\mathbf{0}}|\,\hat{\mathbf{p}}\,|u_{n'\mathbf{0}}\rangle}{m}\hat{\mathbf{p}} f_{n'} = 0 \tag{2.14}$$

where it was assumed that f_n can be taken outside the integral (i.e. varies slowly over one unit cell). Note, that the resultant Eq. 2.14 has the same form as Eq. 2.12 provided we make the substitutions

$$\mathbf{k} \leftrightarrow -i\nabla \qquad c_n(\mathbf{k}) \leftrightarrow f_n(\mathbf{r}) \tag{2.15}$$

which allow to conveniently transfer between extended and confined directions. Here we assumed that the structure is confined in all three directions. One of the original uses of the envelope function approximation was to treat semiconductor heterostructures where it is used against non-periodic directions and $\mathbf{k}\cdot\mathbf{p}$ theory is used along the periodic ones. The same approach can be used to treat

surface states – for a planar (and cylindrical) surface the envelope functions would describe the decay away from the surface. Finally, we note that finding coefficients can be useful in many cases even if we do not know the cellular wavefunctions themselves. For example, using Eq. 2.13 one can obtain probabilty density averaged over a unit cell as follows:

$$\frac{1}{\Omega}\int_{\Omega}|\psi(\mathbf{r})|^2 = \frac{1}{\Omega}\sum_{n,n'} f_n^*(\mathbf{r}) f_{n'}(\mathbf{r})\delta_{n,n'} = \frac{1}{\Omega}\sum_{n}|f_n(\mathbf{r})|^2 \tag{2.16}$$

2.1.4 Tight-binding

Above we considered analytical approaches to the electronic structure of semiconductors however there also exist computational methods. In this thesis, we will use the tight-binding approximation which has an affordable computational cost for the problems considered. The method considers crystals as derived from individual atoms carrying orthonormal atomic orbitals – see [54] for details. The latter can be combined into wavefunctions satisfying the Bloch condition (2.8):

$$\psi_{\mathbf{k}} = \sum_i \sum_\alpha c_{i\alpha}\phi_{i\alpha} \tag{2.17}$$

where i denotes an atom at side i and α denotes the type of the orbital involved (the band index dropped for simplicity). Substituting (2.17) into the Schrodinger Eq. 2.3, multiplying on the left by $\phi_{j\beta}$ and integrating one obtains a matrix equation

$$H_{j\beta i\alpha}c_{i\alpha} = Ec_{j\beta} \tag{2.18}$$

where

$$H_{j\beta i\alpha} = \langle\phi_{j\beta}|\,\hat{H}\,|\phi_{i\alpha}\rangle \tag{2.19}$$

The tight-binding method stands for approximating the above matrix elements (2.19). Usually they are taken to be non-zero for orbitals between nearest neighbours (or also next nearest neighbours) which is a good approximation for covalent crystals with little electron density in-between the atoms. For an example of tight-binding Hamiltonian see Eq. 3.40.

2.1.5 Time-dependent perturbation theory

All the methods described above dealt with stationary states and time-independent Hamiltonians. Here, we outline the behaviour of a particle in the presence of a time-varying perturbation $V(\mathbf{r}) \rightarrow V(\mathbf{r}) + \delta V(\mathbf{r}, t)$ [56]. Let us now assume that before the perturbation was turned on the particle was in some stationary state ψ_i. Because the perturbation is assumed small the new wavefunction becomes

$$\psi_i(\mathbf{r}) \rightarrow \psi_i(\mathbf{r}) + \delta\psi(\mathbf{r}, t) \tag{2.20}$$

The perturbation part, $\delta\psi$, can be expanded in terms of unperturbed states:

$$\delta\psi(\mathbf{r}, t) = \sum_{n \neq i} c_n(t)\psi_n(\mathbf{r})e^{-iw_{ni}t} \tag{2.21}$$

where w_{ni} is the difference in frequencies of the stationary states: $w_{ni} = (E_n - E_i)/\hbar$. Let us now assume that $\delta V(\mathbf{r}, t)$ is a harmonic perturbation with frequency w. If this perturbation has been slowly switched on at time $t = 0$, the coefficients of the expansion (2.21) are to first order given by [56]

$$c_n^{(1)} = -\frac{i}{\hbar}\int_0^t dt' \, \langle n| \, \delta V \, |i\rangle \, e^{i(w_{ni}-w)t} = -\langle n| \, \delta V \, |i\rangle \, \frac{e^{i(w_{ni}-w)t} - 1}{\hbar(w_{ni} - w)} \tag{2.22}$$

where we assumed a pure state at the beginning (the perturbing potential can be slowly turned on from $t = -\infty$ if multiplied by $e^{\epsilon t}$ where ϵ is a small positive constant). At resonance, $w_{ni} = w$, we obtain the Fermi Golden rule [56]. If the frequencies are detuned then the perturbation, $\delta V(\mathbf{r}, t)$, causes a time-dependent probability density and hence a changing charge density. For a particle with charge q the resultant charge density is given by

$$q|\psi(\mathbf{r}, t)|^2 = q(|\psi_i(\mathbf{r})|^2 + \psi_i(\mathbf{r})^*\delta\psi(\mathbf{r}, t) + \psi_i(\mathbf{r})(\delta\psi(\mathbf{r}, t))^* \tag{2.23}$$

2.2 Methods from electromagnetism

2.2.1 Maxwell's equations and boundary conditions

The classical behavior of electric and magnetic fields at macroscopic scales is described by Maxwell's equations [57]:

$$\nabla \cdot \mathbf{E} = \frac{\rho}{\epsilon_0} \tag{2.24}$$

$$\nabla \cdot \mathbf{B} = 0 \tag{2.25}$$

$$\nabla \times \mathbf{E} = -\partial_t \mathbf{B} \tag{2.26}$$

$$\nabla \times \mathbf{H} = \mathbf{j} + \partial_t \mathbf{D} \tag{2.27}$$

where all symbols have their usual meanings. In a homogeneous medium which polarizes and magnetizes linearly in response to external fields the Maxwell's equations are supplemented by the constitutive relations:

$$\mathbf{D} = \epsilon_0 \epsilon_{\text{in}} \mathbf{E} \tag{2.28}$$

$$\mathbf{B} = \mu_0 \mu_{\text{in}} \mathbf{H} \tag{2.29}$$

Here ϵ_{in} is either a scalar or a tensor depending on whether the material's response to $\mathbf{E}$ is isotropic or anisotropic and likewise for μ_{in} and $\mathbf{B}$ field.

Each of the Maxwell's equations (2.24)-(2.27) can be integrated at the boundary of two materials. In conjunction with Gauss' ("divergence") and Stokes' ("curl") theorems this yields four boundary conditions on the fields in two media labelled 1 and 2:

$$\mathbf{n} \cdot (\mathbf{D}_1 - \mathbf{D}_2) = \sigma \tag{2.30}$$

$$\mathbf{n} \cdot (\mathbf{B}_1 - \mathbf{B}_2) = 0 \tag{2.31}$$

$$\mathbf{n} \times (\mathbf{E}_1 - \mathbf{E}_2) = 0 \tag{2.32}$$

$$\mathbf{n} \times (\mathbf{H}_1 - \mathbf{H}_2) = \mathbf{K} \tag{2.33}$$

where σ is the surface charge density and $\mathbf{K}$ is the surface current density at the interface.

2.2.2 Bloch's theorem for light

In this thesis we will only be concerned with materials for which $\mu_{\text{in}} = 1$. When ϵ_{in} varies periodically in space we can write the Bloch theorem for light – see [58] for details. Namely, combining Maxwell's equations (2.26) and (2.27) from 2.2.1 for the magnetic field with a given frequency w, $\mathbf{H}(\mathbf{r})e^{-iwt}$ yields

$$\hat{L}\mathbf{H} = \nabla \times \left(\frac{1}{\epsilon_{\text{in}}} \nabla \times \mathbf{H} \right) = \frac{w^2}{c^2}\mathbf{H} \tag{2.34}$$

Then substituting $\mathbf{H} = e^{i\mathbf{k}\cdot\mathbf{r}}\mathbf{u}(\mathbf{r})$ gives

$$(i\mathbf{k} + \nabla) \times \frac{1}{\epsilon_{\text{in}}}(i\mathbf{k} + \nabla) \times \mathbf{u}(\mathbf{r}) = \frac{w^2}{c^2}\mathbf{u}(\mathbf{r}) \tag{2.35}$$

The latter means we can label $\mathbf{u}(\mathbf{r}) = \mathbf{u}_{\mathbf{k}}(\mathbf{r})$ and $w = w(\mathbf{k})$. Moreover, because $\epsilon_{\text{in}}(\mathbf{r} + \mathbf{R}) = \epsilon_{\text{in}}(\mathbf{r})$ for a reciprocal lattice vector $\mathbf{R}$, the above equation means only needs to be solved within one unit cell implying that

$$\mathbf{u}_{\mathbf{k}}(\mathbf{r} + \mathbf{R}) = \mathbf{u}_{\mathbf{k}}(\mathbf{r}) \tag{2.36}$$

which is the same result as we had in the electronic case – see Eq. 2.8.

2.2.3 Frequency domain methods

In addition to the analytical methods in this thesis we will also make use of numerical methods. The first of these is a frequency domain method which can be used to obtain band structures for light in media with periodic variation of ϵ_{in}. To obtain a band structure one solves the master equation (2.34) substituting $\mathbf{H} = \mathbf{u}_{\mathbf{k}}e^{i\mathbf{k}\cdot\mathbf{r}}$ – see 2.2.2. The solutions need to satisfy the transversality condition

$$(\nabla + i\mathbf{k})\mathbf{u}_{\mathbf{k}} = 0 \tag{2.37}$$

which is automatically taken into account if plane waves are used as the basis. An iterative solver is then employed to find the eigenmodes of a given structure. The basic idea for the iterative solver relies on the Rayleigh-Ritz method and the fact that eigenmodes correspond to the extreme values of the following functional called the Rayleigh quotient:

$$\frac{\langle \mathbf{H} | \, \hat{L} \, | \mathbf{H} \rangle}{\langle \mathbf{H} | \mathbf{H} \rangle} \tag{2.38}$$

For a given eigenmode the value of the Rayleigh quotient above is equal to the the frequency squared – w^2. The lowest frequency mode $\mathbf{H}_0$ and its eigenvalue w_0 can then be obtained by adding terms to the trial wavefunction until its value is sufficiently converged. To find the second lowest eigenmode-eigenvalue pair one repeats the procedure subject to the constraint that $\langle \mathbf{H}_0 | \mathbf{H}_1 \rangle = 0$ and so on. In this work we will use the "MIT Photonic Bands" ("MPB") open source code [58]. The MPB code employs a plane wave basis and uses the conjugate-gradient algorithm to minimize the Rayleigh quotient for several eigenvectors simultaneously [59].

2.2.4 Finite-difference time-domain method

The finite-difference time-domain technique is not restricted to periodic structures and can be used to solve Maxwell's equations for arbitrary structures. Its main idea is to approximate derivatives with finite differences. This is done on a staggered ("Yee") lattice using a leapfrog method. To get a feeling for its workings consider solving Maxwell's equations in 1D:

$$\frac{\partial E_z}{\partial x} = \mu \frac{\partial H_y}{\partial t} \tag{2.39}$$

$$\frac{\partial H_y}{\partial x} = \epsilon \frac{\partial E_z}{\partial t} \tag{2.40}$$

Using the Yee lattice means that we calculate H_y at half-integer time and spatial steps, i.e. if t and x take integer values $0, 1, 2...$ then H_y is always calculated at some $t + 1/2, x + 1/2$. On the other hand, E_z is calculated at integer steps, i.e. x, t. This in turn allows to write the Eq. 2.39 as

$$\left.\frac{\partial E_z}{\partial x}\right|_{x+1/2,t} = \mu \left.\frac{\partial H_y}{\partial t}\right|_{x+1/2,t} \tag{2.41}$$

which using central finite differences becomes

$$\frac{E_z(x+1,t) - E_z(x,t)}{\delta x} = \mu \frac{H_y(x+1/2, t+1/2) - H_y(x+1/2, t-1/2)}{\delta t} \tag{2.42}$$

with the $\delta x, \delta t$ begin the spatial and time steps. This allows to obtain the $H_y(t + 1/2)$ in terms of fields at all previous times. The analogous equation for updating the E_z field can be derived from Eq. 2.40.

2.2.5 Dielectric particle in a quasi-static field

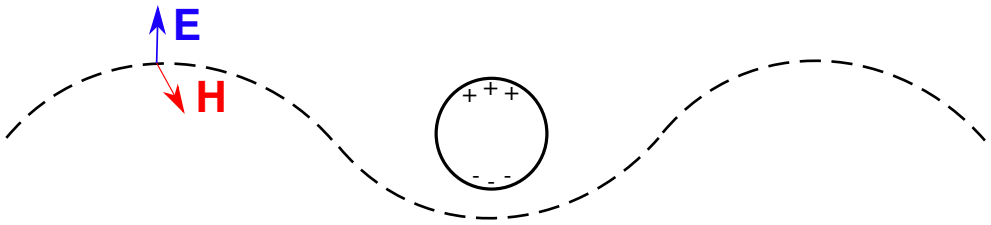

Figure 2.2: Spherical dielectric particle of radius R irradiated with light (dashed line) of wavelength $\lambda \gg R$. The external field can be treated as quasistatic allowing to solve the problem analytically.

Let us now turn back to the analytical methods and consider optical response of a dielectric particle to an incident light wave as in Fig. 2.2. In case the wavelength of light is much larger than the radius of the particle, $\lambda \gg R$, the electric field $\mathbf{E}(\mathbf{r})$ can be well approximated by a static potential $\Phi(\mathbf{r})$ [57]:

$$\mathbf{E} = -\nabla\Phi \tag{2.43}$$

Then in the absence of free charges, $\rho = 0$, Eq. 2.24 becomes the Laplace equation

$$\nabla^2\Phi = 0 \tag{2.44}$$

In spherical coordinates one can use the following expansion [57]:

$$\Phi(\mathbf{r}) = \sum_{l,m} \Phi_{l,m}(r, \theta, \phi) \tag{2.45}$$

where for $r < R$ we have

$$\Phi_{l,m} = r^l P_l^m(\cos\theta) e^{im\phi} \tag{2.46}$$

while for $r > R$

$$\Phi_{l,m} = r^{-l-1} Q_l^m(\cos\theta) e^{-im\phi} \tag{2.47}$$

and P_l^m and Q_l^m are the associated Legendre polynomials. Let us consider an isotropic particle described by scalar ϵ_{in} in vacuum ($\epsilon_{out} = 1$) subject to the incident plane wave whose electric field is along the x axis such that

$$\Phi_{ext} = -E_0 x = -E_0 r\cos\theta \tag{2.48}$$

Then the boundary conditions (2.30) and (2.32) translate to

$$\partial_\theta \Phi_{\text{in}}|_{r=R} = \partial_\theta \Phi_{out}|_{r=R} \tag{2.49}$$

and

$$\epsilon_{\text{in}} \partial_r \Phi_{\text{in}}|_{r=R} = \partial_r \Phi_{out}|_{r=R} \tag{2.50}$$

Using the above we are able to find the total potential for $r > R$ which is given by

$$\Phi_{out} = -E_0 r \cos(\theta) + E_0 \frac{\epsilon_{\text{in}} - 1}{\epsilon_{\text{in}} + 2} R^3 \frac{\cos\theta}{r^2} \tag{2.51}$$

where the last term arises due to the presence of the dielectric sphere. This term has the same form as that of a point dipole which allows to find the absorption cross section of the particle [57]:

$$\sigma_{abs} = k \text{Im}\left[4\pi R^3 \frac{\epsilon_{\text{in}} - 1}{\epsilon_{\text{in}} + 2}\right] \tag{2.52}$$

where $k = 2\pi/\lambda$. The solution for a dielectric wire in a quasistatic field perpendicular to its axis can be obtained analogously. In this case one solves the Laplace equation (2.44) in cylindrical coordinates – see [57] for full derivation.

2.3 Results from Group theory

We have already seen in Eqns. 2.1.1 and 2.2.2 how a discrete translational symmetry sets restrictions on the form of the wavefunction for electrons (2.8) and light (2.36). Here we consider the effect of other symmetries. Unless explicitly stated we ignore the effects of spin-orbit coupling for electrons (and analogous effects for light) and consider spinless particles. For concreteness we consider electrons whose behaviour is governed by a periodic Hamiltonian, $\hat{H}$, in Eq. 2.3, though the results can be easily translated to photons (described by $\hat{L}$ in Eq. 2.34) [58].

2.3.1 Speed of light introduction to group theory

In a general case, spatial symmetry operations, $\hat{R}_i$, of a Hamiltonian form a group G – see [60, 61] for more information. For this group one can come up with a mapping of symmetry operations

onto square matrices representing them. This mapping termed "representation" should conserve the relations between the group elements (symmetry operations). In particular, if for three symmetry operations, $\hat{R}_{1-3}$, it is true that

$$\hat{R}_1\hat{R}_2 = \hat{R}_3 \tag{2.53}$$

then for the matrices representing them, D_{1-3}, it should equally be true that

$$D_1 D_2 = D_3 \tag{2.54}$$

Of particular interest are the so-called irreducible representations of the group. Each of them is a mapping (unique up to a similarity transformation) of symmetry operations onto square matrices subject to the restriction that the matrices comprising a given representation cannot be brought to a block-diagonal form. If the the number of symmetry operations is finite, so will be the number of irreducible representations which together encode all information about the symmetries of the original Hamiltonian.

In addition to representaitons, another important concept is that of conjugacy classes. Suppose we have a group of symmetry operations G then two symmetry operations $\hat{R}_a, \hat{R}_b$ belong to the same class if

$$\hat{R}_a = \hat{R}_i\hat{R}_b\hat{R}_i^\dagger \qquad \forall \hat{R}_i \in G \tag{2.55}$$

The matrices D representing the symmetry operations will also form conjugacy classes. Because of the relation above all representing matrices belonging to one conjugacy class have the same trace which in group theory is called "character". Since an irreducible representation is unique up to a similarity transformation one normally does not work directly with the matrices comprising it. On the other hand, their characters (traces) are not affected by such transformations and are often used.

2.3.2 Character tables

Based on the concepts from 2.3.1 we can introduce a character table. To illustrate it we use the symmetry group of an equilateral triangle (C_{3v}) as an example. The triangle has six symmetry operations – three rotations by $0, 2\pi/3$ and $4\pi/3$ which we label as $\hat{R}_0, \hat{R}_1, \hat{R}_2$ and three reflection planes passing through its medians which we label as $\hat{R}_3, \hat{R}_4, \hat{R}_5$. These six operations fall into three conjugacy classes: $(\hat{R}_0)$, $(\hat{R}_1, \hat{R}_2)$ and $(\hat{R}_3, \hat{R}_4, \hat{R}_5)$. Moreover, the group of the triangle has three

irreducible representations – $\Gamma_1, \Gamma_1', \Gamma_2$ of dimensions one, one and two respectively. The character table as the name suggest contains the character (trace) of each irreducible representation (non-block-diagonal matrix) for each conjugacy class. For the triangle it looks as follows:

	$(\hat{R}_0)$	$(\hat{R}_1, \hat{R}_2)$	$(\hat{R}_3, \hat{R}_4, \hat{R}_5)$	linear	quadratic
Γ_1	1	1	1	z	$x^2+y^2,\ z^2$
Γ_1'	1	1	-1	-	-
Γ_2	2	-1	0	(x, y)	$(x^2-y^2, xy), (xz, yz)$

Table 2.1: The character table of the C_{3v} symmetry group (equilaterial triangle; has six symmetry operations, $\hat{R}_0 - \hat{R}_5$). The group has three irreducible representations – $\Gamma_1, \Gamma_1', \Gamma_2$. First three columns show characters for different conjugacy classes and the last two – basis functions.

2.3.3 Basis functions and selection rules

The columns labelled 'linear' and 'quadratic' in Table 2.1 give examples of basis functions for the group considered. The basis functions $\{|\Gamma i\rangle\}$ of an irreducible representation, Γ are any group of functions that satisfy

$$\hat{R}\,|\Gamma i\rangle = \sum_j D^{\Gamma}(\hat{R})_{ji}\,|\Gamma j\rangle \tag{2.56}$$

where $\hat{R}$ is again a symmetry operation of the group and $D^{\Gamma}(\hat{R})$ is the irreducible matrix representing it. Importantly, wavefunctions in quantum mechanics also form bases for irreducible representations of the parent Hamiltonian [60]. Eq. 2.56 then means that the wavefunctions corresponding to a given irreducible representation will be degenerate with degeneracy given by the dimension of the representation matrix.

Using the definition (2.56) and some results from group theory [60] one can show that wavefunctions corresponding to different irreducible representations are orthogonal. The same is true for different wavefunctions belonging to the same representation. The above is useful for finding the matrix elements, e.g. in $\mathbf{k}\cdot\mathbf{p}$ Hamiltonians – see 2.1.2. For example, consider a matrix element

$$\langle\psi_i|\,\delta\hat{H}\,|\psi_j\rangle \tag{2.57}$$

where δH is a perturbing Hamiltonian and $\psi_{i,j}$ are unperturbed wavefunctions. We can say whether this element will vanish from knowing which representations do $|\psi_i\rangle$ and $\delta\hat{H}\,|\psi_j\rangle$ correspond to. The group theory thus allows us to evaluate the matrix elements (up to a constant factor) from knowing the symmetries of the wavefunctions and the perturbing Hamiltonian but not their exact functional

forms.

2.3.4 Mirror and inversion symmetries

Many crystals possess mirror or inversion symmetries which put restrictions on the wavefunctions. Firstly, we consider the effect of mirror symmetry with xy as the mirror plane. The reflection with respect to this plane is then represented by a unitary operator $\hat{M}$ which swaps $z \to -z$. A Hamiltonian that has such a mirror symmetry then satisfies

$$\hat{M}^\dagger \hat{H} \hat{M} = \hat{H} \tag{2.58}$$

i.e. this mirror operator, $\hat{M}$, commutes with the Hamiltonian:

$$\hat{M}\hat{H} = \hat{H}\hat{M} \tag{2.59}$$

Now suppose we have an eigenstate ψ of the Hamiltonian which has energy E. If we then consider an eigenstate $\hat{M}\psi$, we see that it satisfies

$$\hat{H}(\hat{M}\psi) = \hat{M}(\hat{H}\psi) = E(\hat{M}\psi) \tag{2.60}$$

which means that if $\hat{M}\psi$ is different from ψ then the two states are degenerate. This is a special case of a more general principle that symmetries often lead to degeneracies. Another aspect of the mirror symmetry is that if we write $\hat{M}\psi(x, y, z) = e^{i\alpha}\psi(x, y, -z)$ then

$$\hat{M}^2\psi(x, y, z) = e^{2i\alpha}\psi(x, y, z) \tag{2.61}$$

This means that $e^{i\alpha} = \pm 1$ and implies that the eigenstates of the Hamiltonian can be chosen to satisfy

$$\psi(x, y, z) = \pm\psi(x, y, -z) \tag{2.62}$$

For the case of inversion ("parity") symmetry the results are analogous except that the associated operator, $\mathcal{I}$ now swaps $\mathbf{r} \to -\mathbf{r}$ and the wavefunctions have definite parity:

$$\psi(\mathbf{r}) = \pm\psi(-\mathbf{r}) \tag{2.63}$$

In an inversion-symmetric crystal we have

$$\mathcal{I}\psi_{n\mathbf{k}}(\mathbf{r}) = \psi_{n-\mathbf{k}}(\mathbf{r}) \tag{2.64}$$

and hence

$$E_n(\mathbf{k}) = E_n(-\mathbf{k}) \tag{2.65}$$

2.3.5 Time-reversal symmetry and Kramers' theorem

Time-reversal invariance implies that the Hamiltonian is indistinguishable after reversing the arrow of time. The time-reversal operator, Θ, acts differently on particles with integer and half-integer spins. For spinless particles $\Theta = K$, the complex conjucation operator, and satisfies $\Theta^2 = 1$. For a particular state $\psi_{n\mathbf{k}}(\mathbf{r})$ in a periodic system time-reversal symmetry leads to [60]

$$\Theta\psi_{n\mathbf{k}}(\mathbf{r}) = \psi^*_{n\mathbf{k}}(\mathbf{r}) = \psi_{n-\mathbf{k}}(\mathbf{r}) \tag{2.66}$$

which implies

$$E(\mathbf{k}) = E(-\mathbf{k}) \tag{2.67}$$

– the same holds for photons [58]. For particles with spin 1/2 such as electrons $\Theta^2 = -1$ which in a periodic potential leads to [60]

$$\Theta\psi_{n\mathbf{k}\uparrow}(\mathbf{r}) = \psi_{n-\mathbf{k}\downarrow}(\mathbf{r}) \tag{2.68}$$

and hence

$$E_\uparrow(\mathbf{k}) = E_\downarrow(-\mathbf{k}) \tag{2.69}$$

This result is known as the Kramers' theorem. It is very significant for topological insulators because it implies that even in the presence of spin-orbit coupling any energy level in a crystal is doubly degenerate.

2.4 Topological insulators

2.4.1 General theory

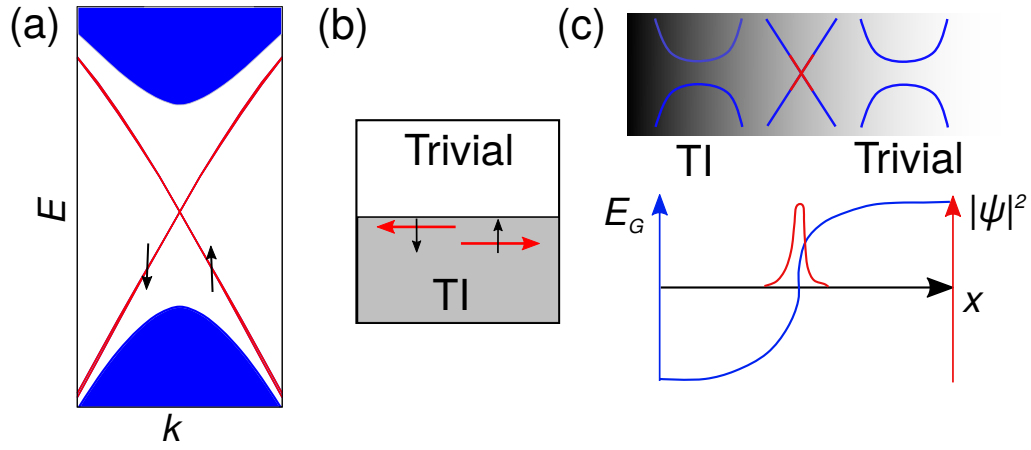

Figure 2.3: (a) Projected band structure of a topological insulator contains surface bands (red) with energies lying inside the band gap of bulk bands (blue). The surface states arise due to the change in the topological invariant at the boundary of the material. (b) They are spin-momentum locked meaning that states with opposite spins have opposite in-plane momenta. (c) The band gap E_G changes from negative to positive between topological (left) and trivial (right) insulators. It closes at the boundary resulting in the surface states

The main idea behind topological insulators (TIs) is that of a topological invariant. For a given material the topological invariant is a number that characterises the topology of its band structure. If the invariant is non-zero then the material will display topological properties – otherwise it is a trivial insulator. In the literature on TIs one often meets a phrase "protected by X-symmetry". This means that the symmetry X of the system determines the formula to calculate the topological invariant and restrict the values it can take. For example, in systems with time reversal symmetry the invariant takes binary values, $\mathcal{Z}_2 = 0, 1$. Another defining property of the invariant is that if we start changing the system keeping the relevant symmetries intact the invariant cannot change as long as the band gap is present [7].

The fact that the topological invariant can only change when the band gap closes becomes important when two systems with different values of the invariant come in contact – see Fig. 2.3. For example, consider a boundary between a topological and a trivial insulator both having time-reversal symmetry. If we imagine starting from one and going into the other then the invariant changes along the way. This means the band gap has to close and reopen at some point and this is what gives rise to the edge

(in 2D) or surface states (3D) at the interface between the two materials – see Fig. 2.3(c). Importantly, these boundary states are present due to the bulk band structure of each material which determines their invariant. For this reason, the states will be more robust against perturbations compared to the boundary states existing on a trivial-trivial insulator boundary. Another difference is that the boundary states of topological origin are spin-momentum locked, meaning that those with opposite in-plane wavevectors, $\mathbf{k}_{||}$, have opposite spins.

2.4.2 Time-reversal invariant topological insulators

At the moment of writing time-reversal symmetric TIs (also called "$\mathcal{Z}_2$ "TIs or simply "TIs") are merely a decade old [12] yet have already attracted much attention from researchers – see [7–9]. These materials are usually made of heavy elements at the bottom of the Periodic table that have strong spin-orbit coupling which results in them having non-zero $\mathcal{Z}_2$ invariant. Without the spin-orbit coupling all insulators are trivial. If one artificially turns it off in a TI (as possible in simulations) and then starts increasing then at some point the band gap in a material closes and reopens. The newly opened band gap is inverted meaning that the states have different ordering and the material has become a TI. The inverted band gap offers another view of why the surface states should occur at a topological-trivial insulator boundary. Namely, they allow to continuously connect the bulk bands as we go from one material into another. A crucial role here is played by the Kramers' theorem (see 2.3.5) which leads to protected crossings of the surface bands inside the bulk band gap.

Up-to-date several dozens of TI materials have been discovered [9]. Many of the predictions were made using density functional theory – see e.g. [14, 16]. Among those Bi_2Se_3 was predicted and confirmed to have a relatively large bulk band gap of 0.3 eV and a simple surface spectrum [14]. Its topological surface states form a single Dirac cone with energy lying inside the bulk band gap. This Dirac cone is centered at the Γ-point of the surface (2D) Brillouin zone in Bi_2Se_3. These surface states are spin-momentum locked as found both with DFT [17] and experimentally using spin angle-resolved photoemission spectroscopy [18]. They survive prolonged exposure to air and the presence of non-magnetic impurities [19] as expected from their topological origin. Furthermore, the surface Dirac cone shows little temperature broadening and is readily observed at ambient conditions [21, 22].

To find whether a given insulator is a TI we need to calculate its $\mathcal{Z}_2$ invariant. For spin 1/2 particles such as electrons the time reversal operator is given by $\Theta = i\sigma_y K$ where σ_y acts on the spin part of

the wavefunction and K is the complex conjucation operator. We now consider the matrix $w_{nm}(\mathbf{k})$ [9]

$$w_{nm}(\mathbf{k}) = \langle u_{n,-\mathbf{k}} | \, \Theta \, | u_{m,\mathbf{k}} \rangle \tag{2.70}$$

where $u_{m,\mathbf{k}}$ is the cellular part of the Bloch state with wavevector $\mathbf{k}$. The band index m runs up to the the highest occupied band (preceding the band gap). Let us now focus on 2D TIs (also called the "Quantum Spin Hall" insulators). In the first Brillouin zone (1BZ) of such an insulator there are four special points, Λ_i, termed the "time reversal invariant momenta". These are the points that map onto themselves by the time-reversal operation (e.g. in a cubic lattice with period a these points would be $\mathbf{k} = (0,0), (\pi/a, 0), (0, \pi/a)$ and $(\pi/a, \pi/a)$). The value of the topological invariant $\mathcal{Z}_2 = \nu$ is [9]

$$(-1)^{\nu} = \prod_{i}^{4} \frac{\mathrm{Pf}[w(\Lambda_i)]}{\sqrt{\det[w(\Lambda_i)]}} \tag{2.71}$$

where Pf is the Pfaffian of the matrix. The above expression is cumbersome to use however it greatly simplifies in the presence of inversion symmetry. In this case the eigenstates of the Hamiltonian can be chosen to have definite parity (see 2.3.4) and the formula for calculating the invariant simplifies to

$$(-1)^{\nu} = \prod_{i}^{4} \prod_{n}^{N} \xi_{2n}(\Lambda_i) \tag{2.72}$$

where the second product is over every other occupied band, i.e. $n = 1, 3...$ – up to the band gap and $\xi_{2n}(\Lambda_i)$ is the parity eigenvalue of the state in $2n$-th band with $\mathbf{k} = \Lambda_i$. Both formulae (2.71) and (2.72) can be easily extended to the 3D case [9]. The only difference in this case is that there are now eight special points, Λ_i, in the 1BZ.

2.4.3 Crystalline topological insulators

Above we considered TIs which relied on time-reversal symmetry however a topological phase can be achieved using spatial (crystal) symmetries [62]. Here orbital (pseudospin) degrees of freedom play the same role as that of spin in TIs [63]. Such materials became known as topological crystalline insulators (TCIs) – see [64] for review. One of the first TCIs to be discovered was SnTe [65]. This is a material with rocksalt lattice where the mirror symmetry with respect to $\{110\}$ planes gives rise to the topological phase. Let us consider a plane in the 1BZ which is invariant under the mirror operation. The Bloch states in this plane will also be eigenstates of the mirror operation, M ($M^2 = -1$) with

eigenvalues $\pm i$ [65]. One can then calculate the Chern number C_{+i} for all the bands n_{+i} below the band gap which have eigenvalue $+i$ as follows:

$$C_{+i} = \sum_{n_{+i}} \frac{1}{2\pi} \int_{1BZ} d^2\mathbf{k} \nabla_{\mathbf{k}} \times (-i \langle u_{n_{+i}\mathbf{k}} | \nabla_{\mathbf{k}} | u_{n_{+i}\mathbf{k}} \rangle) \tag{2.73}$$

with $u_{n_{+i}}$ – the cellular wavefunctions. Calculating the analogous value C_{-i} for the occupied bands with the mirror eigenvalue $-i$ allows to obtain the mirror Chern number [65]

$$C_M = (C_{+i} - C_{-i})/2 \tag{2.74}$$

which is the topological invariant for the system with the given mirror symmetry. For SnTe the mirror Chern number C_M takes non-zero values meaning the material is not a trivial insulator. It is important to stress that the invariant C_M is defined only in the presence of given symmetry. Therefore the resultant surface states will be susceptible to spatial disorder and not as robust as in the case of TI. For clean surfaces however they will be spin-momentum locked.

2.4.4 Photonic topological insulators

Soon after the discovery of electronic TIs it was realized that analogous phases can be made with photonic crystals [66]. However, for bosons topological classification is different. Namely, for photons $\Theta^2 = 1$ which means that one cannot have an crossing of edge bands protected by the Kramers theorem 2.3.5. As a result one cannot realize a photonic TI based just on the time-reversal symmetry as one can do for electrons [43]. Luckily, one can realize other topological phases – for review see [43, 67, 68]. In particular, 2D topological phases have been made using photonic crystals made of ferrimagnetic materials placed in a magnetic field [46, 47]. These designs do not rely on crystal symmetry for topological protection. They can be seen as analogues of the Quantum Hall effect for electrons where a single unidirectional edge band exists due to the broken time-reversal symmetry. An alternative approach is to make use of crystal symmetry to realize a topological photonic phase. These photonic TCI phases have been achieved in a number of designs [48, 51]. Their edge states display spin-momentum locking however, as discussed in 2.4.3, they are sensitive to spatial disorder. The advantage of photonic TCIs is that they can be realized with simple dielectric materials can often be scaled to operate at the frequency of interest.

Chapter 3

Tight-binding studies of topological insulator nanoparticles

Introduction

The main signature of a TI is having robust surface states. These states arise because the topological invariant (non-zero value inside the TI) has to change at the boundary with a trivial insulator (zero invariant). The value of the invariant can only change if the bulk gap closes which happens at the boundary resulting in the surface states – see 2.4.1. Analytically, it is possible to find the surface spectrum of a slab for the (100) family of surfaces [36]. However, there also exist theoretical studies [20, 37] that show that the Dirac cone only gets moderately distorted on higher index surfaces. The topological protection of such states is established for continuous surface bands of bulk TI samples using tight-binding models [69–71]. It manifests in the fact that the states are delocalized and sustain a certain degree of disorder in contrast to ordinary ones. Experimentally, this results in the absence of backscattering as observed in scanning tunneling microscopy experiments [72].

The question then arises what happens in quantum confined TIs. By analogy to quantum dots we might expect the surface bands to become discretized. However, it is not clear whether the states remain protected in this case. From this perspective one might think that confinement destroys the surface states. However, for a clean sample this only happens once the states on the opposite surfaces start overlapping due to small thickness. This occurs due to the finite penetration of the surface states into the bulk (decay length ~ 1 nm). In Bi_2Se_3 thin films the states were found to hybridise

for thicknesses below 5 nm [35]. For thinner samples the states are pushed out of the bulk gap and disappear which can be viewed as the sample having not enough material to ensure the topological protection of the states. In the present chapter we study topological protection in TI nanoparticles motivated by the fact that for technological applications we ideally want to make use of the surface states at the smallest scale possible.

The first section of this chapter is devoted to the analytical solution for a TI nanowire. We first reproduce a derivation of the surface spectrum from literature [3]. We then extend the model to add the effects of a magnetic field – which is shown to close and reopen a surface gap in agreement with other analytical models [40] and experiment [73]. Next we proceed to show how the protection against backscattering holds for the surface states described by the model. The procedure is then repeated for spherical TI nanoparticles in which case the quantum confinement leads to a discrete spectrum of surface states. The analytical solution [4, 41] for the surface states of the sphere have been confirmed with tight-binding calculations in [4] and the present work. By analogy with a 3D quantum well the momentum quantum numbers for the surface states are now discrete. Furthermore, the states closest to the Dirac point have degeneracy of two suggesting that they are protected against elastic backscattering into each other to first order.

The second section of this chapter supports the analytical results for TI nanoparticles with computer simulations. Because density functional theory or GW calculations would be prohibitively expensive we used a tight-binding approach. After a careful review of available models [3, 74, 75] we chose the optimal one in terms of accuracy and complexity [74] and found it to agree well with analytical results for Bi_2Se_3 nanoparticles. Then we performed statistical studies of how surface states respond to disorder. Our main finding is that the discrete surface states in topological nanoparticles have the same level of protection as their continuous counterparts in bulk crystals [2]. This in turn suggests such states will stay delocalized even in the presence of surface imperfections and thus will display the desired properties. The results of this chapter have been published in [2].

3.1 TI wire analytical solution

The first nanoparticles to be investigated were TI nanowires (TINWs) – infinitely long TIs of cylindrical cross section. Compared with the planar surface there are now several bands due to the quantisation of motion in azimuthal direction [3,38–40]. These bands reduce to a single Dirac cone in the limit of large

radius. The ideal cylindrical shape is not important as qualitatively the same results were obtained for rectangular nanowires – with tight-binding [3, 39] and a patch-like approach of diagonalising the states on different faces with continuity imposed along the edges [36]. Several insightful results can be obtained analytically for TI nanowires using $\mathbf{k}\cdot\mathbf{p}$ theory 2.1.2. These results are useful to verify the tight-binding models of nanoparticles later on. We start by considering a TI nanowire as a simpler case. We briefly describe how the surface states can be derived from the bulk $\mathbf{k}\cdot\mathbf{p}$ Hamiltonian using a model from literature. We then improve the model by adding a magnetic field to it and also show that the surface states are protected from elastic backscattering to first order.

3.1.1 Surface band structure of the TI wire

Here we find the wavefunctions and surface energy spectrum on the surface of TINW using a model from literature. We focus on Bi_2Se_3 which is a widely used time-reversal invariant TI (see 2.4.2). We start from the low energy four band $\mathbf{k}\cdot\mathbf{p}$ Hamiltonian for bulk Bi_2Se_3. The basis used is [76]

$$|1\rangle = |\mathrm{Bi}^+, 1/2\rangle \quad |2\rangle = |\mathrm{Se}^-, 1/2\rangle \quad |3\rangle = |\mathrm{Bi}^+, -1/2\rangle \quad |4\rangle = |\mathrm{Se}^-, -1/2\rangle \tag{3.1}$$

where $|\mathrm{Bi}^+, 1/2\rangle$ means that the state has "+" parity (the material has inversion symmetry – see 2.3.4) is formed from $p_{x,y,z}$ orbitals of Bi atom (form the conduction band) and has angular momentum $m_j = 1/2$ [76] proportional to its spin [20] and likewise – for Se (whose $p_{x,y,z}$ orbitals form the valence band). In this basis the Hamiltonian was found by Liu *et al.* [76] using selection rules (see 2.3.3) to be

$$\begin{pmatrix} m(\mathbf{k}) + \epsilon(\mathbf{k}) & Bk_z & 0 & Ak_- \\ Bk_z & -m(\mathbf{k}) + \epsilon(\mathbf{k}) & Ak_- & 0 \\ 0 & Ak_+ & m(\mathbf{k}) + \epsilon(\mathbf{k}) & -Bk_z \\ Ak_+ & 0 & -Bk_z & -m(\mathbf{k}) + \epsilon(\mathbf{k}) \end{pmatrix} \tag{3.2}$$

where $m(\mathbf{k}) = m_0 + m_1 k_z^2 + m_2(k_x^2 + k_y^2), \epsilon(\mathbf{k}) = c_0 + c_1 k_z^2 + c_2(k_x^2 + k_y^2)$ and $k_\pm = k_x \pm i k_y$. The $m(\mathbf{k})$ term describes the parabolic dispersion while the $\epsilon(\mathbf{k})$ term represents asymmetry between the valence and conduction bands. The off-diagonal terms $\propto A, B$ (as well as the choice of the basis states) are dictated by the spin-orbit coupling in the material. $A \neq B$ arises because Bi_2Se_3 is layered with layers assumed to pile up in z direction. The parameters entering the Hamiltonian (3.2) can found from DFT simulations [76]. Using the envelope function approximation one can re-apply it to the cylinder.

In the following we closely follow the derivation of Imura *et al.* [3].

The first step is to drop the $\mathbb{I}\epsilon(\mathbf{k})$ term in Eq. 3.2 altogether. This term adds a parabolic dispersion $O(k^2)$ and breaks the particle hole symmetry [20]. As a result the spectrum is symmetric around $E = 0$. Moreover, the problem becomes much more tractable without sacrificing too much of an accuracy, e.g. in case of a planar TI surface the main effect of the $\mathbb{I}\epsilon(\mathbf{k})$ close to $E = 0$ is to change the linear slope of the Dirac cone [77]. Let us now switch from Cartesian coordinates to cylindrical ones so that in Eq. 3.2 k_x, k_y, k_z are replaced by linear combinations of k_r, k_ϕ, k_z. Assuming the cylinder's axis parallel to the z axis we now split the Hamiltonian (3.2) into two contributions. One contains the constant terms and derivatives normal to the surface (k_r). The other contains derivatives parallel to the surface (k_ϕ, k_z) [3]:

$$H = H_\perp + H_{||} \tag{3.3}$$

The reason for doing so is that the Dirac point determined by $H_\perp$ represents a much higher energy scale than the spacing between the surface states in the Dirac cone determined by $H_{||}$. For this reason we find the solution for $H_\perp$ and then treat $H_{||}$ as a perturbation. For $k_z, k_\phi = 0$ the perpendicular part of the Hamiltonian is given by [3]

$$H_\perp = \begin{pmatrix} m_\perp & 0 & 0 & Ae^{-i\phi}k_r \\ 0 & -m_\perp & Ae^{-i\phi}k_r & 0 \\ 0 & Ae^{i\phi}k_r & m_\perp & 0 \\ Ae^{i\phi}k_r & 0 & 0 & -m_\perp \end{pmatrix} \tag{3.4}$$

where $m_\perp = m_0 + m_2 k_r^2$. The next step is to transit from $\mathbf{k} \cdot \mathbf{p}$ to envelope-function approximation (see 2.1.3) for the confined directions. For the TINW, r forms the confined direction while periodic boundary conditions are applied along ϕ and z. To make this transition, one substitutes the crystal momentum k_r with its real space derivative [55]. Thus we set $k_r \to -i\partial_r$ and $k_r^2 \to \partial_r^2$ neglecting the term $\propto (1/r)\partial_r$. The latter is a good approximation assuming the states decay away from the surface as $e^{\kappa(r-R)}$ and the decay constant satisfies $\kappa^{-1} \ll R$, the radius of the cylidner. Then for $r < R$ we substitute the ansatz $e^{\kappa(r-R)}$ where $\kappa > 0$ and solve $|H_\perp - \mathbb{I}E| = 0$ to obtain two eigenvalues [3]:

$$E = \pm\sqrt{m_\perp^2 - A^2\kappa^2} \tag{3.5}$$

For $E = 0$ ($m_\perp^2 = A^2\kappa^2$) there are only two distinct eigenspinors [3]:

$$|+\rangle = (-ie^{-i\phi},\ 0,\ 0,\ 1)^T/\sqrt{2}, \quad |-\rangle = (0,\ ie^{-i\phi},\ 1,\ 0)^T/\sqrt{2} \tag{3.6}$$

The condition $E = 0$ for the energy of the Dirac point leads to four possible values of κ [3]

$$\kappa_{1,2} = \frac{-A \pm \sqrt{A^2 + 4m_0m_2}}{2m_2} \qquad \kappa_{3,4} = \frac{A \pm \sqrt{A^2 + 4m_0m_2}}{2m_2} \tag{3.7}$$

For Bi_2Se_3 we know from DFT calculations [76] that $m_2, A > 0$ and $m_0, A^2 + 4m_0m_2 < 0$, so only $\kappa_{3,4}$ correspond to decaying solutions. Thus, for $r \leq R$ an arbitrary surface state has a general form [3]:

$$|\psi\rangle = (e^{\kappa_3(r-R)} - e^{\kappa_4(r-R)})(c_+ |+\rangle + c_- |-\rangle) \tag{3.8}$$

where the radial solution ensures that the probability density is zero at the boundary of the cylinder and peaks near the edge. The states are localised near the surface, $Re[\kappa_{3,4}] \approx 0.5$ nm^{-1} (using the parameters from [76]) so for radii larger that a few nm we can drop the radial dependence and set $r = R$. Then, applying the envelope function approximation azimuthally we have

$$k_\phi \to \frac{-i}{R}\partial_\phi \tag{3.9}$$

The azimuthal part of the Hamiltonian Eq. 3.2, $H_{||}$, given by [3]

$$H_{||} = \begin{pmatrix} m_{||} & Bk_z & 0 & -iAe^{-i\phi}k_\phi \\ Bk_z & -m_{||} & -iAe^{-i\phi}k_\phi & 0 \\ 0 & iAe^{i\phi}k_\phi & m_{||} & -Bk_z \\ iAe^{i\phi}k_\phi & 0 & -Bk_z & -m_{||} \end{pmatrix}, \tag{3.10}$$

where $m_{||} = m_1k_z^2 + m_2k_\phi^2$. Projecting the resultant eigenvalue equation

$$H_{||}\,|\psi\rangle = E\,|\psi\rangle \tag{3.11}$$

onto the unperturbed eigenspinors given by Eq. 3.6, [3] we get

$$\begin{pmatrix} 0 & -iBk_z + A(k_\phi - \frac{1}{2R}) \\ iBk_z + A(k_\phi - \frac{1}{2R}) & 0 \end{pmatrix} \begin{pmatrix} c_+ \\ c_- \end{pmatrix} = E \begin{pmatrix} c_+ \\ c_- \end{pmatrix} \tag{3.12}$$

The constant terms are due to the Berry phase of π that an electron in a spin-locked surface state acquires on going around the circumference of the cylinder. It can be made implicit by making a substitution $\mathbf{c} = e^{i\phi/2}\chi$ to arrive at

$$(A\sigma_x k_\phi + B\sigma_y k_z)\chi = E\chi \tag{3.13}$$

where A, B have dimensions of $[E][L]$ and k_z, k_ϕ have dimensions of $[L]^{-1}$. For convenience we relabel $k_z \to k$, $k_\phi \to m/R$, $B \to v_z$ and $A \to Rv_\phi$. In this notation the eigenenergies of Eq. 3.13 are given by

$$E_{skm} = s\sqrt{(kv_z)^2 + (mv_\phi)^2} \tag{3.14}$$

where $s = \pm 1$, k is continuous and $m = \pm 1/2, \pm 3/2...$ to ensure azimuthal periodicity after switching from Eq. 3.12 to Eq. 3.13. The half-integer values of m lead to an energy gap in the surface spectrum. The obtained energy dispersion Eq. 3.14 illustrated in Fig. 3.2 shows good agreement with tight-binding simulations [3, 39]. The normalized coefficients of Eq. 3.13 are given by

$$|skm\rangle = \chi_{skm}\frac{e^{i(kz+m\phi)}}{\sqrt{2\pi RL}} = \frac{1}{\sqrt{2}}\left(-s\frac{i\sqrt{v_z^2k^2 + v_\phi^2m^2}}{v_z k - iv_\phi m}, 1\right)^T \frac{e^{i(kz+m\phi)}}{\sqrt{2\pi RL}} \tag{3.15}$$

where $R \ll L$, the length of the cylinder (effectively infinite). Importantly, the eigenstates with $\pm m$ are symmetric in the sense $\chi^\dagger_{skm}\chi_{sk(m+1)} = \chi^\dagger_{sk-m}\chi_{sk-(m+1)}$ and $\chi^\dagger_{skm}\chi_{sk(m-1)} = \chi^\dagger_{sk-m}\chi_{sk-(m-1)}$ $(m > 0)$. This is in contrast to the surface states obtained for an alternative surface Dirac Hamiltonian used by [39] which was not derived from the Bi_2Se_3 Hamiltonian. For this reason we continue using the Dirac Hamiltonian of Imura *et al.* whose derivation has been presented above. For small radii of the cylinder the degeneracy of the states increases as $4, 8, 12...$ away from the Dirac point. Thus the degeneracy is proportional to the energy difference from the Dirac point. The same occurs for continuous states on a planar surface. The dispersion there is linear and the degeneracy is proportional to the radius of the circular cross section of the Dirac cone at a given energy. Thus degeneracy pattern of the TINW can be interpreted as increasing the circumference of the surface Dirac cone which has been discretised by quantum confinement. The zero density of states in the Dirac cone on the planar surface manifests as a surface energy gap in the case of the cylinder and also the sphere as we will see later.

3.1.2 Topological protection of the wire's surface states

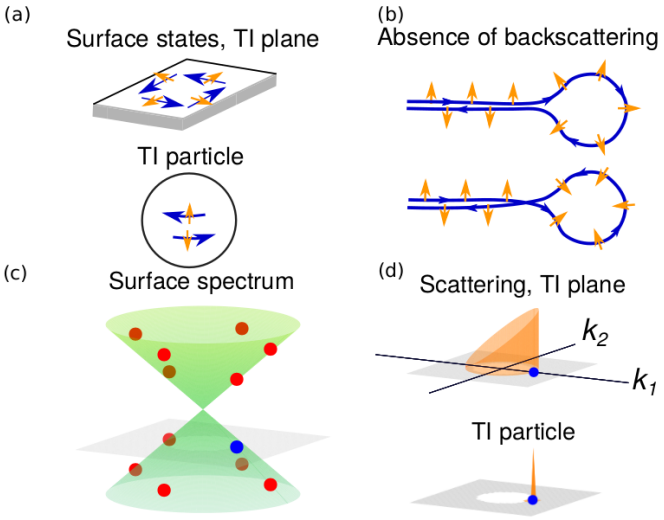

Figure 3.1: (a) Topological surface states have correlation between spin and momentum. (b) This spin-momentum locking leads to destructive interference of two possible backscattered paths. (c) Planar surface of a TI has a Dirac cone which turns into discrete states in quantum confined TI nanoparticles. (d) Matrix element for elastic backscattering of a surface state (blue dot) equally vanishes in the cases of the planar surface and the spherical nanoparticle. Figure from [2], 2017, American Physical Society.

Let us start by reviewing how disorder affects the electrons on a flat surface of a TI sample. In the perfect crystal their wavefunction is extended but for strong enough disorder it becomes localized. The ability of an electron to scatter backwards serves as a precursor to localization. This occurs because when backscattering is possible then constructive interference of backscattering paths adds a correction to diffusive motion making an electron more likely to return to its original position [78]. For TIs backscattering can be studied analytically. Here a major role is played by the spin-momentum locking of the states 2.4.1. This means that the states with opposite momenta have opposite spins – as required by time-reversal symmetry (see Fig. 3.1(a)). This protects the states from backscattering due to the destructive interference between the two possible paths [8, 74] as shown in Fig. 3.1(b) and leads to antilocalization. To see the absence of backscattering explicitly let us consider the matrix elements for the event [2]. In the simplest case of Bi_2Se_3 the surface states form a single Dirac cone as shown in Fig. 3.1(c). Then, solving the $\mathbf{k}\cdot\mathbf{p}$ Hamiltonian [76] for a planar surface one obtains the surface wave functions of the form $|\psi\rangle = c_+|+\rangle + c_-|-\rangle$ where $|\pm\rangle$ are the two spinors whose coefficients depend on the crystal momentum, k: $\mathbf{c} = (c_+(k), c_-(k))^T$. The two spinors are related by the time-reversal operation, Θ: $\Theta|+\rangle = e^{i\alpha}|-\rangle$ and $\Theta|-\rangle = e^{i\beta}|+\rangle$ with $\alpha - \beta = \pm\pi$ to ensure that $\Theta^2 = -1$ as required for fermions 2.3.5.

We now consider the protection of the TINW surface states derived above. To show the protection explicitly we first prove that the eigenspinors $|+\rangle$ and $|-\rangle$ in Eq. 3.14 form a Kramers pair. This can be shown using the time-reversal operator, Θ, represented by [20, 76] whose form follows from the basis states used (3.1)

$$\Theta = \begin{pmatrix} 0 & 0 & 1 & 0 \\ 0 & 0 & 0 & 1 \\ -1 & 0 & 0 & 0 \\ 0 & -1 & 0 & 0 \end{pmatrix} K \tag{3.16}$$

with K being the complex conjugation operator. The time-reversal operator satisfies

$$\Theta^2 = -1 \tag{3.17}$$

It relates the eigenspinors in Eqn. 3.6 via

$$\Theta |+\rangle = -ie^{i\phi} |-\rangle \tag{3.18}$$

$$\Theta |-\rangle = ie^{i\phi} |+\rangle \tag{3.19}$$

which proves that they form a Kramers pair. The fact that the surface states are protected against non-magnetic disorder can be shown using perturbation theory. Let us consider a generic time-reversal symmetric perturbation V which satisfies

$$V = \Theta V \Theta^{-1}, \quad V^\dagger = V \tag{3.20}$$

We now also note that the two Kramers partners satisfy

$$\langle -| \Theta |+\rangle = -ie^{i\phi} \langle -|-\rangle = -ie^{i\phi} = -ie^{i\phi} \langle +|+\rangle = - \langle +| \Theta |-\rangle \tag{3.21}$$

$$\langle \pm| \Theta |\pm\rangle = - \langle \pm| \Theta |\pm\rangle = 0 \tag{3.22}$$

which equally follows from a more general property of Θ that [9]

$$\langle p| \Theta |q\rangle = - \langle q| \Theta |p\rangle \tag{3.23}$$

This together with the properties of V in Eq. (3.20) and relations between $|+\rangle$, $|-\rangle$ leads to

$$\langle +|\, V\, |-\rangle = \langle +|\, \Theta V \Theta^{-1}\, |-\rangle = \langle +|\, \Theta V \Theta^{-1} ie^{-i\phi}\Theta\, |+\rangle = ie^{-i\phi}\, \langle +|\, \Theta V\, |+\rangle = -ie^{-i\phi}\, \langle +|\, V^{\dagger}\Theta\, |+\rangle$$

$$= -ie^{-i\phi}\, \langle +|\, V\Theta\, |+\rangle = -ie^{-i\phi}\, \langle +|\, V(-ie^{i\phi})\, |-\rangle = -\langle +|\, V\, |-\rangle = 0 \tag{3.24}$$

Thus a time-reversal symmetric perturbation cannot mix the eigenspinors to first order and therefore the surface states of the TINW are protected against backscattering from non-magnetic impurities and disorder. The latter follows because the coefficients for states (k, m) and $(-k, -m)$ are orthogonal as follows from Eq. 3.15.

One way to check the model described above is to incorporate a magnetic field into it. Then at some points surface bands with linear dispersion are expected to form [39, 40]. To check for this we now modify the model of Imura *el at.* by adding a static uniform magnetic field via Peierls' substitution:

$$\hbar\mathbf{k} \to \hbar\mathbf{k} - q\mathbf{A} \tag{3.25}$$

For a magnetic field in z-direction a suitable gauge is

$$\mathbf{A} = (x\mathbf{j} - y\mathbf{i})\frac{B}{2} \tag{3.26}$$

There are two relevant wavevectors in the xy plane, one of them, k_r, is unchanged while the other, k_ϕ, becomes

$$k_\phi \to k_\phi - \frac{qBr}{2\hbar} \tag{3.27}$$

Note that because a magnetic field is a time-reversal breaking perturbation it enters Eq. 3.13 as an off-diagonal term. Now, because for the surface states $r \approx R$ we have

$$k_\phi - \frac{qBr}{2\hbar} \approx \frac{1}{R}(-i\partial_\phi - \frac{qB\pi R^2}{2\pi\hbar}) = \frac{1}{R}(-i\partial_\phi + \frac{\Phi}{\Phi_0}) \tag{3.28}$$

where Φ is the flux through the cylinder and $\Phi_0 = h/e$. Thus for a flux $\Phi = \Phi_0/2$ a band crossing occurs for $m = -1/2$. This particular band obtains a linear dispersion

$$E_{sk-1/2} = sv_z k \tag{3.29}$$

as shown in Fig. 3.2 and its eigenstates given by

$$\chi_{sk-1/2}\frac{e^{ikz}}{\sqrt{2\pi RL}} = \frac{1}{\sqrt{2}}\left(-s\frac{k}{|k|}, 1\right)^T \frac{e^{ikz}}{\sqrt{2\pi RL}} \tag{3.30}$$

Thus for one particular band the magnetic field compensates the π Berry phase due to curvature of the cylindrical surface. This is also seen in tight-binding calculation [3, 39]. The single band that arises in case of $\Phi = \Phi_0/2$ has linear dispersion with each energy level being doubly degenerate. As a consequence, the states in this band are protected against elastic backscattering (to first order). This follows from their coefficients' wavefunctions given by Eq. 3.30 and the resulting conductance of e^2/h due to this particular band has been observed [73].

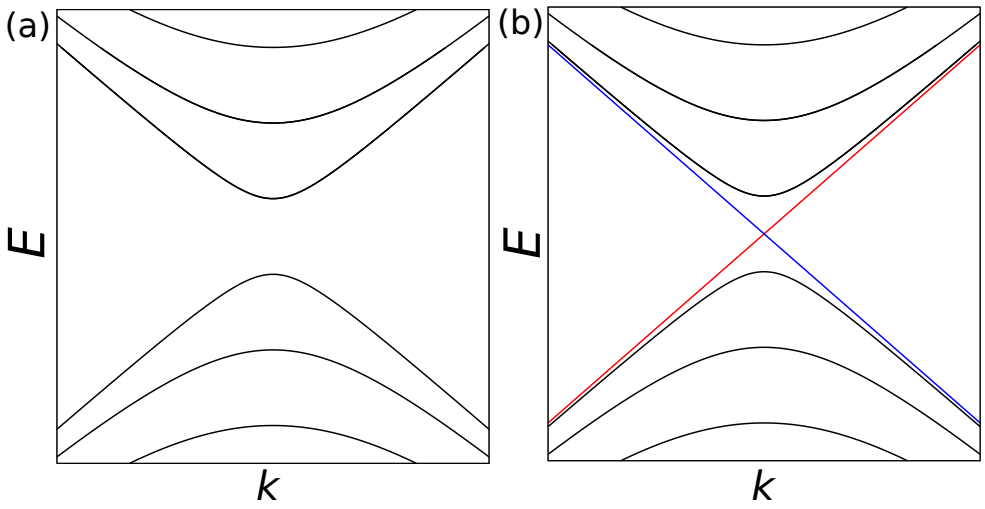

Figure 3.2: Left: Band structure of a topological insulator nanowire. Right: The same with magnetic field flux of half a flux quantum, $\Phi = h/2e$ threading the wire parallel to its axis. A band with linear dispersion appears where states propagate along the cylindrical wire without backscattering.

3.1.3 TI particle surface spectrum

In this section we briefly outline the derivation of the surface spectrum for a spherical TI [4]. We then use these analytical results to show that surface states in this case are also protected. The wavefunctions for the spherical TI nanoparticle (TINP) were obtained by Imura *et al.* starting from the Hamiltonian (3.2) [4] in a way very similar to that for the TINW described in the previous section. To summarise, the $\epsilon(\mathbf{k})$ term was again neglected and the authors further set $B = A$ to simplify the solution in spherical coordinates. As in the TINW case resolving $H = H_\perp + H_{||}$ one first obtains the

two eigenspinors of $H_\perp$ [4] which for the sphere are given by

$$|+\rangle = \frac{1}{2}\left((1,\ -i)e^{-i\phi/2}\cos\frac{\theta}{2},\quad (1,\ -i)e^{i\phi/2}\sin\frac{\theta}{2}\right)^T \tag{3.31}$$

$$|-\rangle = \frac{1}{2}\left((1,\ i)e^{-i\phi/2}\sin\frac{\theta}{2},\quad (-1,\ -i)e^{i\phi/2}\cos\frac{\theta}{2}\right)^T \tag{3.32}$$

These are the states at $E = 0$ for which $H_{||}$ can be treated as perturbation. Projecting $H_{||}$ onto $|+\rangle$ and $|-\rangle$ yields a surface Dirac equation analogous to Eq. (3.13) for the wire. The resultant surface states have energies [4]

$$E_{snm} = s\frac{A}{R}\left(n + |m| + \frac{1}{2}\right) \tag{3.33}$$

where R is the radius, $A = 3.0\,\text{eV}\cdot\text{Å}$ is a constant obtained from DFT calculations [76] and the quantum numbers take values $s = \pm$, $n = 0, 1, 2...$, $|m| = 1/2, 3/2...$ with m – the z component of the total angular momentum. Thus the states are equally spaced in energy above (below) the Dirac point, $E = 0$. Their degeneracy increases as $2, 4, 6, 8...$ away from the Dirac point with states at a given energy forming Kramers pairs. Thus, the spectrum can be interpreted as a discretised version of the surface Dirac cone from the parent TI (Bi_2Se_3). The linear increase in degeneracy can be understood as increasing the circumference of the cone when going away from the Dirac point. For details of the derivation and the form of coefficients entering the general wavefunction, Eq. 3.8, see Appendix A.2.3, e.g. for the first two states below the $E = 0$ they are given by

$$\mathbf{c}_{-\,0\,1/2} = \frac{e^{i\phi/2}}{\sqrt{4\pi R^2}}(\cos\frac{\theta}{2},\ \sin\frac{\theta}{2})^T \tag{3.34}$$

$$\mathbf{c}_{-\,0\,-1/2} = \frac{e^{-i\phi/2}}{\sqrt{4\pi R^2}}(\sin\frac{\theta}{2},\ -\cos\frac{\theta}{2})^T \tag{3.35}$$

3.1.4 Protection of the particle's surface states

Just as in the case of cylinder the two eigenspinors 3.31 and 3.32 are related by the time-reversal operation:

$$\Theta\,|+\rangle = |-\rangle \tag{3.36}$$

$$\Theta\,|-\rangle = -\,|+\rangle \tag{3.37}$$

which proves that they form a Kramers pair. As in the case of cylinder we now consider a general time-reversal symmetric perturbation V satisfying 3.20. We also note that the two Kramers partners again satisfy (3.21) and (3.22). Together with properties of V and relations between $|+\rangle$, $|-\rangle$ above this leads to

$$\langle +| V |-\rangle = \langle +| \Theta V \Theta^{-1} |-\rangle = \langle +| \Theta V |+\rangle = -\langle +| V \Theta |+\rangle = -\langle +| V |-\rangle = 0 \tag{3.38}$$

Thus a time-reversal symmetric perturbation cannot mix the eigenspinors and therefore the surface states of the TINP are protected elastic against scattering from non-magnetic impurities and disorder to first order. The latter follows because the coefficients of backscattered partners are orthogonal (see, e.g. Eqns. 3.34, 3.35). As such, the doubly degenerate states immediately below (and also above) the Dirac point are particularly interesting. Their z components of the angular momenta are opposite ($m = \pm$) but they cannot backscatter having opposite spins given by Eqns. 3.34 and 3.35. Therefore these states should be very stable against disorder and impurities. They will be our focus when considering the optical properties of the TINP in the next chapter. To summarise, the existence of the surface states is guaranteed by the non-trivial topology of the bulk band structure and time-reversal symmetry. The inverted band gap in the topological insulator on one side and the normal band gap in the trivial insulator on the other is what gives rise to states which should be delocalized over the whole surface.

3.2 Tight-binding solution of TI nanoparticles

3.2.1 Coarse-grained tight-binding model and its limitations

In general, there have not been many studies of TI nanoparticles [4, 79]. Moreover, the only investigation of disorder in TI nanoparticles focused on how it affects the energies of the surface states using an analytical model [79]. In contrast, the tight-binding method has been used for several studies of disorder and localization on the planar TI surface [69–71]. The latter is in many ways advantageous over the analytical approach: it is not restricted only to the surface states with energies in the middle of the band gap, can resolve details at atomic level and is able to treat particles of different shapes as well as those with rough surfaces. Ideally we would want to use more elaborate methods such as density-functional theory or GW however even for the smallest TI nanoparticles possessing surface

states they are prohibitively expensive. This is because a TI has to be at least a few nm in size to display topological properties [35, 39, 80]. The way around this is to use a DFT-parametrised tight-binding model. While there exist DFT-parametrised models of common TIs [81] our first step is to follow a simpler route and used a coarse grained tight-binding model of Bi_2Se_3 [3, 4] given by (see Appendix A.2.4):

$$H = \tau_z \left[m_0 + \frac{2}{L^2} \sum_i m_2 (1 - \cos k_i L) \right] + \frac{1}{L} A \tau_x \sum_i \sigma_i \sin k_i L \tag{3.39}$$

where $i = x, y, z$ and m_0, m_2, A are material-dependent constants, τ, σ are the Pauli matrices corresponding to the orbital and spin degrees of freedom. $L \approx 4$ nm is the coarse graining length [80] so the averaging is made over several primitive unit cells of Bi_2Se_3. This Hamiltonian does not differentiate between Bi and Se atoms and reduces spin-orbit coupling effects to nearest-neighbour hops on a cubic lattice. It has been successfully used to simulate TI slabs. Fig. 3.3(a) shows a single Dirac cone as expected for the planar surface of Bi_2Se_3. However, the model struggles to reproduce the band structure of a TI nanowire as has been shown previously [3]. In the absence of a magnetic field such a nanowire is expected to show a gap in the surface spectrum (Eq. 3.14) which has been confirmed with other models [38–40] and experimentally observed [73]. In contrast, the coarse grained model considered shows a crossing in Fig. 3.3(b). This can be ascribed to the model's approximations however more accurate descriptions of TI nanoparticles are available as shown in the next subsection.

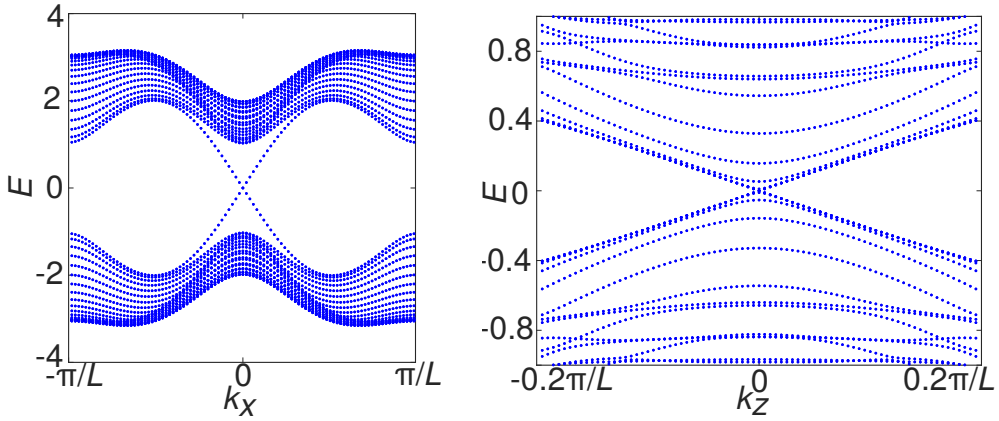

Figure 3.3: Coarse grained tight-binding model of Bi_2Se_3 [3]. (a) Bandstructure of a TI slab correctly shows a single Dirac cone. The slab is periodic in the xy plane (20 cells in thickness, $A/L = 1$, $2m_2/L^2 = 1$ and $m_0 = -1$) (b) Reproducing the band structure of a TI wire extended along z-axis [3] which incorrectly shows a Dirac crossing in the absence of a magnetic field (12 by 16 cells in cross section, $A_z/L = 0.7$, $A_{x,y}/L = 1$ $2m_2/L^2 = 1$ and $m_0 = -1$).

3.2.2 Fu-Kane-Mele fully microscopic tight-binding model

The failure of the coarse-grained tight-binding model for the TI nanowires shown above suggests that it is unsuitable for describing nanoparticles. To make up for that we use the microscopic tight-binding model of Fu-Kane-Mele [74]. This model does not rely on the slowly-varying envelope approximation of a four-band Hamiltonian as most other tight-binging models do [3, 69, 71]. While this toy model is not tied to a particular material it provides a microscopic description of TIs and reproduces many important features. As such, it has been successfully used to model TI slabs [70, 74] and nanowires [39, 82].

The atoms in the Fu-Kane-Mele model are arranged on a diamond lattice as shown in Fig. 3.5(a). Each atom carries a single (spin-degenerate) s-orbital. Hoppings between the atoms are described by the following Hamiltonian

$$H = t \sum_{\langle i,j \rangle} |i\rangle \langle j| + \frac{\lambda_{\mathrm{SOC}}}{4a^2} \sum_{\langle\langle i,j \rangle\rangle} |i\rangle \langle j| \, \sigma \cdot (\mathbf{d}_1 \times \mathbf{d}_2) \tag{3.40}$$

where the first term describes nearest neighbour hops. The second term includes next-nearest neighbour hops representing spin-orbit coupling. It mixes the spins through the operation of Pauli matrices, σ. It is direction-dependent through $\mathbf{d}_1$ and $\mathbf{d}_2$ which are the two nearest neighbour bonds leading to the next nearest neighbour atoms separated a lattice vector apart. The size of the cubic unit cell is $a = \sqrt{2}|\mathbf{a}_i| = 1$ and we use $t = \lambda_{SOC} = 1$ [70, 74] unless otherwise specified. This Hamiltonian describes a topological phase once we make the nearest neighbour bond along the [111] direction shorter by setting $t \to t + \delta t$ with $\delta t = 0.4t$ [74]. This opens a topological gap of size $E_{\mathrm{G}} = 2\delta t$ [74] at the X points in the first Brillouin zone – see Fig. 3.4. The geometry of the unit cell is shown in Fig. 3.5(a). We verified our implementation of the Fu-Kane-Mele model for a TI slab reproducing a single surface cone in the band structure for (111) surface termination [70]. In addition, we have also studied how disorder affects the surface states. This has been done by adding an on-site disorder potential term in the Hamiltonian of Eq. 3.40, $\sum_i V_i |i\rangle \langle i|$ where $V_i \in [-V_{\mathrm{D}} : V_{\mathrm{D}}]$. Such potentials taken from uniform distribution are known to yield the correct scaling behaviour in studies of Anderson localization [83]. In addition, they allow to compare our results with the previous studies of TI slabs [69–71]. We restrict disorder to one unit cell below the surface to represent possible defects and impurities. The results in Fig. 3.5(b-d) indicate that surface states become localized when $V_{\mathrm{D}} \approx E_{\mathrm{G}}$. These results agree with previous simulations of disorder on TI slabs with the Fu-Kane-Mele model [70] as well as

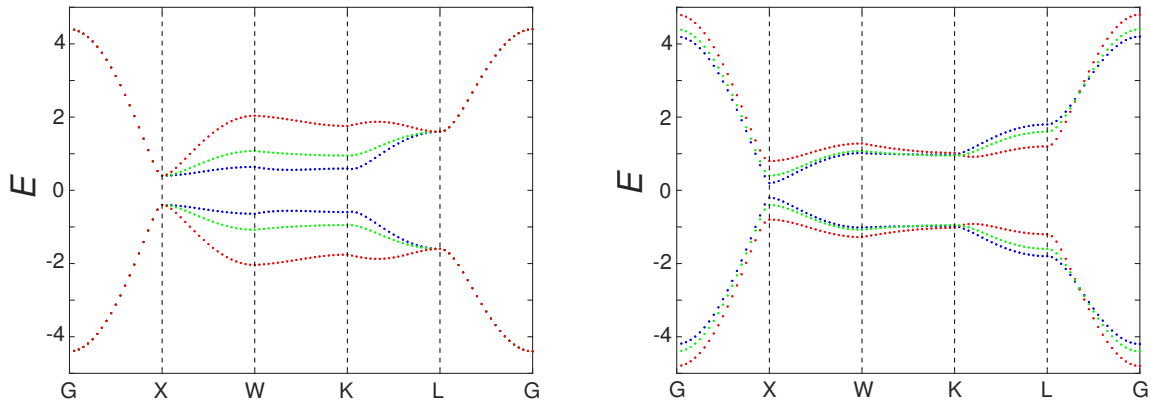

Figure 3.4: Left: Bulk band structure of the Fu-Kane-Mele model with $t = 1, \delta t = 0.4$ and three different spin-orbit coupling strengths: $\lambda_{SOC} = 0.5, 1$ (used), 2 (blue, green, red) Right: Bandstructure for $t = \lambda_{SOC} = 1$ and $\delta t = 0.2, 0.4$ (used), 0.8 (blue, green, red). The coordinates of $\Gamma = (0,0,0)$, $X = (1,0,0)$, $W = (1,1/2,0)$, $K = (3/4,3/4,0)$ and $L = (1/2,1/2,1/2)$ are given in units of $2\pi/a$.

coarse-grained tight-binding ones with slowly-varying potentials [69, 71]. In the next subsection they are compared against the robustness of the discrete states in topological nanoparticles.

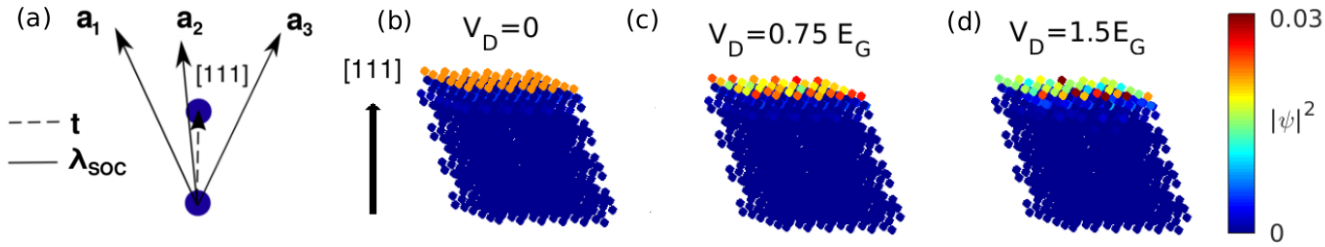

Figure 3.5: Fu-Kane-Mele microscopic tight-binding model. (a) The primitive unit cell with (next-) nearest-neighbour hoppings shown as (solid) dashed lines. (b-d) Supercell of a slab ($6 \times 6 \times 8$ primitive unit cells). Probability density of the surface states at the Dirac point. The states localize when the disorder potential strength, V_{D}, reaches the bulk band gap E_{G}. Figure from [2], 2017, American Physical Society.

3.2.3 Fu-Kane-Mele model applied to TI particles

Having checked our implementation of the model above and bearing in mind that it has been previously used for TI nanowires [39, 82] we proceed to apply it to the nanoparticles. We consider a spherical-like TI nanoparticle containing about 2500 atoms (a Bi_2Se_3 particle with the same number of atoms has a radius of 5 nm). It is large enough to support surface states as indicated by the spectrum in Fig. 3.6(a). The spectrum contains several pairs of surface states in the energy region corresponding to the bulk bang gap. These states decay exponentially from the boundary of the particle – see Fig. 3.6(b). Moreover, the states' energies scale as λ_{SOC}/R – in agreement with the analytical model

(Eq. 3.33) for Bi_2Se_3. The probability densities of the surface states close to $E = 0$ are concentrated at the two poles of the nanoparticle as seen in Fig. 3.6(d). One reason for these preferred directions arises from the way we construct the nanoparticle from primitive unit cells (see Appendix A.1.1). The other reason for the preferred direction is that one of the four nearest-neighbor bonds ([111]) is made shorter ($t \to t + \delta t$) just as in the slab case above. The latter factor dominates as seen from Fig. 3.6(e) where a different – $[\bar{1}\bar{1}1]$ bond was made shorter instead (see Appendix A.1.2 for other shapes). The surface states also depend on the size of the particle. For small particles they cover most of the area. On the other hand, for larger particles the states tend to concentrate at the two poles more. This can be understood by considering the limit of a very large particle. If such a particle had several faces then each face could be considered separately as a plane supporting its own Dirac cone.

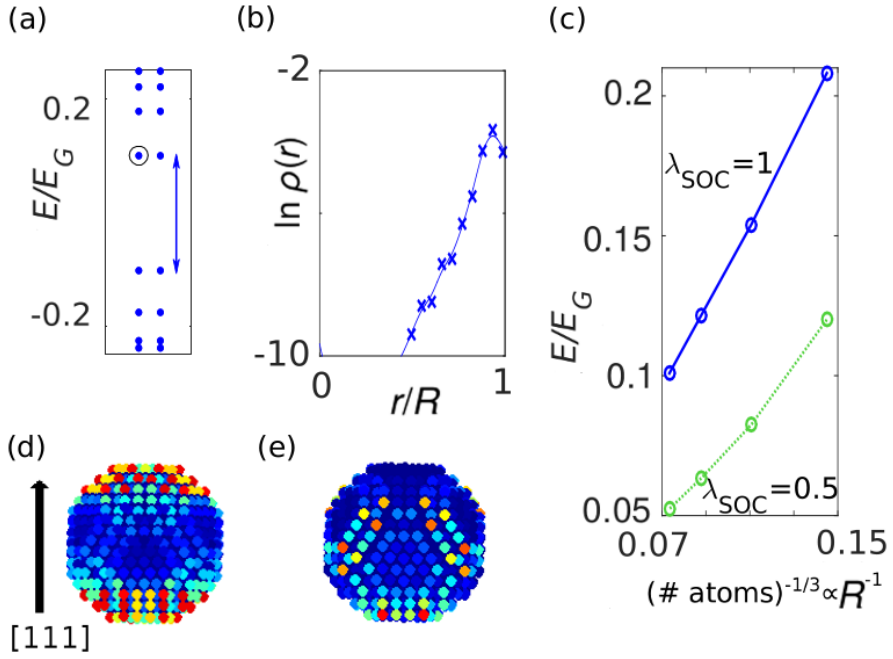

Figure 3.6: Surface states of a spherical TI nanoparticle simulated using the Fu-Kane-Mele model. (a) For energy values inside the bulk band gap there are pairs of surface states. (b) The encircled surface state decays exponentially away from the particle's boundary; $\rho(r) = \sum_{r_i=r} |\psi_i|^2$ with r_i – the radial coordinate of $i-th$ atom. (c) Its energy grows as λ_{SOC}/R in agreement with the analytical model (see text). (d) The wavefunction is delocalized over two poles as determined by the direction of the short bond – [111]. (e) Same as (d) but with the short bond along $[\bar{1}\bar{1}1]$ direction. Figure from [2], 2017, American Physical Society.

3.2.4 Disordered TI particle

To study the effects of disorder we add random on-site potentials to atoms just as we did for the slab above. These potentials are applied to the 700 outermost atoms (out of the total 2500) covering

the entire surface. With disorder strength, V_{D}, equal to E_{G}, the bulk band gap, the nanoparticle's spectrum still contains an energy gap and the states are still confined to the surface as seen from a representative example in Fig. 3.7(a,b) (for statistical averages of the radial wavefunction – see Appendix A.1.3). The statistical average for the gap between the states above and below $E = 0$ in Fig. 3.7(c) shows that the variation in energy of the states becomes comparable to the spacing of the levels when $V_{\mathrm{D}} > E_{\mathrm{G}}$. This provides a hint that localization occurs at disorder strengths of about $V_{\mathrm{D}} = E_{\mathrm{G}}$.

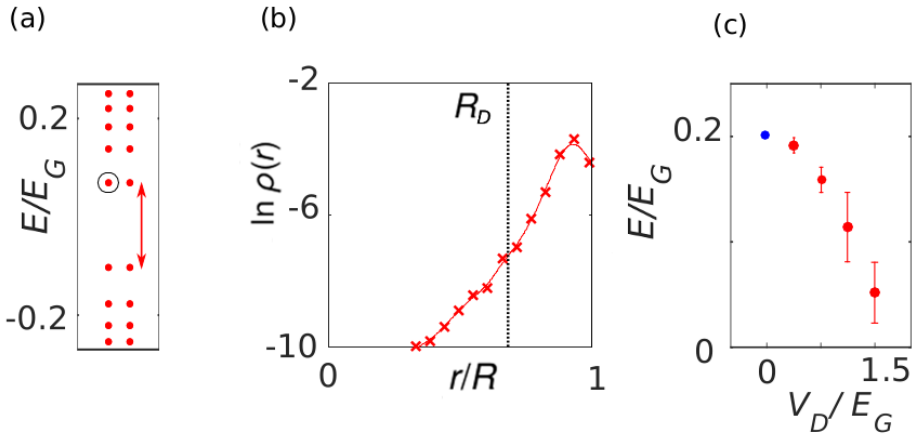

Figure 3.7: Disordered TI nanoparticle simulated with the Fu-Kane-Mele model. (a) The surface spectrum and (b) The decay of the state (encircled) away from the particle's boundary given by $\rho(r)$ for disorder potential strength $V_{\mathrm{D}} = E_{\mathrm{G}}$, the bulk band gap, shows little difference from the clean case; $\rho(r) = \sum_{r_i=r} |\psi_i|^2$ with r_i – the radial coordinate of the $i-th$ atom. All surface atoms with $r > R_{\mathrm{D}}$ carry disorder potentials. (c) Energy gap around $E = 0$ indicated by the arrow in (a) and Fig. 3.6(a). Each point is an average over 25 disorder realizations; error bars denote their standard deviations. Figure from [2], 2017, American Physical Society.

Localization of extended states in crystals is usually quantified using the inverse participation ratio. However, above we have seen how the surface states of the spherical TINP spread out over particular regions. This means we cannot rely on the inverse participation ratio often used for planar surfaces [70, 71]. In addition, defining the ratio for surface states requires imposing an ad hoc depth under the surface. Fortunately, we can make use of the inversion symmetry of the TI particle to invent an unbiased measure of localization. We define a symmetry deviation function, s_{D}, which acts as a measure of inversion symmetry breaking for a particular surface state ψ:

$$s_{\mathrm{D}} = \left| \sum_{i \in \mathrm{atoms}} |\psi_i|^2 \hat{\mathbf{r}}_{\mathbf{i}} \right| \tag{3.41}$$

where $\hat{\mathbf{r}}_{\mathbf{i}}$ is a unit vector towards atomic site i and $|\psi_i|^2$ is the probability of electron in state ψ

occurring at site i. Placing the origin at the center of the nanoparticle, we get $s_{\mathrm{D}} = 0$ for states on a clean surface. Any deviation from inversion symmetry leads to a non-zero value with the maximum of $s_{\mathrm{D}} = 1$ meaning that the state is localized at a single atom (or a chain of atoms in a particular radial direction). We then take care of any pathological cases by performing statistical averaging over many disorder realizations of a given strength V_{D}. The results shown in Fig. 3.8(a) indicate that for a spherical particle s_{D} saturates close to $V_{\mathrm{D}} = E_{\mathrm{G}}$ agreeing with the results above for the surface spectrum (Fig. 3.7(c)). This can be also be seen from the probability distributions plotted in Fig. 3.8(b). The same particle but with a smaller λ_{SOC} and surface disorder has less robust states. This is because smaller spin-orbit coupling strength ($\lambda_{\mathrm{SOC}} = 1/2$) leads to a smaller bulk band gap, E_{G} (see Appendix A.1.4 for the spectrum with $\lambda_{\mathrm{SOC}} = 0$). Finally, bulk disorder (all atoms within R_{D} in Fig.3.7(b) carry disorder) has a much weaker effect on the states being confined to the surface.

The advantage of using a tight-binding model is that it allows us to investigate particles of shapes too difficult for analytical treatment. We start by studying the effects of surface roughness added on top of an otherwise spherical particle (700 "roughness" atoms out of total 1900 atoms – for details see Appendix A.1.5). Because random atomic-scale roughness breaks the inversion symmetry the states have $s_{\mathrm{D}} \neq 0$ even for $V_{\mathrm{D}} = 0$ however they become localized at the same value of V_{D} as those with a smooth surface seen above – compare Fig. 3.9(a) and Fig. 3.8. These results are illustrated by probability distributions in Fig. 3.9(b). Finally, we consider localization of the surface states in particles of other shapes. This includes a cubic particle (600 outermost of 1300 total atoms disordered) and rhombohedral particle (all 2000 atoms disordered) – the latter being a natural shape for the Fu-Kane-Mele model considered. Surface states have $s_{\mathrm{D}} = 0$ (for clean particles centered at the origin). As seen from Fig. 3.9(a,b) the states become localized around $V_{\mathrm{D}} = E_{\mathrm{G}}$ as before (s_{D} here plateaus at $V_{\mathrm{D}} = 1.5E_{\mathrm{G}}$). All the cases considered show that the surface states in TI nanoparticles become localized at the same disorder strength as on a planar TI surface suggesting both have the same degree of protection against disorder.

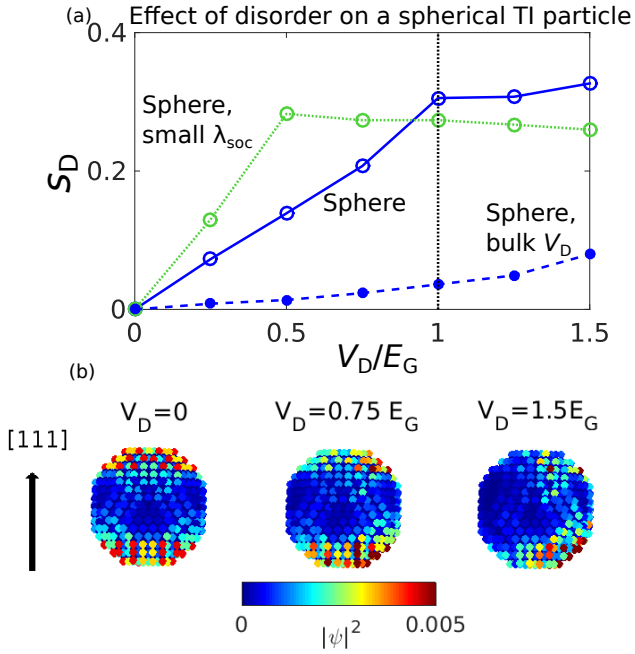

Figure 3.8: (a) Disorder function, $s_{\mathrm{D}} = [0 : 1]$ measures inversion symmetry breaking for a surface state. For the spherical particle (solid line) it saturates close to $V_{\mathrm{D}} = E_{\mathrm{G}}$ marking localization. Disorder of the same strength on all bulk atoms ($r < R_{\mathrm{D}}$ in Fig. 3.7(b)) has little effect on the surface states (dashed line). States of the spherical particle with smaller spin-orbit coupling (dotted line), $\lambda_{\mathrm{SOC}} = 1/2$ vs $\lambda_{\mathrm{SOC}} = 0$ are less robust against disorder. Error bars are smaller than the marker sizes; each data point is an average over 25 disorder realizations. (b) Wavefunction of the first state above $E = 0$ for a disorder realization of given strength, V_{D}. Figure from [2], 2017, American Physical Society.

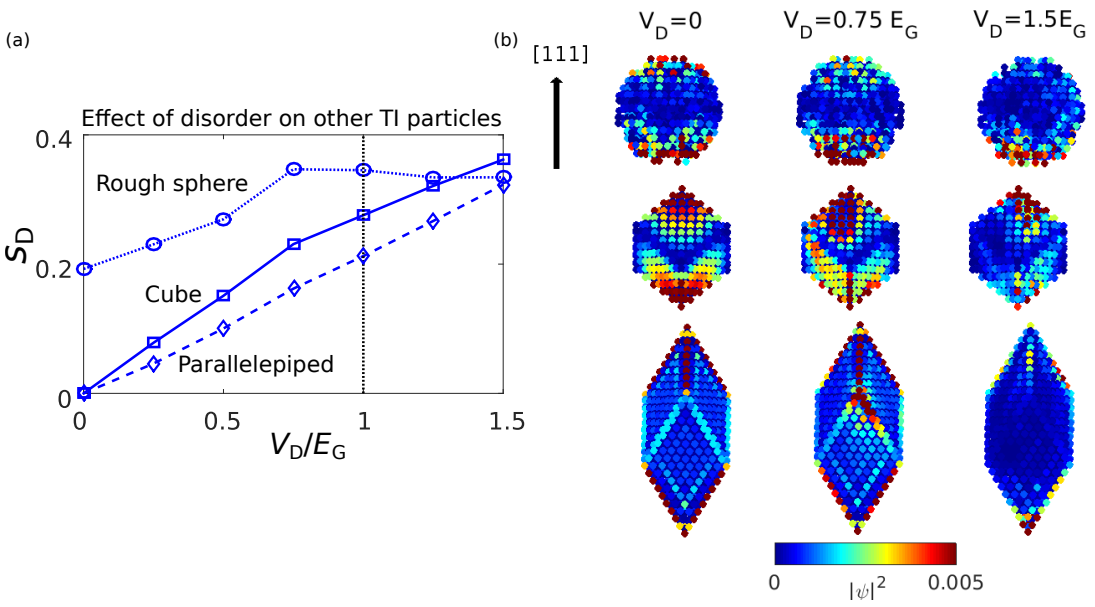

Figure 3.9: (a) The disorder function, s_D, saturates faster for a sphere with surface roughness (dotted line) and slower for the cubic (solid line) and rhombohedral particles (dashed line) compared to the sphere in Fig. 3.8(a). Error bars are smaller than the marker sizes; each data point is an average over 25 disorder realizations (for the rough sphere both V_D and surface roughness vary). (b) Surface wavefunctions for the three shapes and a single disorder realization of strength V_D. Figure from [2], 2017, American Physical Society.

3.3 Conclusion

In this chapter we have first shown analytically that the surface states in TI nanowires and nanoparticles are protected from elastic backscattering in the same way as their continuous counterparts on a planar surface. We have then applied the Fu-Kane-Mele tight binding model to TI nanoparticles and found it to agree well with analytical results for Bi_2Se_3 spheres (exponential localization at the surface, λ_{SOC}/R energy dependence of the states). Our main finding is that the discrete states in the topological nanoparticles become localized when the strength of disorder potentials, $V_D \approx E_G$, the band gap of the parent bulk crystal. Disorder of the same strength was previously found to localize the continuous states on planar surfaces of TIs [69–71]. This implies that continuous and discrete states have the same level of robustness against disorder. More broadly, the planar surfaces of bulk crystals and the smallest nanoparticles studied here lie at the opposite ends of possible length scales. Thus the protection in nanoparticles shown complements past studies suggesting that TI particles of intermediate sizes also possess protected surface states.

Chapter 4

Optical properties of topological insulator nanoparticles

Introduction

Surface states of topological insulators give rise to many interesting optical phenomena. As such illuminating the surface of a TI with circularly polarised light pulse was found to produce a surface photocurrent due to the helical nature of the Dirac surface states [24]. An additional consequence of helicity is the transient magnetisation occuring when Dirac electrons are excited by circularly polarised light pulses [25]. Yet another study found that THz light can be used to produce direct current in TIs [26]. In addition, when the time reversal symmetry is broken on the surface of a TI but not in the bulk, the material can mix electric and magnetic fields [8]. The so-called topological magnetoelectric effect manifests through a change in polarisation plane of linearly polarised light on reflection. This change termed "Kerr rotation" was observed in TI thing films where it now holds a record among all known materials [27]. In addition, the surface states have been proposed to facilitate chemical catalysis [84, 85]. One might expect the described effects due to surface states to be enhanced in TI nanoparticles due to their large surface-to-volume ratios. This is somewhat analogous to the case of metallic nanoparticles which have drastically different optical response compared to the bulk parent materials. In the case of metals the effect can be described classically in terms of free carriers present in the bulk – at least for sizes larger than ≈ 10 nm [86]. In fact, the same can occur in Bi_2Se_3 samples which often have free charge carriers arising from the bulk defects which manifested themselves, e.g

in optical experiments on microribbons [28] and large nanoplates [29]. However, such effects are not related to the surface states – for these one study predicted a divergent absorption cross section of topological insulator thin films [31]. This study applies the Fermi Golden rule to TI surface states and is similar in spirit to what we do in the present chapter for TI nanoparticles. The main difference is that in [31] optical phonons of the material are not taken into account and they turn out to play a large role. In addition, it relies on the Peierls substitution to incorporate light into the model which casts doubt on the results as will be explained below when we describe our treatment of light. Finally, it is worth mentioning that a second surface Dirac cone was predicted in Bi_2Se_3 to lie 1.5 eV directly above the first one using DFT calculations [16]. This was confirmed experimentally using two-photon photoemission technique [32] where the electron is first excited into the unoccupied state and subsequently photoemitted. The latter discovery suggests that topological surface states may find use in manipulating light in the visible region.

In the present chapter we analytically investigate optical responses of TI nanoparticles at far-IR (aka THz) frequencies. There are not many efficient sources and receivers of radiation at these frequencies (the "THz gap" problem) [10, 11] so the revealed effects may be of technological interest. Our main finding is that in TI nanoparticles the surface states can couple with bulk optical phonons to give rise to an additional absorption peak – the surface topological particle (SToP) mode [80]. To illustrate this we consider a cylindrical nanowire and a spherical nanoparticle of Bi_2Se_3.

Because the TI surface states are conducting, crudely speaking, they can be seen as a metallic layer on the surface of a TI nanoparticle. Thus one might expect optical behaviour similar to that of metallic nanoparticles in plasmonics [87, 88]. In these nanoparticles the conduction electrons of metal described by a Drude model are accelerated by the incident light forming coherent electron density oscillations known as surface plasmons. The existence of surface plasmons in metallic nanoparticles can be deduced classically by matching fields at the boundary of the nanoparticle described by a bulk dielectric function. We extend this approach to treat the TI nanoparticles by dividing the response to the external field into two parts – the bulk dielectric response and that of the surface states located at the boundary. The former is treated classically and described by the bulk dielectric function accounting for all the bulk states. The latter has to be treated quantum mechanically and is described by a $\mathbf{k} \cdot \mathbf{p}$ Hamiltonian. These two components – the bulk polarisation and the surface states – create a surface charge density which enters the boundary conditions on the electric field in a self-consistent manner as shown in Fig. 4.1. Note that without the surface states this is a textbook example of a dielectric

nanoparticle in a uniform field. However, the topologically protected surface states will modify the optical response as shown for the TI cylindrical wire and spherical particle in the next two sections. The results of this chapter have been published in [80].

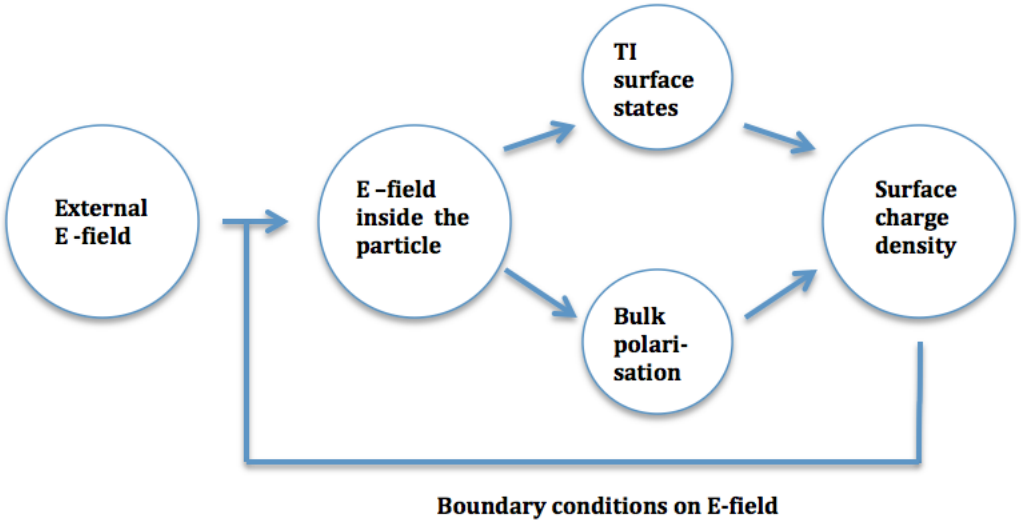

Figure 4.1: Schematics of our approach to study optical properties of topological insulator nanoparticles. External electric field polarises the body of the nanoparticle but also causes transitions between the protected surface states. These form the two contributions to the total surface charge density. The latter enters the boundary conditions for the electric field self-consistently.

4.1 Optical properties of TI nanowires

In this section we consider a cylindrical topological insulator nanowire (TINW) as a simpler case. The figure of merit for us is the absorption cross section of the TINW. It can be found in three steps:

- show how the surface states can be derived from the bulk $\mathbf{k} \cdot \mathbf{p}$ Hamiltonian using a model from the literature.
- show how the states contribute to the surface charge density using time-dependent perturbation theory.
- find how this charge density modifies the optical properties (the absorption cross section) of the TINW and compare it to the case of a trivial insulator which has no delocalised surface states.

4.1.1 The quasistatic approximation

The first step in finding the effect of the surface states on the optical properties is to decide how to treat light within the model. Here it is important to notice that there are three length scales in the system: the decay length of the surface states, the cylinder radius and the wavelength of light. The decay length is ≈ 1 nm (Appendix A.2.4). The minimal radius has to be larger than the decay length which ensures that there is enough material to support the surface states. We choose this value to be 5 nm as motivated by experiments [35] and theoretical calculations (Appendix A.2.4). The maximum radius considered is 100 nm – much smaller than the wavelength of light in the THz region ($> 10\,\mu$m) so we can work within the dipole approximation.

There are two ways to include the dipolar field in the Hamiltonian for the surface states. One is the minimal coupling procedure:

$$\mathbf{k} \to \mathbf{k} - \frac{q}{\hbar}\mathbf{A}(t) \tag{4.1}$$

The alternative is to add a real space potential to the Hamiltonian. This potential represents the electric field of light (magnetic field being negligible)

$$V = q\mathbf{E}(t) \cdot \mathbf{r} \tag{4.2}$$

The former approximation can be derived from the latter using a gauge transformation [89]. The crucial step often omitted in the literature (e.g. [31, 33]) is that when the gauge transformation is performed it applies not only to the potentials but also to the wavefunctions. Performing this time-dependent gauge transformation on the wave function is far from simple and for this reason we choose to proceed with the real space version of the dipolar approximation. Furthermore, this approach agrees better with numerical simulations [90] and experimental results [91] than the minimal coupling procedure.

4.1.2 Absorption cross section of a TI nanowire

To see how the surface states are modified due to the interaction with light we use time-dependent perturbation theory. For simplicity, let us first consider a transition from a single occupied initial state $|i\rangle = |skm\rangle$ (see Eq. 3.15) to an empty final state $|f\rangle = |s'k'm'\rangle$ caused by circularly polarised light in the xy plane. Then for an electron inside the wire having potential energy $qV_{in} \equiv \mathrm{Re}[qB_1 r e^{i(\phi - wt)}]$

where B_1 is a constant describing the strength of a uniform electric field (see below), the matrix elements are (see Eq. 3.15)

$$\langle f|\, e^{i\phi}\, |i\rangle = \chi^{\dagger}_{s'k'm'}\chi_{skm}\delta_{k,k'}\delta_{m+1,m'} \tag{4.3}$$

where the Kronecker deltas account for the conservation of linear and angular momenta. These selection rules force $k' = k$ and $m' = m + 1$. The expansion coefficients for the surface states ($r \approx R$) are to first order 2.1.5

$$c^{(1)}_{if}(t) = \frac{-i}{\hbar}\int^{t} dt'\, \langle f|\, \frac{qB_{\text{in}}R}{2} e^{i(\phi - wt)}\, |i\rangle\, e^{i(w_f - w_i)t}$$

$$= -\frac{qB_{\text{in}}R}{2}\frac{\chi^{\dagger}_{s'km+1}\chi_{skm}}{E_{s'km+1} - E_{skm} - \hbar w} e^{i(w_{s'km+1} - w_{skm} - w)t} \tag{4.4}$$

with R being the radius of the wire. In case of resonance this yields the Fermi golden rule. Away from the resonance the mixing of states creates a charge density on the initially neutral surface. In case of linearly polarized light there will be another term due to the opposite circular polarization $\propto e^{-i(\phi - wt)}$. Taking it into account the total surface charge density is then (2.16)

$$-\frac{2q}{2\pi RL}\text{Re}\left[\frac{qB_{\text{in}}R}{2}\frac{|\chi^{\dagger}_{s'km+1}\chi_{skm}|^2}{E_{s'km+1} - E_{skm} - \hbar w} e^{-i(\phi - wt)} + (m - 1 \text{ term})\right] \equiv -\delta_{smk}\epsilon_0 \text{Re}[B_{\text{in}} e^{i(\phi - wt)}] \tag{4.5}$$

where δ_{smk} (not to be confused with Kronecker delta) is the proportionality constant between the potential inside the cylinder and surface charge density coming from this particular initial state $|i\rangle = |skm\rangle$ and is given by

$$\delta_{smk} = \frac{q^2}{2\pi L\epsilon_0}\frac{|\chi^{\dagger}_{s'km+1}\chi_{skm}|^2}{E_{s'km+1} - E_{skm} - \hbar w} + (m - 1 \text{ term}) \tag{4.6}$$

Summing over all states in the band with quantum numbers s, m in the limit of an infinitely long cylinder we have

$$\delta_{sm} = \sum_k \delta_{smk} = \sum_k \frac{L}{2\pi}\delta_{smk}\Delta k \xrightarrow{L\to\infty} \frac{q^2}{4\pi^2\epsilon_0}\int_{-k_f}^{k_f}\frac{|\chi^{\dagger}_{s'km+1}\chi_{skm}|^2}{E_{s'km+1} - E_{skm} - \hbar w} dk + (m - 1 \text{ term}) \tag{4.7}$$

where we took the integration range to be even (no net current in longitudinal direction). It is assumed that the sum above only includes transitions from occupied initial to unoccupied final states. Then

summing over all occupied surface bands we get the total surface term, δ_R, given by

$$\delta_R = \sum_{sm \in \text{occ.}} \delta_{sm} \tag{4.8}$$

As shown above the delocalised TI surface states induce a surface charge density (in addition to bulk polarisation). This affects the boundary conditions when matching the electric field inside and outside the nanoparticle and modifies the optical properties 2.2.5.

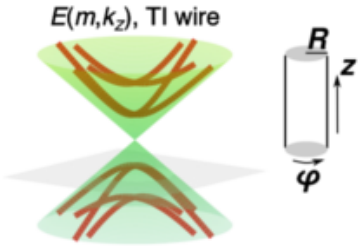

Figure 4.2: Surface bandstructure of a TI nanowire is shown. The red lines represent the surface bands. The cylinder is oriented along the z axis so each surface state is labelled by two quantum numbers – k_z (longitudinal) and m (azimuthal).

The energies of the surface states for the TINW are given by Eq. 3.14 and are illustrated in Fig. 4.2. We consider a wire extended along the z axis coinciding with the c axis of the material (Bi_2Se_3 is layered). To find the absorption cross section let us consider an incident field along the x-axis. Then we have in cylindrical coordinates

$$V_{in} = \sum_n B_n r^n \cos(n\phi) \tag{4.9}$$

$$V_{out} = -E_0 r \cos(\phi) + \sum_n \frac{C_n}{r^n} \cos(n\phi) \tag{4.10}$$

where B_n and C_n are expansion coefficients. For surface charge density given by $\sigma = -\epsilon_0 \delta_R B_1 \cos(\phi)$ we find from matching the fields $(\mathbf{E}_{||}, \mathbf{D}_\perp)$ at the boundary that the only two non-zero coefficients are

$$B_1 = \frac{-2}{\epsilon_{in} + 1 + \delta_R} E_0 \tag{4.11}$$

$$C_1 = \frac{\epsilon_{in} - 1 + \delta_R}{\epsilon_{in} + 1 + \delta_R} R^2 E_0 \tag{4.12}$$

where ϵ_{in} is the dielectric constant inside the material. To find the absorption cross-section per unit

length we use Poynting's theorem

$$P = -\langle \int_{S(V)} (\mathrm{Re}\mathbf{E} \times \mathrm{Re}\mathbf{H}) d\mathbf{S} \rangle = -\frac{1}{2} \langle \mathrm{Re} \int_V (\mathbf{H}\partial_t \mathbf{B} + \mathbf{E}\partial_t \mathbf{D} + \mathbf{H}^* \partial_t \mathbf{B} + \mathbf{E}\partial_t \mathbf{D}^*) dV \rangle \tag{4.13}$$

where $S(V)$ is the surface of the cylinder with volume V. The only term with real part that does not average to zero over time is $\mathbf{E}\partial_t \mathbf{D}^*$ (the $\mathbf{H}^*\partial_t \mathbf{B}$ term is purely imaginary) – it yields

$$\frac{dP}{dz} = \pi R^2 \frac{-2w\epsilon_0 E_0^2 \mathrm{Im}(\epsilon_{\mathrm{in}})}{|\epsilon_{\mathrm{in}} + 1 + \delta_R|^2} \tag{4.14}$$

where no k or m dependence occurs because we sum over all occupied surface bands. The normalised absorption cross-section of a cylinder is then

$$\frac{1}{2\pi R} \frac{d\sigma_{\mathrm{abs}}}{dz} = -\frac{1}{2\pi R} \frac{2}{\epsilon_0 c E_0^2} \frac{dP}{dz} = 2kR \frac{\mathrm{Im}[\epsilon_{\mathrm{in}}]}{|\epsilon_{\mathrm{in}} + 1 + \delta_R|^2} \tag{4.15}$$

where k is the wavevector of incident light and ϵ_{in} is the bulk dielectric function of the constituent material. The same result can be obtained by considering two infinite parallel lines with charge per unit length $\pm\lambda$ located at $x = \pm\Delta/2$. Their quasistatic potential is given by

$$V_{\mathrm{ext}}^{\mathrm{ind}} = \frac{-\lambda}{2\pi\epsilon_0} \ln(\sqrt{(x - \Delta/2)^2 + y^2}) + \frac{\lambda}{2\pi\epsilon_0} \ln(\sqrt{(x + \Delta/2)^2 + y^2}) \xrightarrow{r \gg \Delta} \frac{\lambda\Delta}{2\pi\epsilon_0} \frac{\cos\phi}{r} \tag{4.16}$$

Comparing this with Eq. (4.12) shows that a dielectric cylinder in uniform field can be treated as a line of dipoles with density

$$\frac{dp}{dz} = \lambda\Delta = 2\pi\epsilon_0 \frac{\epsilon_{\mathrm{in}} - 1 + \delta_R}{\epsilon_{\mathrm{in}} + 1 + \delta_R} E_0 R^2 = \frac{d\alpha}{dz} \epsilon_0 E_0 \tag{4.17}$$

where α is the polarizability defined by the above relation. This can be used in conjunction with the formula for the power radiated by a single dipole to arrive at the same result as above

$$\frac{1}{2\pi R} \frac{d\sigma_{\mathrm{abs}}}{dz} = \frac{1}{2\pi R} k \mathrm{Im}\left[\frac{d\alpha}{dz}\right] = 2kR \frac{\mathrm{Im}[\epsilon_{\mathrm{in}}]}{|\epsilon_{\mathrm{in}} + 1 + \delta_R|^2} \tag{4.18}$$

To summarize, Eq. 4.15 contains the δ_R term because the charge density of the surface states enters the boundary conditions for the normal component of the electric displacement field. Note that without the effect of surface states ($\delta_R = 0$) this is just the absorption cross section of a dielectric wire in uniform quasistatic field.

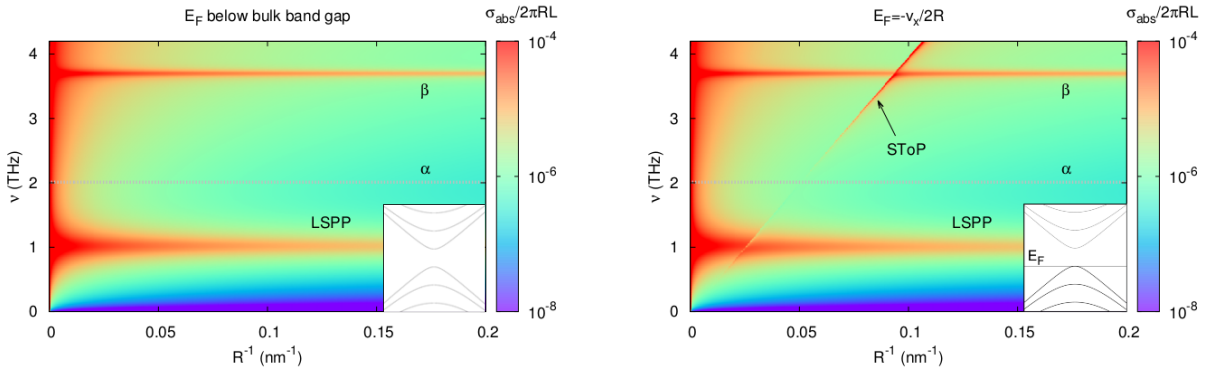

Figure 4.3: Left: Absorption cross-section of a topological insulator nanowire without occupied surface states. Two absorption lines due to bulk charge carriers (LSPP) and bulk β phonon are seen whereas the bulk α phonon does not absorb in this geometry. Right: The same with occupied surface bands shown in bold. The surface states mediate the interaction between light and the bulk α phonon of the material giving rise to the SToP mode.

The absorption cross section is insensitive to whether the light is linearly or circularly polarised (Appendix A.2.1). An example of the resultant absorption cross section without the effect of surface states ($\delta_R = 0$) is given in Fig. 4.3. Without the effect of the surface states it is dictated by the bulk dielectric function of Bi_2Se_3. This material has a layered structure and throughout this work we take the electric field of incident light to lie in the plane of the layers. In this case the dielectric function contains three terms

$$\epsilon_{\text{in}}(w) = \sum_{j=\alpha,\beta,\text{f}} \frac{w_{\text{p}j}^2}{w_{0j}^2 - w^2 - i\gamma_j w} \tag{4.19}$$

where the two Lorentz terms are due to α and β transverse phonons and the Drude term ($w_{0\text{f}} = 0$) is due to free charge carriers (labelled f) arising from the bulk defects. The parameters for the three terms in (4.19) are taken from a fit to experimental data on bulk Bi_2Se_3 [1] and presented in Table 4.1.

	$w_{\text{p}j}$	w_{0j}	γ_j
α	19.2	2.0	0.15
β	2.3	3.72	0.06
f	11.5	0	0.24

Table 4.1: Parameters for the bulk dielectric function of Bi_2Se_3. The values given are in THz and were measured at 6 K [1]. α and β phonons are represented by Lorentz terms. The Drude term is due to free bulk charge carriers (f) and not surface electrons which we treat quantum-mechanically.

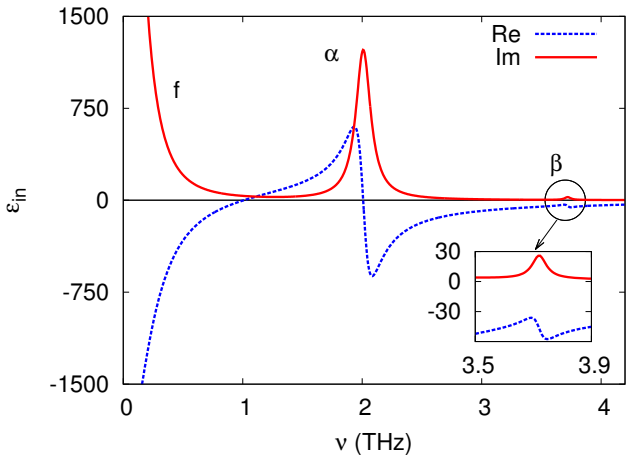

Figure 4.4: Dielectric function of bulk Bi_2Se_3 using fit to experimental data from [1].

The resultant absorption cross section in Fig. 4.3 contains two peaks at 1.05 and 3.72 THz due to bulk phonon (β) and bulk carriers (LSPP) – see Fig. 4.4. Another phonon at 2.0 THz (α) does not absorb for geometrical reasons. Apart from bulk carriers this is a typical absorption cross section of a dielectric in the THz range. The values are dictated by the optical phonons present and are similar to those in other materials. These values are several orders of magnitude lower than observed for metallic nanorods in the visible range because the wavelength entering Eq. 4.15 is much smaller in the latter case.

Turning on the δ_R term due to the surface states in Fig. 4.3 reveals the presence of the α phonon. As will be shown below the surface states mediate interaction between the phonon and light giving rise to a previously unreported collective mode. This mode manifests as an additional absorption line labelled SToP - for Surface Topological Particle mode. The line follows $\nu = v_\phi$ because the transition occurs mostly between the maximum of the highest occupied band ($-v_\phi/2 = -v_x/2R$ – see Eq. 3.14) and the minimum of the lowest unoccupied band ($v_\phi/2$). Note that we only plot absorption by the body of the cylinder whereas the transition occurs at the surface.

The SToP mode is sensitive to which surface bands are occupied. This is illustrated in Fig. 4.5 below. Here the transitions between the minima of the highest occupied and the lowest unoccupied band result in a SToP which is difficult to distinguish. More apparent is the zero absorption line associated with the transition. This occurs when all the states have transition energies above or below the light frequency and contribute in phase as given by Eq. 4.4. In most other cases there are states with transition energies either larger or smaller than the frequency of incident light. These two groups oscillate out-of-phase nullifying the overall effect. The V-shaped absorption line that occurs due to

the highest occupied states. This line is very sensitive to the Fermi energy - see Appendix A.2.2 for further examples. To conclude, in this section we have we have used the model to show how the surface states the modify absorption properties of the cylinder's body compared to the case of topologically trivial insulators. This theme is further developed in the next section where we consider a spherical nanoparticle.

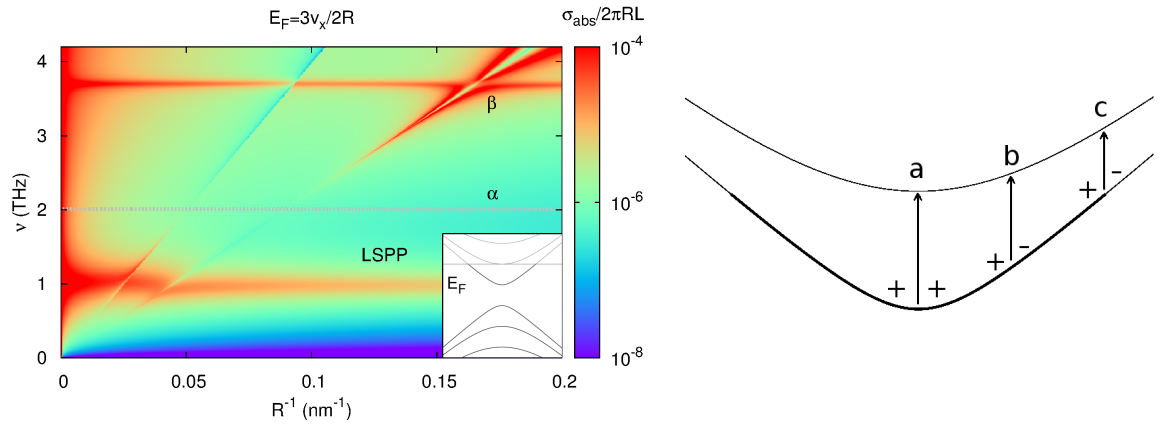

Figure 4.5: Left: Absorption cross-section of a topological insulator nanowire with a surface band above the Dirac point partially occupied. Right: Explanation of the surface states effect: letters denote light of three different frequencies and signs denote relative phases of transitions. At most frequencies there are states with transition energies above and below the frequency of light (b) which are out of phase and cancel out. One exception occurs when the light frequency matches the energy difference between the minima of the highest occupied band and lowest unoccupied band (a). This yields the zero absorption line on the left. The second exception is when the light frequency matches the transition energy of the highest occupied state - there are no occupied states with lower transition energies to cancel its effect (c). This results in the V-shaped absorption line.

4.2 Optical properties of TI nanoparticles

4.2.1 Absorption cross section of the spherical particle

We have seen previously (Eq. 3.33) that the spectrum of the spherical TI nanoparticle consists of equally spaced states – as illustrated in Fig. 4.6. In this section we describe how the surface states modify optical properties of a topological insulator nanoparticle (TINP). The effect is markedly stronger than in the case of nanowire. In, particular, the SToP mode is more pronounced and the accompanying zero absorption line is apparent. We also discuss how these effects transfer to other geometries and topological insulator materials.

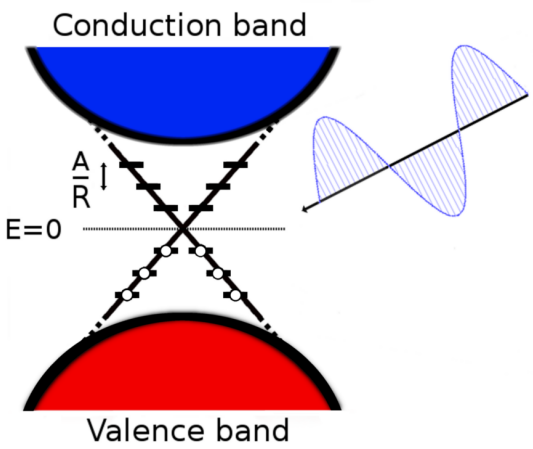

Figure 4.6: In the topological insulator nanoparticle the surface Dirac cone consists of discrete levels [4]. The Dirac point is located at $E = 0$ and the surface states have constant energy spacing A/R where $A = 3.0\,\mathrm{eV}\cdot\text{Å}$. A single electron in a surface state couples to the other states under the influence of light. This produces a time-dependent surface charge density which modifies the optical properties.

The effect of a time-dependent electric field on the electrons in surface states is again analysed using time-dependent perturbation theory. Because the states decay quickly away from the surface we can set the radius variable, $r = R$, the particle radius, everywhere. For simplicity let us for a moment consider a single surface state subject to circularly polarised light. Then the quasistatic potential of incident light gives rise to a potential energy of the electron with charge q in the surface state given by

$$q\Phi_{\mathrm{in}}|_R = q\mathrm{Re}[B_{\mathrm{in}}R\sin\theta e^{i(\phi-wt)}] \tag{4.20}$$

The light wave is travelling along the z axis ($\mathbf{k}||z$) which coincides with the $\mathbf{c}$ axis of the material – see Fig. 4.7. This beam configuration was chosen because the azimuthal symmetry of the four-band Hamiltonian for the surface states allows the solution of the resultant equations analytically (the layered structure of Bi_2Se_3 crystal makes the in-plane dispersion different from that along the $\mathbf{c}$ axis). The resultant coupling between the surface states caused by external field leads to a surface charge density. To first order we have (see 2.1.5):

$$c_f^{(1)}(t) = -\frac{i}{\hbar}\int^t dt' \langle f|\,\Phi_{\mathrm{in}}\,|i\rangle\, e^{iw_{fi}t'} = -\frac{i}{\hbar}\int^t dt' \langle f|\,\frac{qB_{\mathrm{in}}R}{2}\sin\theta e^{i(\phi-wt')} + \frac{qB_{\mathrm{in}}^*R}{2}e^{-i(\phi-wt')}\,|i\rangle\, e^{iw_{fi}t'} =$$

$$= -\frac{\langle f|\,\frac{qB_{\mathrm{in}}R}{2}\sin\theta e^{i\phi}\,|i\rangle}{\hbar}\frac{e^{i(w_{fi}-w)t}}{w_{fi}-w} - \frac{\langle f|\,\frac{qB_{\mathrm{in}}^*R}{2}\sin\theta e^{-i\phi}\,|i\rangle}{\hbar}\frac{e^{i(w_{fi}+w)t}}{w_{fi}+w} \tag{4.21}$$

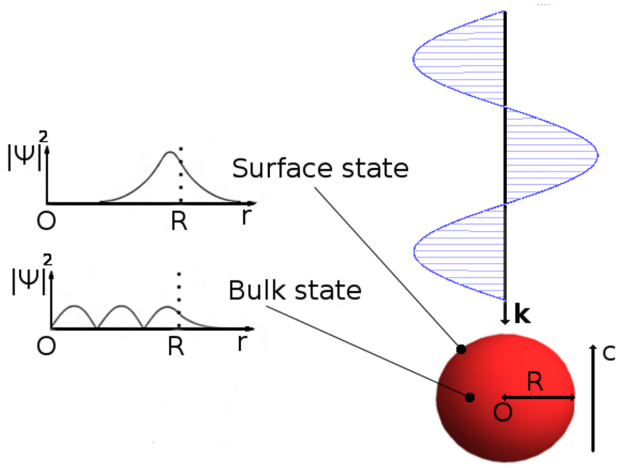

Figure 4.7: System setup: particle at the origin is subject to circularly polarised light. The **c** axis of the layered material is parallel to the wavevector of incident photon $\mathbf{k} \parallel \mathbf{c}$ (both aligned with the z coordinate).

where $\hbar w_{fi} = E_f - E_i$. The lower integration limit is omitted because we assume a pure state $|i\rangle$ in the beginning. The surface charge density arising from the state $|i\rangle$ coupled to the state $|f\rangle$ is given by

$$\sigma_{fi}(\theta, \phi, t) = c_f^{(1)}(t)\psi_i^\dagger(\theta, \phi)\psi_f(\theta, \phi)e^{-iw_{fi}t} + \text{c.c.} \tag{4.22}$$

Let us consider the state $|+, 0, 1/2\rangle$ (see Eq. 3.33 for labels) – with energy A/R (where $A = 3.0\,\text{eV}\cdot\text{Å}$) in the nanoparticle and suppose that all states below are occupied. Then, the circularly polarised light (Eq. (4.20)) has $m_z = 1$ and couples this state to the other ones:

$$\langle +, 0, 3/2| \sin\theta e^{i\phi} |+, 0, 1/2\rangle = \sqrt{\frac{2}{3}} \tag{4.23}$$

$$\langle +, 1, -1/2| \sin\theta e^{-i\phi} |+, 0, 1/2\rangle = \frac{\sqrt{2}}{3} \tag{4.24}$$

$$\langle -, 0, 1/2| \sin\theta e^{-i\phi} |+, 0, 1/2\rangle = \frac{2}{3} \tag{4.25}$$

Together with Eq. (4.22) they allow to find the time-dependent surface charge density given by

$$\sigma(\theta, \phi, t) = 2q\text{Re}\left[-\frac{qB_{\text{in}}R\sin\theta e^{i(\phi-wt)}}{8\pi R^2(E_{+0\,3/2}-E_{+0\,1/2}-\hbar w)} - \frac{qB_{\text{in}}^* R\sin\theta e^{-i(\phi-wt)}}{24\pi R^2(E_{+1\,-1/2}-E_{+0\,1/2}+\hbar w)} - \frac{qB_{\text{in}}^* R\sin\theta e^{-i(\phi-wt)}}{12\pi R^2(E_{-0\,-1/2}-E_{+0\,1/2}+\hbar w)}\right]$$

$$= -q^2\left(\frac{1}{4\pi(A-\hbar wR)} + \frac{1}{12\pi(A+\hbar wR)} + \frac{1}{6\pi(-2A+\hbar wR)}\right)\text{Re}[B_{\text{in}}\sin\theta e^{i(\phi-wt)}] \tag{4.26}$$

The divergence of the first term signifies the absorption of a photon that causes the transition $|+,0,1/2\rangle \rightarrow |+,0,3/2\rangle$. On the other hand, the resonance of the last term corresponds to the transition $|+,0,1/2\rangle \rightarrow |-,0,-1/2\rangle$ during which a photon is emitted. In fact, we should omit the last transition because we assumed that all states below are filled. Then we can write the off-resonant surface charge density in terms of the potential inside the particle as

$$\sigma(\mathbf{r},t) = \frac{-\delta_R^+ \epsilon_0 \Phi_{\text{in}}|_R}{R} = -\delta_R^+ \epsilon_0 \text{Re}[B_{\text{in}} \sin\theta e^{i(\phi - wt)}] \tag{4.27}$$

where the superscript in δ_R^+ denotes the $\text{sgn}(m_z)$ of the potential (4.20) and

$$\delta_R^+(w) = \frac{q^2}{\epsilon_0}\left(\frac{1}{4\pi(A-\hbar w R)} + \frac{1}{12\pi(A+\hbar w R)}\right) \tag{4.28}$$

The potential outside the TINP is given by

$$\Phi_{\text{out}} = \text{Re}\left[\frac{C_{\text{out}}}{r^2}\sin\theta e^{i\phi} - \mathcal{E} r \sin\theta e^{i\phi}\right] \tag{4.29}$$

where $\mathcal{E}$ is the incident field strength. Φ_{out} should now be matched to Φ_{in} using the boundary conditions on the electric field where the surface charge density σ (and δ_R^+) now enters:

$$\frac{\partial \Phi_{\text{in}}}{\partial \theta}\bigg|_R = \frac{\partial \Phi_{\text{out}}}{\partial \theta}\bigg|_R \tag{4.30}$$

$$\epsilon_{\text{in}} \frac{\partial \Phi_{\text{in}}}{\partial r}\bigg|_R = \frac{\partial \Phi_{\text{out}}}{\partial r}\bigg|_R + \sigma \tag{4.31}$$

These two equations arise from the continuity of $\mathbf{E}_{||}$ and $\mathbf{D}_{\perp}$. Solving them we obtain

$$B_{\text{in}} = \frac{-3}{\epsilon_{in} + \delta_R^+ + 2}\mathcal{E} \tag{4.32}$$

$$C_{\text{out}} = R^3 \frac{\epsilon_{\text{in}} + \delta_R^+ - 1}{\epsilon_{\text{in}} + \delta_R^+ + 2}\mathcal{E} \tag{4.33}$$

The latter relates the induced dipole moment to the external field allowing us to find the absorption cross section. Note that above we ignore the effect of the external field on the spin-orbit coupling assuming that $\mathcal{E}$ is much smaller than the fields created by atoms. The perturbation theory is itself valid for $qB_{\text{in}}R \ll \frac{A}{R}$ which translates to $\mathcal{E}$ values below $\sim 10^6$ V/m for a particle of size $R = 5$ nm (the smallest considered).

Let us now consider incident light with opposite angular momentum given by

$$\Phi_{\text{in}} = q\text{Re}[B_{\text{in}} r \sin\theta e^{i(\phi+wt)}] \tag{4.34}$$

which has $m_z = -1$. The net effect on the response of the surface state is to change the sign in front of w in the δ_R^+ term which should now be substituted in Eqs. (4.27), (4.32) and (4.33) by

$$\delta_R^- = \frac{q^2}{\epsilon_0}\left(\frac{1}{4\pi(A+\hbar wR)} + \frac{1}{12\pi(A-\hbar wR)}\right) \tag{4.35}$$

where only the middle term can be resonant. Thus a single surface state reacts differently to different circular polarisations because of intrinsic anisotropy — the states have half-integer m.

Let the Fermi energy equal A/R so that both states $|+,0,\pm 1/2\rangle$ are occupied. From calculating matrix elements it then turns out that only these two states can couple to other states under the influence of light. The effect of all the occupied states below can be neglected because they have transition energies of at least $4A/R$ (e.g. $|-,1,\pm 1/2\rangle \to |+,0,\pm 3/2\rangle$). The resultant surface charge density due to the states $|+,0,\pm 1/2\rangle$ will have the same symmetry as the incident light. In all cases ($m_z = \pm 1$, x-, y-polarised light) we have

$$\delta_R = \frac{q^2}{\epsilon_0}\left(\frac{1}{4\pi(A+\hbar wR)} + \frac{1}{12\pi(A-\hbar wR)} + \frac{1}{4\pi(A-\hbar wR)} + \frac{1}{12\pi(A+\hbar wR)}\right) \tag{4.36}$$

Another Fermi energy we consider is located at $-A/R$. In this case only the states $|-,0,\pm 1/2\rangle$ would undergo transitions (again neglecting the transitions with energy $4A/R$ and higher) in which case we have (as follows from the last term in Eq. (4.26))

$$\delta_R = \frac{q^2}{\epsilon_0}\left(\frac{1}{6\pi(2A-\hbar wR)} + \frac{1}{6\pi(2A+\hbar wR)}\right) \tag{4.37}$$

To summarise the above, an external potential applied to an initially neutral nanoparticle enters the Hamiltonian giving rise to a surface charge density. This surface charge density also enters the Hamiltonian making the problem self-consistent in nature. The initial states we chose ($|\pm,0,\pm 1/2\rangle$) are convenient because the resultant surface charge density has the same angular dependence (dipolar) as the external potential allowing us to solve the equations for the electric field analytically. In general, the surface states give rise to a surface charge density which is a linear combination of spherical harmonics that in turn creates higher harmonics in the potential. As in the case of the TI nanowire,

the incident light causes transitions between the delocalised TI surface states which lead to a time-dependent surface charge density. This charge density enters the boundary conditions on the electric field and affects the optical properties. The normalised absorption cross section of a spherical TINP is found from Eq. 4.33 to be

$$\frac{\sigma_{\text{abs}}}{4\pi R^2} = kR\,\text{Im}\left[\frac{\epsilon_{\text{in}} + \delta_R - 1}{\epsilon_{\text{in}} + \delta_R + 2}\right] \tag{4.38}$$

where the δ_R terms arise due to the surface states. We start with a simple situation where the surface states are occupied up to the Dirac point ($E = 0$) as shown in Fig. 4.6 (Left). To begin with, we only consider the two electrons in the highest occupied states at energy $-A/R$ which can be excited into the lowest vacant states at A/R. This captures the essential physics and keeps the model intuitive. As discussed above, the dipole transitions from lower occupied states require energy of at least $4A/R$ and can be neglected because they are only important for $R >$100 nm. The resultant surface charge density represented by the term δ_R given by Eq. 4.37 vanishes for bulk samples ($R \to \infty$) as expected. It is significant for nanoparticles because for small R the energy spacing of the states is comparable to the energies of the optical phonons. Note that without the δ_R term Eq. 4.38 reduces to the standard result for a dielectric particle 2.2.5. The absorption cross section of a bare nanoparticle is shown in Fig. 4.8(c). It contains two horizontal modes – LSPP and β phonon. When the surface states are occupied the absorption cross-section is modified as shown in Fig. 4.8(a). It contains two distinct features - the first one is the zero absorption line which happens at resonance as the denominator of the first term in Eq. (4.37) becomes zero – the associated surface electron absorbs a photon. The δ_R term then becomes large and real resulting in a zero absorption cross section (4.38). At this point the field inside the particle becomes vanishingly small to keep the surface charge density finite. This has a classical interpretation: the body of the nanoparticle is being screened by the perfectly conducting surface. As a result the absorption cross-section becomes zero (the scattering cross-section remains finite). The second notable feature in Fig. 4.8a is the SToP mode which arises due to the surface charge density coupling to the α phonon. The SToP mode depends on the TINP radius through Eq. (4.37). Here R^{-1} can be interpreted as a wavevector because it determines allowed angular momenta of the surface states. Physically, the SToP mode is a coherent oscillation of the charge densities due to the surface states and bulk polarisation. The mode exists because the surface states mediate the interaction of the bulk α phonon with the incident light. This is demonstrated in Fig. 4.8(b) where only the α phonon has been retained in the bulk dielectric function (Eq. 4.19) and the SToP mode is practically unaffected. Note, that above we have considered transitions between the doubly degenerate

states which we expect to be rather stable against surface passivation as described in the previous chapter.

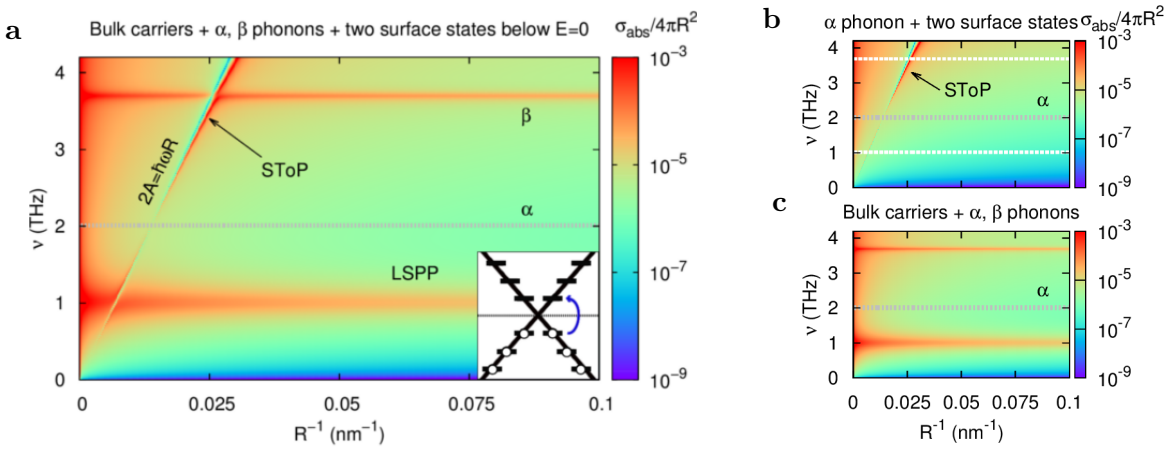

Figure 4.8: **(a)** When all the states are occupied up to the Dirac point the two uppermost electrons (at energy $-A/R$) can be promoted to empty states above the Dirac point (at A/R). The zero absorption line occurs at resonance ($2A = \hbar w R$) when the surface conductivity becomes infinite. There is also an additional absorption line (SToP, marked with an arrow) which arises because the surface electrons mediate the interaction of light with the α phonon (grey dotted line). Finally, the SToP mode crosses the radius-independent localised surface plasmon (LSPP) and bulk β phonon (the two horizontal modes). **(b)** Here the free carriers and β phonon (marked by white dashed lines) contributions to the bulk dielectric function were removed. The SToP mode is unchanged proving its origin lies in the interaction of the α phonon with the surface states. **(c)** Cross-section of the nanoparticle with no surface states occupied.

We now show that the effect of the surface states can be tuned by the Fermi energy as long as it remains in the bulk gap. For example, when the two states immediately above $E = 0$ are occupied (at A/R) the cross section become that shown in Fig. 4.9(a). The term δ_R is now different although again depends only on the two uppermost electrons (Appendix A.2.4). These electrons can be promoted to the empty states at energy $2A/R$. The transition frequency (A/R) again determines the line of zero bulk absorption. The associated SToP mode is also present and shows a strong Rabi splitting with the LSPP as shown in Fig. 4.9(b). The ratio of the Rabi frequency to that of the peak here is $\Omega_R/w > 0.1$. Finally, we note that the electromagnetic energy density inside the TINP is large at the SToP mode frequencies that occur when the real part of the denominator in Eq. (4.38) is small. Thus, both the field inside and ϵ_{in} are large resulting in large electromagnetic energy densities. This is in contrast to ordinary insulators where the field inside a material is small whenever ϵ_{in} is large and vice versa.

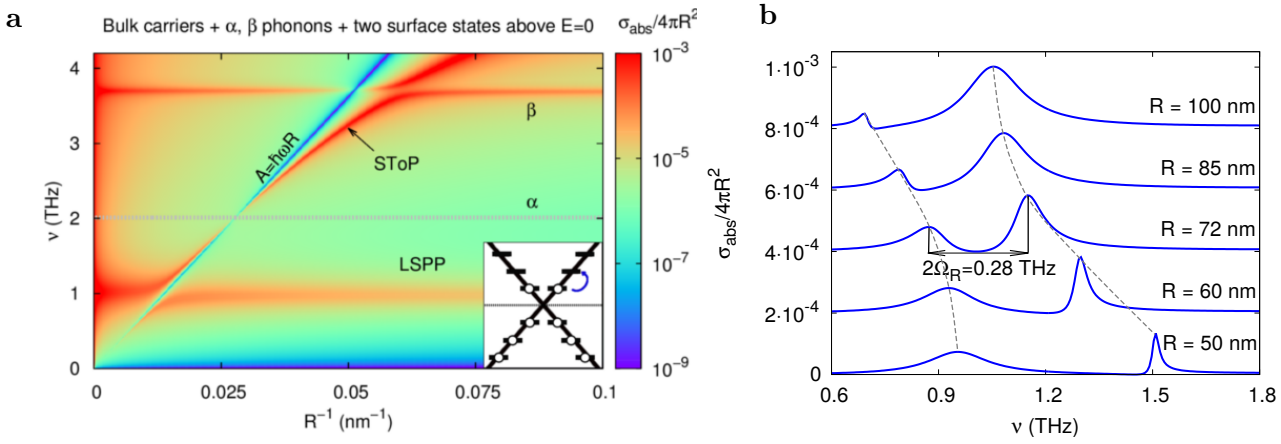

Figure 4.9: **(a)** Absorption cross section of the topological insulator nanoparticle with states immediately above the Dirac point (at energy A/R) occupied. The two uppermost electrons are perturbed by incident light which causes transitions to empty states higher in energy (at $2A/R$). This results in the line of suppressed absorption along $A = \hbar w R$ and a SToP mode (marked with an arrow). **(b)** The SToP mode couples strongly to the localised surface plasmon (LSPP). This follows from the fact that at avoided crossing ($R = 72$ nm) the splitting $\Omega_R = 0.14$ THz is a considerable fraction ($> 0.1\nu$) of the average peak frequency.

4.2.2 Absorption cross section of a spherical shell

It should be stressed that we have chosen a spherical geometry because this case can be solved analytically. The studied effect however is not restricted to TI sphere and will hold in other geometries. This is analogous to the surface plasmon resonance which occurs in metal nanoparticles of spherical and many other shapes [87, 88]. As an example of how the surface states affect optical properties in more complex situations, let us consider a TI nanoparticle with a concentric cavity or radius R_{cav} inside. The model Hamiltonian can also be used to find the states on the inner surface. The topological insulator then takes the form of a spherical shell bounded by radii R and R_{cav}. We take the Fermi energy to be located at A/R_{cav} so that for $R \approx R_{\text{cav}}$ only the surface states $|+, 0, \pm 1/2\rangle$ on the inner and outer walls will significantly affect the absorption cross section. The fields now have to be matched in the three regions: within the cavity, inside and outside the shell. The model Hamiltonian can also be used to find the surface states on the inner surface. Their contributions are represented by $\delta_{R_{\text{cav}}}$ and δ_R (related by $R_{\text{cav}} \leftrightarrow R$). We have potentials in three regions:

$$0 < r < R_{\text{cav}}: \qquad \Phi_{\text{cav}} = \text{Re}[B_{\text{cav}} r \sin\theta e^{i\phi}] \tag{4.39}$$

$$R_{\text{cav}} < r < R: \quad \Phi_{\text{in}} = \text{Re}[(B_{\text{in}} r + \frac{C_{\text{in}}}{r^2}) \sin\theta e^{i\phi}] \tag{4.40}$$

$$R < r < \infty : \quad \Phi_{\text{out}} = \text{Re}[(-\mathcal{E}r + \frac{C_{\text{out}}}{r^2}) \sin\theta e^{i\phi}] \tag{4.41}$$

where $\mathcal{E}$ is the external field. Boundary conditions at R_{cav} and R allow to find the coefficients above.

$$B_{\text{cav}} = -\mathcal{E}\frac{9\epsilon_{\text{in}}\epsilon_{out}}{D} \tag{4.42}$$

$$B_{\text{in}} = -\mathcal{E}\frac{3(2\epsilon_{\text{in}} + \delta_{R_{\text{cav}}} + \epsilon_{cav})}{D} \tag{4.43}$$

$$C_{\text{in}} = \mathcal{E}R_{\text{cav}}^3\frac{\epsilon_{\text{in}} - \delta_{R_{\text{cav}}} - \epsilon_{cav}}{D} \tag{4.44}$$

$$C_{\text{out}} = \mathcal{E}R^3\frac{(\epsilon_{\text{in}} + \delta_R - \epsilon_{out})(2\epsilon_{\text{in}} + \delta_{R_{\text{cav}}} + \epsilon_{cav}) + \frac{R_{cav}^3}{R^3}(\epsilon_{\text{in}} - \delta_{R_{\text{cav}}} - \epsilon_{cav})(-2\epsilon_{\text{in}} + \delta_R - \epsilon_{out})}{D} \tag{4.45}$$

$$D = (\epsilon_{\text{in}} + \delta_R + 2\epsilon_{out})(2\epsilon_{\text{in}} + \delta_{R_{\text{cav}}} + \epsilon_{cav}) + \frac{R_{\text{cav}}^3}{R^3}(\epsilon_{\text{in}} - \delta_{R_{\text{cav}}} - \epsilon_{cav})(-2\epsilon_{\text{in}} + \delta_R + 2\epsilon_{out}) \tag{4.46}$$

and $\delta_{R_{\text{cav}}}, \delta_R$ represent surface charge densities on the inner and outer surfaces. The absorption cross-section can again be found from C_{out}. The resultant absorption cross section shown in Fig. 4.10 differs little from that of a nanoparticle except that there is now an additional SToP mode due to the surface states located on the inner wall (occur at higher w). The SToP modes start interacting and repel each other as the shell becomes thin. This is analogous to the hybridisation of surface plasmons on the inner and outer surfaces in metallic nanoshells [92]. Note that the screening effect due to the states on the inner wall is absent because they are unable to screen the body of the shell. Overall, the spectrum of the shell is more complicated but still consists of the bare nanoparticle response and SToP modes.

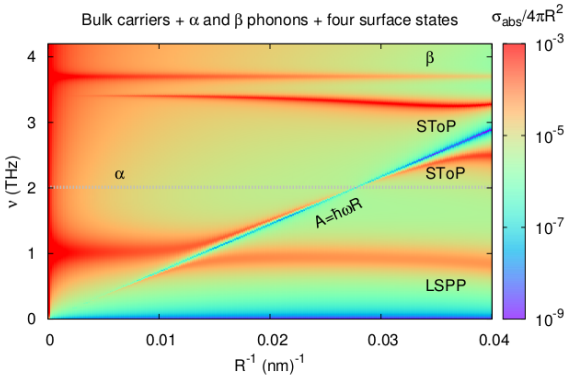

Figure 4.10: Absorption cross-section of a topological insulator shell, i.e. a spherical nanoparticle with a concentric cavity of fixed radius inside ($R_{\text{cav}} = 20$ nm). The spectrum is similar to that of a nanoparticle except for the additional SToP mode at high energy due to the occupied topological surface states on the inner wall. The screening effect due to those states is absent because they cannot screen the body of the shell as effectively as the ones on the outer wall.

4.2.3 Other materials and physical interpretation

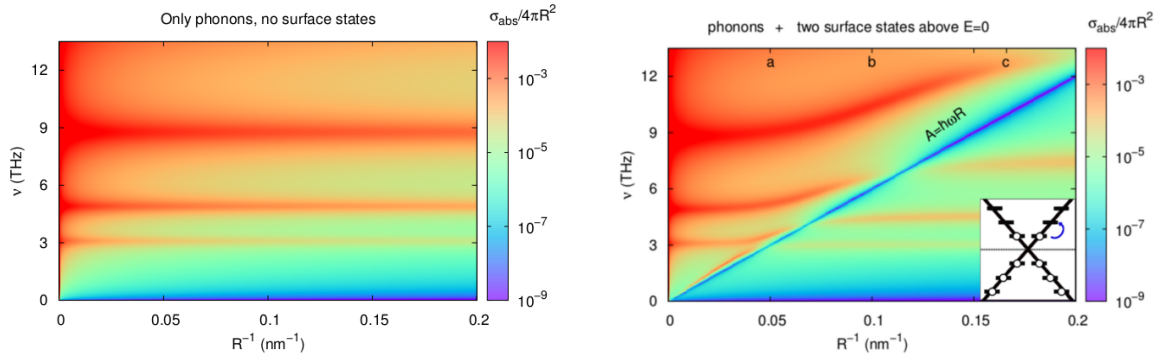

Figure 4.11: Left: Absorption cross section of a bare nanoparticle made of $BaBiO_3$. Without the effect of surface states there are four peaks due to bulk transverse optical phonons of the material. Right: Absorption cross section of the nanoparticle made of $BaBiO_3$ with two states immediately above the Dirac point occupied. The two uppermost electrons (at energy A/R) are perturbed by incident light which causes them to couple to empty states higher in energy (at $2A/R$). This leads to a line of suppressed absorption along $A = \hbar w R$ and the SToP mode accompanying it.

Although, we have considered a particular TI material the discussed phenomenon will also hold for other TI materials as shown below. Our choice of Bi_2Se_3 was motivated by abundance of experimental data and its simple surface spectrum. Most other topological insulators have a similar (0.3 eV) or smaller bulk band gaps but are more demanding to produce and have complex surface spectra. A notable exception is $BaBiO_3$ (BBO) which was predicted to have a large non-trivial gap of 0.7 eV using DFT [15]. This has not yet been confirmed experimentally presumably because the band gap lies high above the Fermi level in the pure material. Potentially this can be circumvented with doping or electric gating [15] which would make BBO a very attractive candidate for applications. In addition to the large bulk gap, the advantage of BBO compared to Bi_2Se_3 is the small number of bulk defects. The optical response of bulk BBO in the THz region is dominated by four bulk transverse optical phonons [93, 94] as seen in Fig. 4.11. Note that their absorption is ten times higher than in case of Bi_2Se_3. Conveniently, the low-energy four band Hamiltonian of BBO is exactly the same as that of Bi_2Se_3 in Eq. 3.2 except for different parameters [15] and the equality $B = A$ due to the symmetry of BBO. The material is approximately cubic with the oxygen octahedra being slightly tilted which results in a monoclinic unit cell with $\beta = 90.2°$ [95].

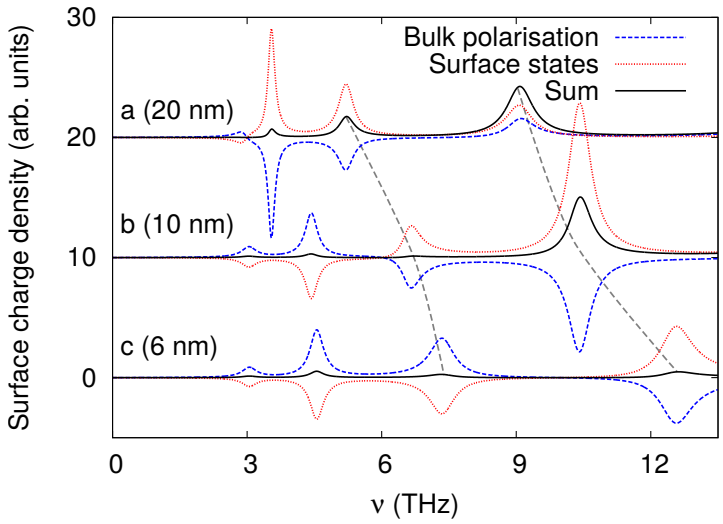

Figure 4.12: The dipoles created by surface charge densities from bulk polarisation (blue dashed line) and surface states (red dotted line) are shown for three different radii (a, b, c). These can be used to interpret the features in absorption cross section – see text for details. The grey dashed line highlights the strong Rabi splitting at small radii.

Assuming that the phonon modes and topological properties will not be significantly modified by doping, the absorption cross section of a TINP made of BBO should look like that shown in Fig. 4.11. It is clearly analogous to the case of Bi_2Se_3 in Fig. 4.9. The main differences are larger energies accessible with BBO and very strong Rabi splitting that occurs for small radii.

The absence of bulk carriers in BBO allows us to develop a simple physical picture. Its absorption cross section can be interpreted in terms of surface charge densities due to bulk polarisaion and protected surface states respectively. For an external field of strength $\mathcal{E}$ the field inside the TINP is

$$E_x = -B_{\text{in}} = \frac{3}{\epsilon_{\text{in}} + 2 + \delta_R}\mathcal{E} \tag{4.47}$$

At any given time the contribution to the total surface charge density at point $(R, 0, 0)$ (the particle is centered at the origin) due to the bulk polarisation is

$$\sigma_p = \epsilon_0(\epsilon_{\text{in}} - 1)B_{\text{in}}e^{-iwt} = -\epsilon_0(\epsilon_{\text{in}} - 1)B_{\text{in}}e^{-iwt} \tag{4.48}$$

whereas the contribution from the surface states is given by

$$\sigma_s = -\delta_R\epsilon_0 B_{\text{in}}e^{-iwt} \tag{4.49}$$

such that the sum of two terms is

$$\sigma_s + \sigma_p = 3\epsilon_0 \mathcal{E} \frac{\epsilon_{\text{in}} - 1 + \delta_R}{\epsilon_{\text{in}} + 2 + \delta_R} e^{-iwt} \tag{4.50}$$

Note that if one averages Eq. 4.50 over half a period and then takes the imaginary part, the result will be proportional to the absorption cross section given by Eq. 4.38. Physically this is because the real part of Eq. (4.48) (Eq. (4.49)) corresponds to surface charge from bulk polarisation (surface states) accounting for potential energy stored in the dipole. On the other hand, the imaginary part corresponds to the current (change in the surface charge) which gives the average power absorbed according to

$$\text{Re}[\dot{p}^* \cdot \mathcal{E}] \propto \text{Im}[p^* \cdot \mathcal{E}] \tag{4.51}$$

The average power absorbed is proportional to the real part of total surface charge density integrated over half a period (the density changes sign over the other half) from comparing two previous equations is

$$\int_{-\pi/2w}^{\pi/2w} dt \, \text{Re}[\sigma] \tag{4.52}$$

The surface charge density averaged in this way is plotted in Fig. 4.12 and clearly replicates the absorption cross section. At most frequencies the dipoles due to surface charges coming from bulk polarisation and surface states point in the opposite direction. They cross at the zero absorption frequency. In addition, the avoided crossing between the SToP mode and bulk phonons is clearly observed: above the zero absorption frequency the total dipole is dominated by the SToP mode while below – by one of the phonons. Finally, there is a strong Rabi splitting at small radii similar to that in Fig. 4.9 (Right).

An analogous simple physical interpretation can be obtained for Bi_2Se_3 once we note that its ϵ_{in} is dominated by an optical α phonon. The maximum in absorption occurs when the vanishing real part of the particle's effective dielectric function vanishes:

$$\text{Re}[\epsilon_{\text{eff}}] = \text{Re}[\epsilon_{\text{in}} + \delta_R] = \text{Re}[\frac{C}{A - \hbar w R} + \frac{w_p^2}{w_0^2 - w^2 - i\gamma w}] = 0 \tag{4.53}$$

where the two terms correspond to the surface states and the phonon of relative strengths C and w_p respectively. A determines the energy spacing of the surface states, R – the particle's radius, w_0, γ – frequency and damping of the α phonon and w is the frequency of light. The above equation can be

rewritten as:

$$C(w_0^2 - w^2)^2 + C\gamma^2 w^2 + w_p^2(A - \hbar w R)(w_0^2 - w^2) = 0 \tag{4.54}$$

In the limit $w \ll w_0$ the only root is given by

$$w = \frac{1}{\hbar R}\left(A + \frac{w_0^2 C}{w_p^2}\right) \tag{4.55}$$

Thus much below the phonon frequency, w_0, the SToP mode appears immediately above the zero absorption line, $A = \hbar w R$. These conclusions agree with the results of a full calculation of absorption cross section of the particle in Fig. 4.9(a) [80]. The SToP mode has predominantly the character of the surface states (the phonon term $\propto w_p^{-2}$ in Eq. 4.55). In the opposite limit of $w \gg w_0$ there are two roots only one of which is positive:

$$w = w_p\sqrt{\frac{A}{C}} \tag{4.56}$$

thus at high frequencies the mode is expected to become independent of radius. Clearly, high above w_0 the SToP mode has mostly the character of bulk polarization - see Eq. 4.56. The same conclusions are reached by considering surface charge density obtained from full calculation shown in Fig. 4.13. It is dominated by the surface states below w_0 and – bulk polarization above it. Note that the charges from the surface states and bulk phonons have opposite signs. This feature is responsible for the weak field enhancements in this system (< 10) compared with metallic nanoparticles in plasmonics.

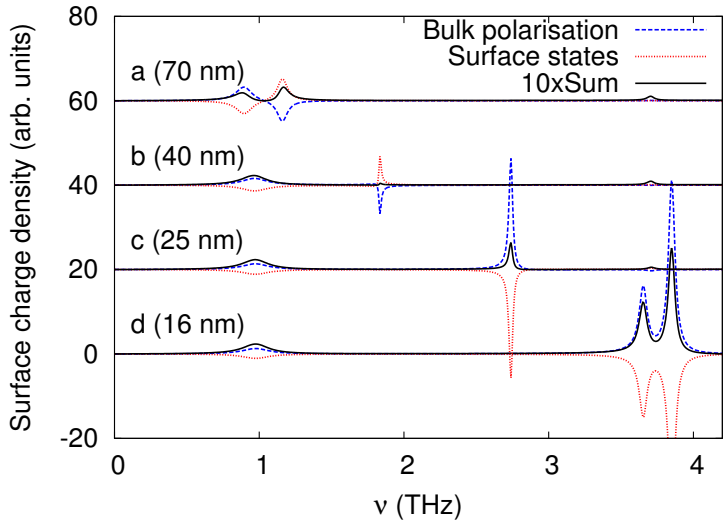

Figure 4.13: The dominant contribution depends on whether the frequency $\nu > \nu_\alpha$, frequency of the α phonon in the material.

4.3 Conclusion

To conclude, in this chapter we have combined approaches from electromagnetism (particle in uniform quasistatic field) and quantum mechanics (time-dependent perturbation theory) to study the optical properties of the TI nanowire and nanoparticle. We have found, that for radii below ≈ 100 nm the spacing of the surface states becomes comparable to that of bulk optical phonons in the material. These lead to two features absent for ordinary insulators. One is a dent in absorption. This occurs when light matches the resonant frequency between two surface states. As a result all incident light is absorbed on the surface and none of it reaches inside the wire (or particle). The second feature is an additional absorption peak that occurs due to the interaction between phonons, surface states and light. Both described effects can be tuned with the Fermi energy and particle' shape. Moreover, in the previous chapter we have shown that the discretized states considered in nanoparticles are also protected from a certain degree of disorder. This suggests that the described effects may be observed in practice although likely at low temperatures as they rely on coherency of the interaction.

Chapter 5

Photonic topological insulators

Introduction

Photonic crystals are structures with periodic variations of dielectric constant, ϵ – see Fig. 5.1. In the 1980s it was realized [96,97] that such periodicity allows us to apply the Bloch's theorem and construct a band structure for photons 2.2.2. These photonic band structures are in many ways analogous to those known for electrons in condensed matter physics. Namely, allowed light states inside photonic crystals are characterized by bands in $(\mathbf{k}, w)$ space. Propagation of energy and information is dictated by $\nabla_{\mathbf{k}} w$ and frequencies at which no allowed states exist and the crystal behaves like a mirror are called "photonic band gaps". Overall, the photonic crystals have greatly increased our ability to manipulate light leading to, e.g. optical fibers and mirrors based on the photonic band gaps.

Shortly after the discovery of electronic TIs Haldane realized that because the effect is based on the single-particle band structures it can be extended to photonics [66]. Since then studies of topological phenomena have also been extended to acoustics [98–100], optical lattices [101] and plasmonics [102–105]. Our concern in this chapter however will be with photonic analogues of TIs [43]. These devices are currently of much interest because their topologically protected boundary states can be used to realize unidirectional propagation of light which depends on the polarization (spin). Unidirectional propagation allows us to minimize scattering losses and can be useful for realizing optical networks [52]. Such propagation has already been demonstrated for a number of photonic TIs [44–50].

From the modelling point of view photonic TIs are simpler than electronic ones because for the intensities considered the interaction between photons (through non-linearity of the medium) is insignificant.

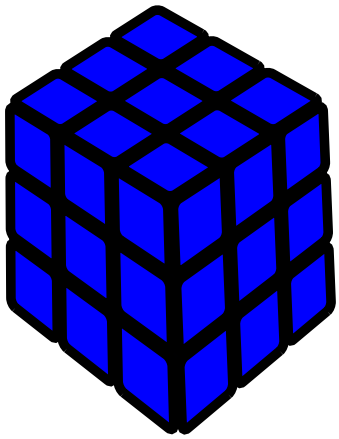

Figure 5.1: Photonic crystals are artificial materials where the dielectric constant, ϵ varies periodically in space. This variation acts as a periodic potential for photons and allows us to apply Bloch's theorem. The resultant single-particle photonic band structures can be classified according to their topology.

From the topological point of view the main difference is that photons are bosons and the time-reversal operator satisfies $\Theta^2 = 1$ (see 2.4.4) as opposed to $\Theta^2 = -1$ for fermions [43]. This means that one cannot have a topological phase with photons relying only on the time reversal symmetry because the Kramers doubling at the time-reversal-invariant points in the first Brillouin zone no longer occurs. As a result, researchers have come up with several other ways to achieve photonic topological phases. One of them is to break the time reversal symmetry with an applied magnetic field [46, 47] (analogues of the Quantum Hall effect). In these realizations the frequency gap depends on the strength of the magnetic field applied. Unfortunately, we cannot produce strong enough magnetic fields to provide us with topological gaps at optical frequency this way [53]. Another way to achieve Kramers doubling is by making the transverse magnetic (TM) and electric (TE) modes degenerate using materials with $\epsilon = \mu$ [67]. Both this and the magnetic field realization lack suitable materials to operate in the optical range. An alternative is to use crystal symmetry [48, 49, 51] in what can be seen as the photonic analogues of topological crystalline insulators (TCI) – see 2.4.3. They preserve the time-reversal symmetry and can be used at any frequency due to the scale invariance of Maxwell's equations (except at the atomic scale where the constitutive relations break down). However, it comes at a price of the edge states being more sensitive to structural disorder because the relevant topological invariant is now only defined if a particular crystal symmetry is present. Nevertheless, these edge states allow novel ways to use the polarization of light (analogue of spin) for integrated optical circuits and quantum computing [52].

This chapter consists of three parts. Firstly, we present a particular 2D photonic TCI (uniform along z) based on the C_6 symmetry from the literature [51]. This TCI is made of a dielectric and supports

topological edge states for TM polarization. To model it we use the MPB frequency domain (see 2.2.3) plane wave code [59]. We then show how, inspired by this design, we can make another TCI that shows topological properties for TE modes. In the second part we show how the same ideas can be used to design a planar TCI using metallic rods which has been realized experimentally and shown to possess topological edge states. The last part introduces an analytical model to describe the edge states. This is based on the $\mathbf{k}\cdot\mathbf{p}$ method and applies to all three designs considered (TCI for TM, TE and fully 2D metallic) as it relies only on the crystal symmetry.

5.1 All-dielectric photonic crystalline TIs

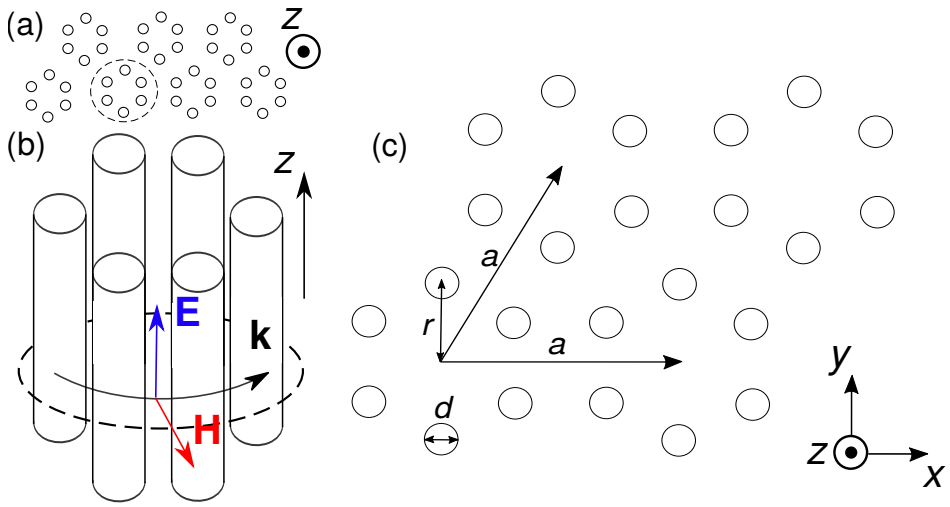

Figure 5.2: (a) Top view of the photonic TCI made with dielectric rods. (b) Six of these rods constitute a meta-atom; fields for the TM polarization are shown. (c) Lattice vector, a, and rod diameter, d, are fixed; changing r allows us to switch between the trivial and topological phases.

There are many possible designs of photonic TIs. Here our focus is on a photonic TCI crystal with C_6 symmetry made of silicon rods [51] – see Fig. 5.2(a). In the chosen crystal, six silicon rods are arranged in a hexagon to form a meta-atom such that the bulk crystal possesses both time-reversal and C_6 symmetries. Their combination allows us to achieve a TI phase [51]. Because the rods are uniform along the z axis, the supported modes separate into two groups – even (TE) and odd (TM) states depending on how the fields transform on reflection in the xy plane. When the spacing of all rods in the crystal is equal $r = a/3$ in Fig. 5.2(c) there is a bulk doubly-degenerate Dirac cone for TM polarization at the Γ point - see Fig. 5.3(b). This happens because the supercell containing six rods is no longer primitive when $r = a/3$. At this point the primitive cell contains just two rods and its top view looks exactly like the graphene lattice. As a result, the Dirac cones from the 1BZ of the

primitive cell (two rods) at the K and K' points fold onto the Γ point of the larger cell containing six rods. To push the crystal into the trivial regime we need to decrease the size (r/a) of the meta-atoms. On the other hand, increasing r/a leads to a band inversion and turns the crystal into a topological phase as shown by [51] and reproduced in Fig. 5.3(a,c).

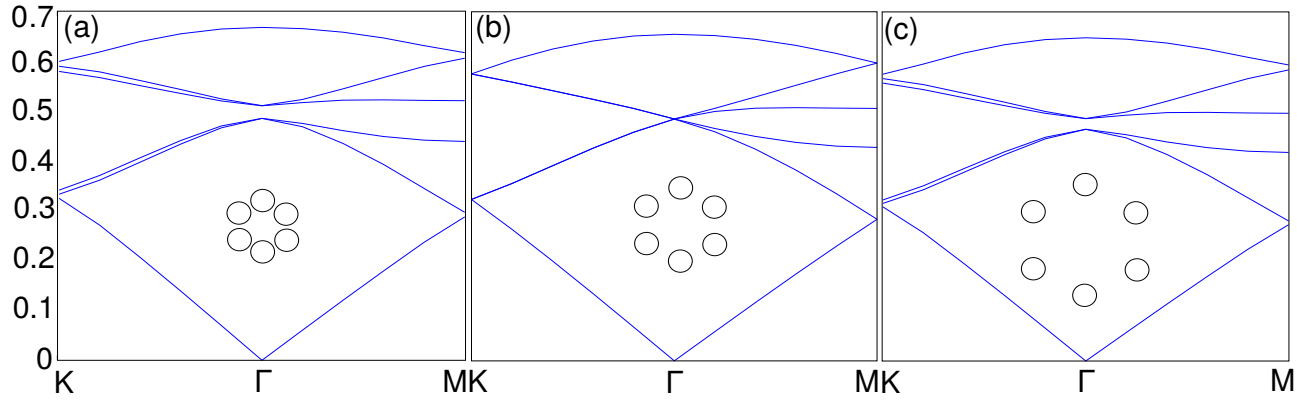

Figure 5.3: (a) The radius of the meta-atom (six dielectric rods) is $r = a/3.125$ where a – lattice constant; the crystal is in trivial regime. (b) At $r = a/3$ the photonic band gap closes and a topological transition occurs. (c) For $r = a/2.9$ the band gap re-opens with the system now in topological regime. $\Gamma = (0, 0)$, $K = (0, -2/3)2\pi/a$, $M = (1/2\sqrt{3}, -1/2)2\pi/a$.

	Linear	Quadratic	Cubic
E_1	(x, y)	(xz, yz)	irrelevant
E_2	-	$(x^2 - y^2, xy)$	$(zxy, z(x^2 - y^2))$

Table 5.1: Basis functions of the two doubly degenerate representations of the C_6 group, E_1 and E_2.

The basis functions (see 2.3.2 and 2.3.3) for the doubly-degenerate representations of the C_6 group are shown in the character table 5.1 above. In this crystal only the TM but (not TE) polarization has a full photonic band gap as seen from Fig. 5.4 and is of interest to us here. The relevant basis functions are (x, y) and $(x^2 - y^2, xy)$. For the doubly-degenerate modes at the Γ point we expect a pair reminiscent of the hydrogen p_x and p_y orbitals as well as another one which are $d_{x^2-y^2}$ and d_{xy}-like respectively [51] as seen in Fig. 5.4(a). The four bands formed from these orbitals form the bulk Dirac cones when $r = a/3$ – away from this value a band gap develops. The same authors also demonstrated that ribbons of this photonic TCI have edge states supporting unidirectional propagation [51].

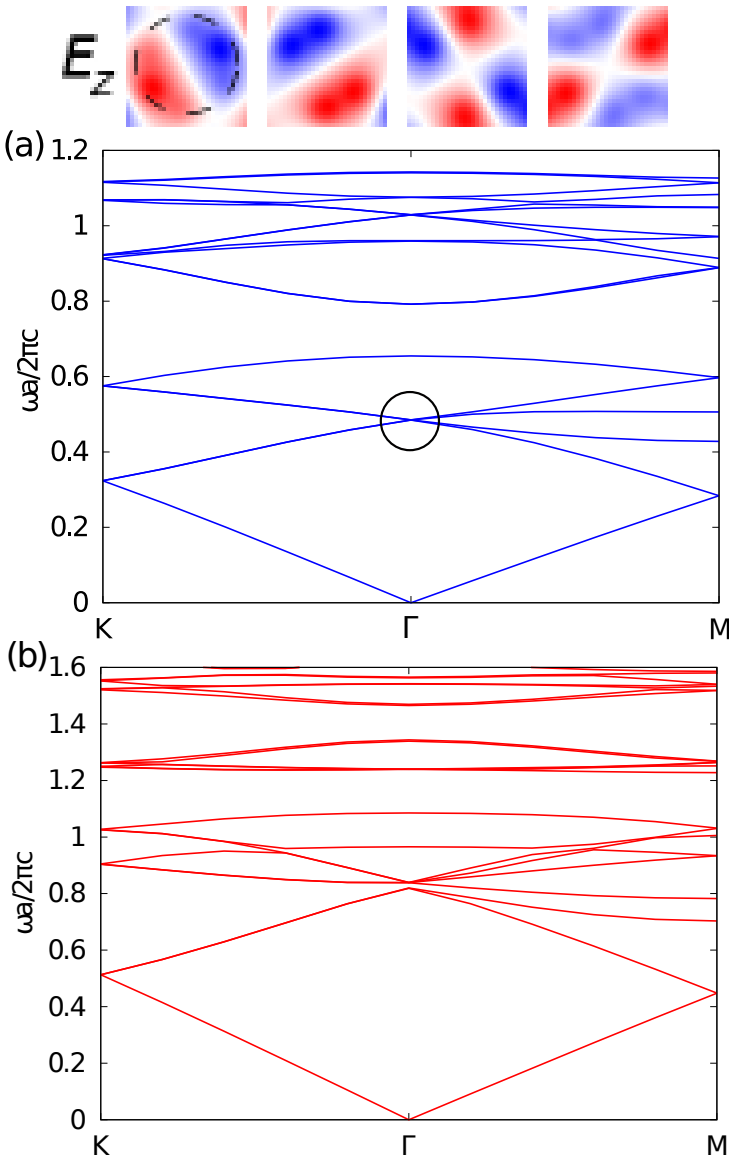

Figure 5.4: (a) Band structure of the photonic TCI made with dielectric rods ($\epsilon = 11.7$ for silicon) for the TM polarization and $r/a = 1/3$. The encircled bulk Dirac cone contains four modes whose E_z fields are shown above (dashed line represents a meta atom). For $r/a \neq 1/3$ the Dirac cone develops into a full band gap. (b) In contrast, band structure for TE polarization does not have a full band gap.

Above we have a seen a TCI design with topological edge states that have TM polarization. In practice TE polarization is often used so it would be interesting to try and design a topological crystal with a full TE band gap. We have tried a few designs and found that a triangular array of dielectric hexagons (uniform in z) as shown in Fig. 5.5 possesses a bulk Dirac cone – see Fig. 5.6(a). The crystal can be turned into a photonic TCI if we increase the air gaps between the hexagons appropriately (see Appendix A.3). The ribbon of such a TCI cladded with trivial crystals should then display topological edge states at the interface which is indeed seen in Fig. 5.6(b).

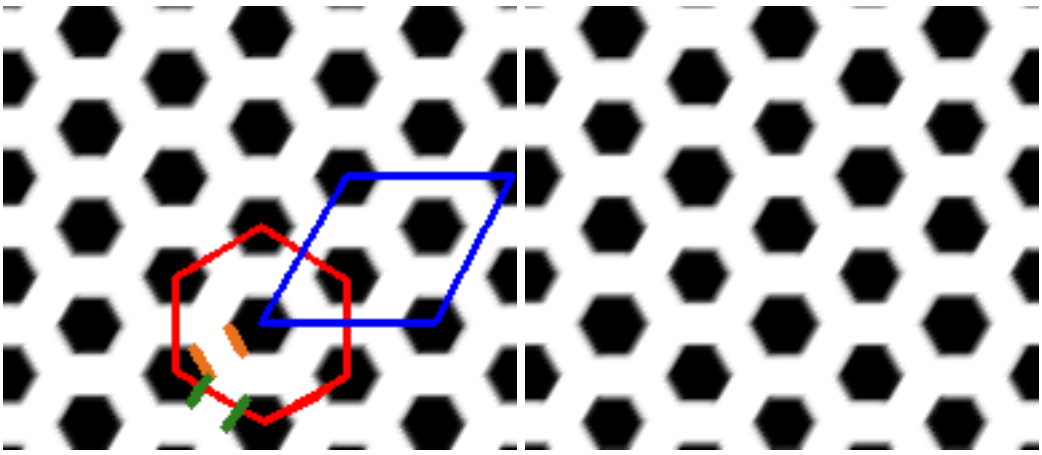

Figure 5.5: (left) This periodic structure of silicon hexagons (uniform in z) possesses a bulk Dirac crossing which turns into a topological band gap if (right) the gaps inside every other hexagon (orange) become longer than the ones connecting them (green). The red hexagon highlights the motif and the blue rhombus – the primitive unit cell.

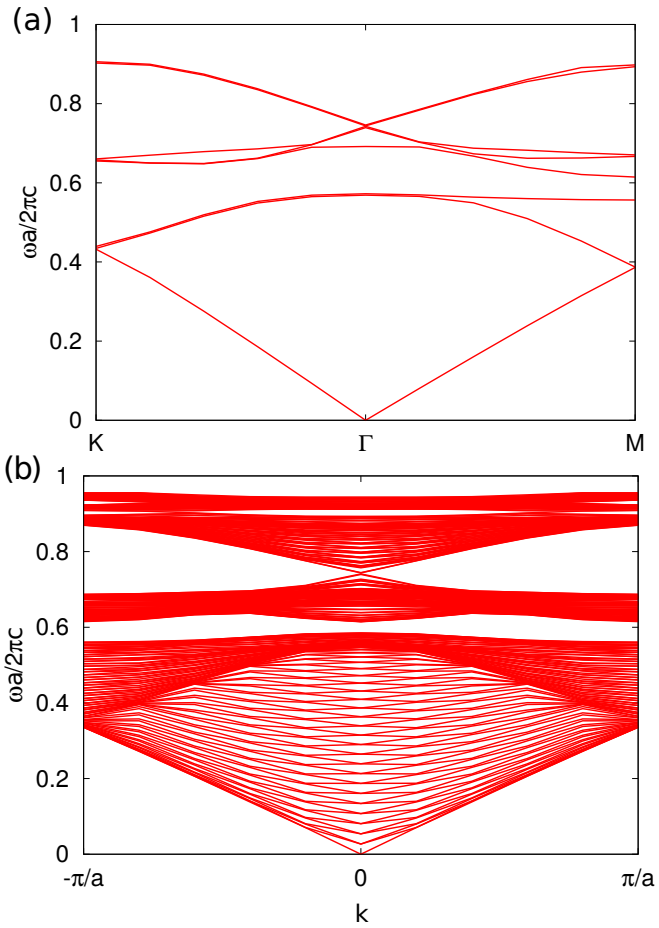

Figure 5.6: (a) Band structure of triangular array of silicon hexagons shows a bulk Dirac cone (uniform in z). (b) The hexagons can be disorted to achieve a topological ribbon surrounded by trivial crystal (20 and 5 unit cells in width). The ribbon displays TE-polarized topological edge states inside the photonic band gap.

5.2 Planar photonic crystalline TI

The previous section focused on photonic TCIs of infinite height. In practice we would like to keep our structure as thin as possible. To achieve that one might use a high-index dielectric material and this approach has already been attempted [106]. Here we take a different approach and study metasurfaces made of metal motivated by very interesting experimental results obtained by Mrs Yulia Dautova from the University of Exeter. She studied a planar structure whose top view is schematically the same as shown in Fig. 5.5 with gaps occupied by a perfect conductor forming a hexagonal 2D net. This net of wires possessing D_{6h} symmetry has been shown to support unidirectional edge states (not yet published). The advantage of this structure is that it is simple to construct (metallic wires) and is scalable to other frequencies as long as the constituent materials acts as a perfect metal. We study this structure with two methods. Firstly, we consider a thin structure (confined to the $z = 0$ plane) of finite width using the Boundary Element Method as implemented in the SCUFF-EM code [107]. The code enables us to find the least leaky modes around a certain frequency at the Γ point ($\mathbf{k} = 0$) in the 1BZ. Their charge densities are shown in Fig. 5.7(a). In particular, if we start from all metallic links being equally spaced ("Dirac") and contract the inner part of the motif, the d-like mode becomes lower in frequency than the p-like suggesting a band inversion.

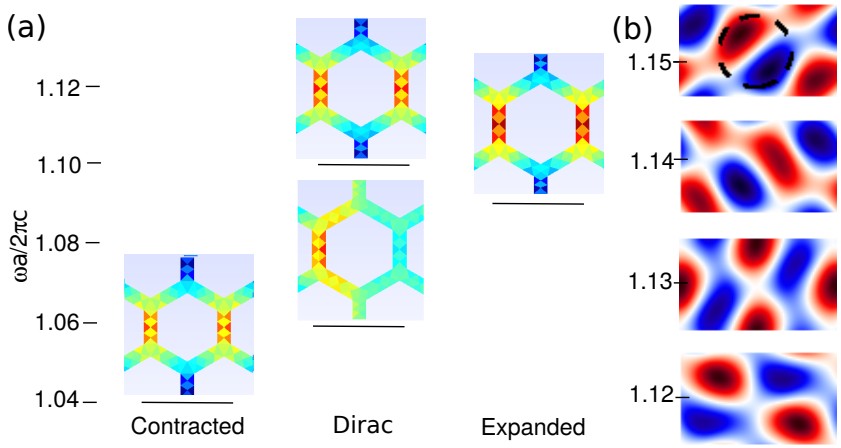

Figure 5.7: (a) Surface charge densities of the modes at the Γ-point in the 1BZ for three structures plotted. They were obtained with the Boundary Element Method and are plotted against Re[w] (y axis). The material is perfect metal of infinitesimal thickness. When the links inside the hexagon are shorter than between the neighbouring hexagons (Contracted) a band inversion occurs leading to a topological phase. (b) E_z field profiles for the four modes obtained with FDTD at the same frequency (to within five per cent). Rectangular unit cell used contains two motifs one of which is schematically shown with a dashed circle.

The above results also hold experimentally – see Fig. 5.8. Namely, in a ribbon-like arrangement when

the topological phase is surrounded by a trivial metasurface the linear dispersion is observed in the photonic band gap. Moreover, arranging the two phases in a 2×2 checkboard-like pattern allows to observe unidirectional propagation.

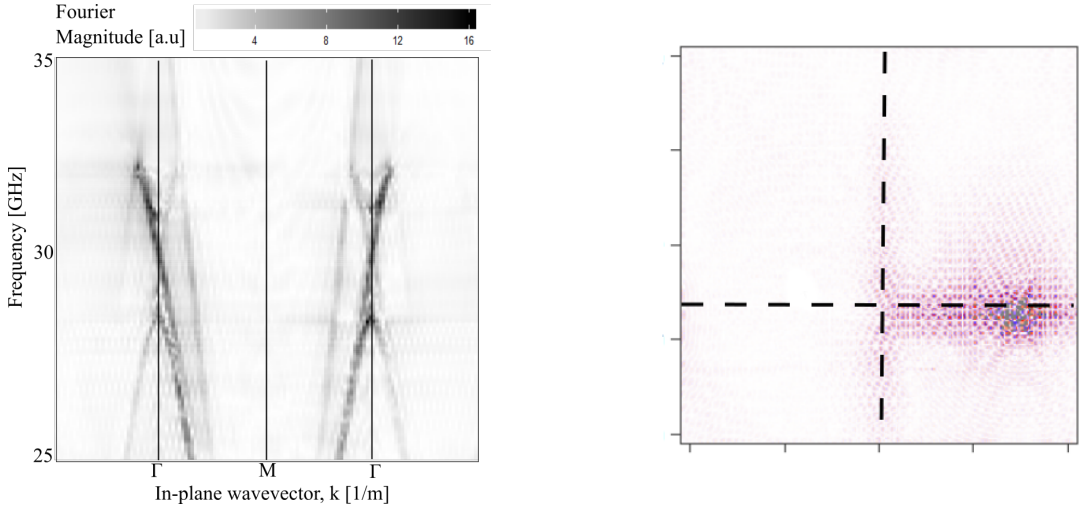

Figure 5.8: Left: The band structure of a topological ribbon made of metallic wires cladded with the trivial phase. The Dirac crossing corresponding to the topological edge modes is observed inside the photonic band gap for this metasurface. Right: The unidirectional propagation of light is observed when the tiles of topological and trivial phases are arranged in a 2x2 checkerboard pattern. The dashed lines represent the boundaries between the tiles. With the source placed in the bottom right corner light propagates vertically but not horizontally to the right after the "crossroads". The results are a courtesy of Mrs Yulia Dautova from the University of Exeter.

To understand the polarization of the modes we first note that the structure has a mirror plane in the xy plane. This implies that the modes come in two flavours with respect to the mirror operation. For a general structure with a mirror symmetry the fields satisfy:

$$\mathbf{E} = (E_x(x,y,z), E_y(x,y,z), E_z(x,y,z)) = (\pm E_x(x,y,-z), \pm E_y(x,y,-z), \mp E_z(x,y,-z)) \tag{5.1}$$

$$\mathbf{H} = (H_x(x,y,z), H_y(x,y,z), H_z(x,y,z)) = (\mp H_x(x,y,-z), \mp H_y(x,y,-z), \pm H_z(x,y,-z)) \tag{5.2}$$

where $\pm$ corresponds to the even and odd modes respectively also known as TE- and TM-like. The latter notation is motivated by the fact that at $z = 0$ the even modes have non-zero components E_x, E_y, H_z while the odd ones have H_x, H_y, E_z - just like for the TE and TM modes in the structures extended in z studied in the previous subsection. To find the symmetry of our modes we have studied the same structure using the FDTD code MEEP [108] and found four modes whose E_z fields are reminiscent of the hydrogenic $p_x, p_y, d_{xy}, d_{x^2-y^2}$ orbitals – see Fig. 5.7(b). These can again be understood from the character table of the D_{6h} group whose relevant fragment is shown in Table 5.2.

	Linear	Quadratic	Cubic
E_{1g}	-	(xz,yz)	irrelevant
E_{2g}	-	(x^2-y^2, xy)	-
E_{1u}	(x,y)	-	irrelevant
E_{2u}	-	-	$(zxy, z(x^2-y^2))$

Table 5.2: Basis functions of the doubly degenerate representations of the D_{6h} group.

To find out whether our modes are TM- or TE-like we have checked the field values above and below the $z = 0$ plane where our metallic metasurface is positioned. The representative results shown in Fig. 5.9 for one of the four modes clearly show that our modes are TM-like (odd).

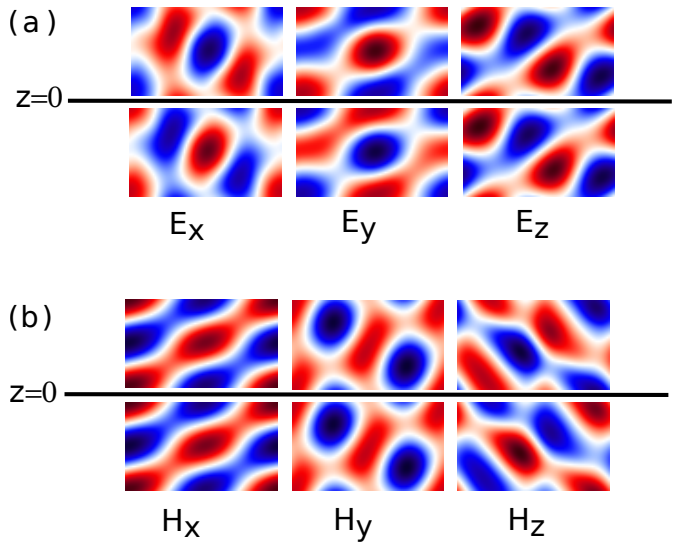

Figure 5.9: (a) E and (b) H fields for one of the four bulk modes (representative) have TM-like symmetry forming the topological band gap.

5.3 Analytical model

The $\mathbf{k}\cdot\mathbf{p}$ approximation of semiconductor physics relies on knowing the symmetries of the orbitals involved. As such, it can also be applied to photonic crystals because the symmetries of the modes there can be deduced from those of the underlying photonic crystal. In the following, we first present the $\mathbf{k}\cdot\mathbf{p}$ Hamiltonian relevant for the photonic structures discussed above. Later we use it to derive the frequencies, mode profiles and polarizations of the edge states.

The crucial idea of the $\mathbf{k}\cdot\mathbf{p}$ method is to expand a mode using other modes with $\mathbf{k} = \mathbf{0}$ and similar frequencies as basis – see 2.1.2. Firstly, consider a mode which transforms as the x basis function of the E_{1u} in Table 5.2 (its E_z field reminds the hydrogenic p_x orbital). Let us change the notation so that the $\mathbf{E}$ and $\mathbf{H}$ fields associated with this mode are collectively denoted as p_x from now on. Then

adopting the same notation for the other three relevant photonic bands we can expand the field of any mode close to the band gap as

$$[\mathbf{E}, \mathbf{H}] \approx \alpha p_x + \beta d_{x^2-y^2} + \gamma p_y + \delta d_{xy} \tag{5.3}$$

where $\alpha, \beta, \gamma, \delta$ are some coefficients. In what follows, it is more convenient to work with $p_\pm = (p_x \pm ip_y)/\sqrt{2}$ and $d_\pm = (d_{x^2-y^2} \pm id_{xy})/\sqrt{2}$. So that the field expansion becomes:

$$[\mathbf{E}, \mathbf{H}] \approx \alpha' p_+ + \beta' d_+ + \gamma' p_- + \delta' d_- \tag{5.4}$$

One can then write the $\mathbf{k} \cdot \mathbf{p}$ equation as

$$H |\psi\rangle = w' |\psi\rangle \tag{5.5}$$

where $|\psi\rangle = (\alpha', \beta', \gamma', \delta')^T$ and $w' \equiv w - w_0$. The four band $\mathbf{k} \cdot \mathbf{p}$ Hamiltonian, H, in the basis of p_+, d_+, p_-, d_- was previously found to be [51]

$$H = \begin{pmatrix} M + Bk^2 & Ak_+ & 0 & 0 \\ A^*k_- & -M - Bk^2 & 0 & 0 \\ 0 & 0 & M + Bk^2 & Ak_- \\ 0 & 0 & A^*k_+ & -M - Bk^2 \end{pmatrix} \tag{5.6}$$

where A is purely imaginary, B and M are some constants, $k^2 = k_x^2 + k_y^2$ and $k_\pm = k_x \pm ik_y$. The specific values of the constants vary with the details of the photonic TCI considered - the spacing of the rods, their diameters and the dielectric function. However, the form of the Hamiltonian relies only on the C_6 symmetry of the crystal. Because the crystal is uniform in z we can separate the in-plane motion from that associated with k_z. This Hamiltonian 5.6 was originally derived by [51] for the hexagonal array of dielectric cylinders considered at the start of the chapter. However, it relies only on the C_6 like symmetry of the structure in the xy plane and hence also applies to the the dielectric hexagons and the metallic metasurface also considered in this chapter.

To find the associated edge modes we use the $\mathbf{k} \cdot \mathbf{p}$ Hamiltonian above in conjuction with the method of Imura *et al.* [3] for electronic TI wires – see Chapter 3. We assume a photonic crystal with circular

perimeter and using

$$k_x = k_r \cos\phi - k_\phi \sin\phi \quad k_y = k_r \sin\phi + k_\phi \cos\phi \tag{5.7}$$

extract the radial part of the Hamiltonian:

$$H_\perp = \begin{pmatrix} M + Bk_r^2 & Ae^{i\phi}k_r & 0 & 0 \\ A^* e^{-i\phi}k_r & -M - Bk_r^2 & 0 & 0 \\ 0 & 0 & M + Bk_r^2 & Ae^{-i\phi}k_r \\ 0 & 0 & A^* e^{i\phi}k_r & -M - Bk_r^2 \end{pmatrix} \tag{5.8}$$

In doing so we assumed a posteriori that the states are localized at the edge and neglected the $(1/r)\partial_r$ term [3]. This is a good approximation for large particles with radius, $R \gg \kappa^{-1}$, the decay constant. Substituting the ansatz, $e^{\kappa(r-R)}$, gives $k_r \to -i\kappa$ with an expression for the frequency:

$$w'_\perp = \pm\sqrt{-|A|^2\kappa^2 + (M - B\kappa^2)^2} \tag{5.9}$$

Setting $w'_\perp = 0$ we find κ (see below) and two possible eigenvectors:

$$|1\rangle = (se^{i\phi}, 1, 0, 0)^T/\sqrt{2} \tag{5.10}$$

$$|2\rangle = (0, 0, se^{-i\phi}, 1)^T/\sqrt{2} \tag{5.11}$$

where $s = -i(M - B\kappa^2)/(A^*\kappa) = \pm$ is purely real. These allow us to find the polarizations of the states in terms of the constituent modes $p_+, p_-, d_{x^2-y^2}, d_{xy}$. The solution for the edge wavefunction then has the form

$$|\psi\rangle = \rho(r)(c_1 |1\rangle + c_2 |2\rangle) \tag{5.12}$$

Here $\rho(r)$ is the radial part of the wavefunction. It is only defined for $r < R$ (the modes vanish outside) and peaks close to the edge – as guaranteed by its form:

$$\rho(r) = e^{\kappa_1(r-R)} - e^{\kappa_2(r-R)} \tag{5.13}$$

where the decay constants are given by the two solutions of

$$\kappa^2 = \frac{|A|^2 + 2MB \pm \sqrt{|A|^4 + 4MB|A|^2}}{2B^2} \tag{5.14}$$

which have a positive real part. This solution ensures that the wavefunction vanishes at $r = R$ as required by the boundary conditions. The final step is to find the coefficients $c_{1,2}$. These are obtained treating the azimuthal part of the total Hamiltonian 5.6, $H_{||} = H - H_{\perp}$, as a perturbation. This part has the form

$$H_{||} = \begin{pmatrix} 0 & iAe^{i\phi}k_\phi & 0 & 0 \\ -iA^*e^{-i\phi}k_\phi & 0 & 0 & 0 \\ 0 & 0 & 0 & -iAe^{-i\phi}k_\phi \\ 0 & 0 & iA^*e^{i\phi}k_\phi & 0 \end{pmatrix} \tag{5.15}$$

where we have neglected $Bk_\phi^2 \propto 1/R^2$ term assuming that $R \gg \kappa_{1,2}^{-1}$. Projecting $H_{||}$ onto $|1\rangle, |2\rangle$ we obtain

$$|A|(\sigma_z k_\phi + \frac{1}{2R})\mathbf{c} = w'_{||}\mathbf{c} \tag{5.16}$$

In case of $R \to \infty$ we get continuous edge bands. Each of the two solutions $c_+ = (1,0)^T$ and $c_- = (0,1)^T$ has only p_+, d_+ or p_-, d_- components which represents the pseudo-spin dependent transport properties of the edge states. To obtain the fields one has to take the real part of Eq. 5.4. Note that in case of photonic crystals uniform in z the modes p, d only have x, y-dependence, whereas for the planar metallic surface they also depend on z.

The Dirac crossing together with the mode profiles can also be obtained by considering a straight edge instead of a cylindrical one. This has been done many times in the literature for electronic TIs (e.g. [76]) so instead of repeating the derivation here we study a tight binding model. This is done by transforming the Hamiltonian 5.6 into its coarse-grained tight-binding form as we previously did for the case of electrons. The resulting band structure for a ribbon of the topological crystal displays edge states as seen in Fig. 5.10(b).

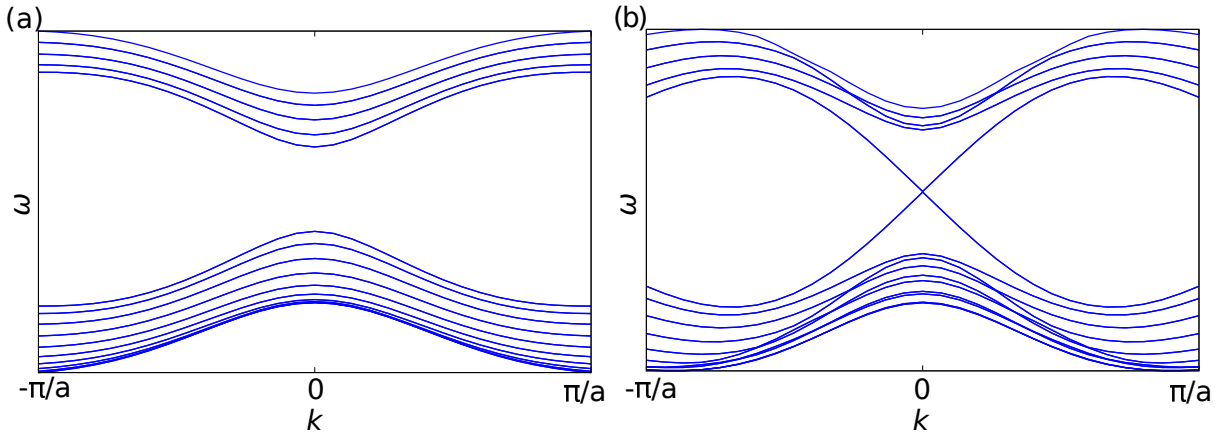

Figure 5.10: (a) Rectangular ribbon of trivial and (b) topological crystal extended infinitely in one direction. The results are obtained by transforming the four band Hamiltonian into a coarse grained tight-binding model. For the topological case the negative mass term inverts band gap.

5.4 Conclusion

In this chapter we have considered three photonic TCIs based on C_6 symmetry. We have shown that for the case of silicon cylinders a topological band gap occurs only for TM polarization and proposed a new photonic TCI made of silicon hexagons which displays topological properties for TE polarization. Furthermore, through simulations we have studied a planar structure of metallic wires and found it to display a band inversion for TM-like modes. In all the above cases the symmetries of the electric and magnetic fields for the modes can be neatly understood using group theory. The latter applied to band structure ($\mathbf{k} \cdot \mathbf{p}$ approximation) allowed us to obtain analytical expression for the frequencies and polarizations of the edge modes.

So far we have only considered bulk structures and those extending infinitely in one dimension (ribbons) – the latter possessing continuous edge bands. One might ask what happens if the the crystal is confined in all directions and the edge states become discrete. This question is of importance to many experiments due to the finite nature of the photonic crystals involved made in practice and we address it in the next chapter.

Chapter 6

Confined photonic topological insulators

Introduction

In the previous chapter we considered photonic TI crystals and have found them to possess boundary states of topological origin. These states are spin-filtered such that photons of opposite polarizations propagate in opposite directions. In practice we would like the devices exploiting this property of photonic TIs to be as small as possible. This motivates the study of confinement effects in topological photonics which have received practically no attention at the time of writing [5].

From what we learned about nanoscale electronic TIs in the previous chapters we expect photonic TI particles (aka cavities) to possess discrete edge states as illustrated in Fig. 6.1. To do so in this chapter we focus on a particular realization of a photonic TI. The first part is devoted to studying a particle carved out of this TI using frequency domain simulations (with the MPB code [59]) – see [5] for details. These are then compared with analytical results for a photonic TI particle of circular cross section. A good agreement is found both in terms of the energies of the edge states as well as their field profiles.

The second part somewhat deviates from the main topic of the chapter – in that it explores limitations of the parent photonic TCI we have chosen for our particle. In particular, we show that as long as the C_6 necessary for topological protection is preserved the states exist for particles of various shapes and can bend around sharp corners.

In the final part we model the dynamical behaviour of light using the finite-difference time-domain approach (see 2.2.4) as implemented in the MEEP code [108]. Such first-principles simulations are possible because photons act as independent particles in the absence of non-linear effects which is the case here (and provide insights into the transport of electronic TI nanoparticles). The simulations show that the discrete states in photonic TCI particles support unidirectional propagation of light which can be switched with its polarization. These findings explain experimental observations of discrete transmission peaks in experiments on photonic TIs [46–48, 50]. The peaks occur because the fabricated photonic TIs in the experiments are small and better considered as particles – cf. electronic TIs containing macroscopic numbers of atoms. The present work shows this and provides guidelines for manipulating the edge states in confined structures. Finally, we find that several particles combined together in a manner of coupled resonator optical waveguide also support unidirectional propagation. The results of this chapter have been published in [5].

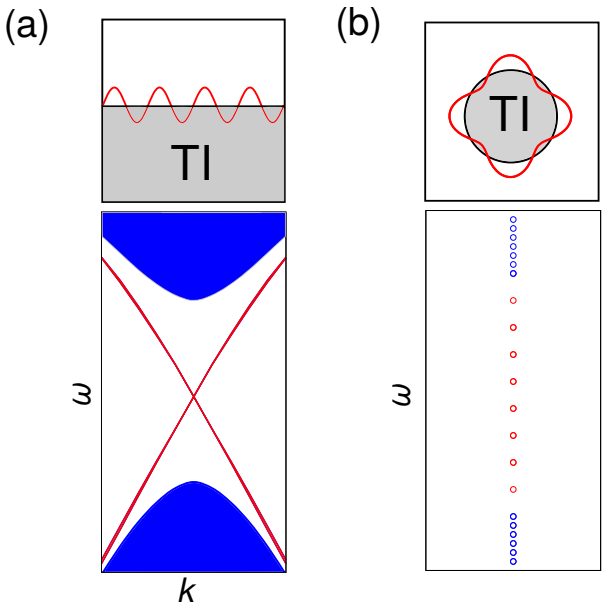

Figure 6.1: (a) Crystals of photonic TIs support continuous edge states at their boundaries. (b) In confined photonic TIs the states become discrete. Figure from [5], 2017, American Physical Society.

6.1 Edge states of a topological particle

6.1.1 Numerical simulations

From the previous chapter it is clear that there are a number of possible designs to consider. Here our focus is on a photonic TCI crystal made of silicon rods [51] – see Fig. 5.2(c). This design is

somewhat easier to simulate but many of the results derived are general. This is because the different designs share a common feature - the Dirac crossing in the photonic band gap. For the chosen TCI the combination of time-reversal and C_6 symmetries can be seen as a "pseudo-time-reversal" symmetry. The latter symmetry plays a role similar to bare time-reversal for electrons and allows us to achieve a photonic TCI phase for TM polarization in this crystal.

Unlike electrons, photons are not confined to a crystal but leak into the surrounding vacuum. It is thus customary, to clad a topological crystal with a trivial crystal such that their band gaps overlap. We thus study the topological particle of hexagonal shape placed inside a trivial matrix with a band gap which acts as a mirror for the edge states. The edge states then occur at the boundary are shown in Fig. 6.2(a). The states calculated in the frequency domain (see 2.2.3 for details) occur in pairs whose number grows linearly with the size of the particle – see Fig. 6.2(b,d). These pseudo-Kramers pairs can be seen as analogues of Kramers pairs of electrons in time-reversal-symmetric TIs. Each state has a particular polarization (pseudo-spin) and supports propagation in one direction only as discussed later. The states are localized at the edges as seen in Fig. 6.2(e). Their E_z fields are shown in Figs. 6.2(c) and Appendix A.4 labelled according to the number of azimuthal nodes. These findings agree well with the analytical model as shown below.

6.1.2 Analytical model of the edge states

In the previous chapter we derived the Dirac equation for the edge modes of a cylindrical particle (Eq. 5.16) which lead to the frequency spectrum given by

$$w = w_0 + \frac{|A|}{R}(\frac{1}{2} \pm m) \tag{6.1}$$

Where $m = 0, \pm 1, \pm 2...$ to ensure periodicity $\mathbf{c}_\pm(2\pi) = \mathbf{c}_\pm(0)$ and it was assumed that $iAs = |A|$ without loss of generality. Each mode is doubly degenerate with the coefficients given by

$$\mathbf{c}_+ = (1 \quad 0)^T e^{im\phi} \qquad c_-(0 \quad 1)^T e^{im\phi} \tag{6.2}$$

Note that the coefficients $\mathbf{c}_\pm$ are orthogonal for any ϕ. For the case of electronic TIs we saw previously that orthogonal coefficients imply the absence of elastic scattering by time-reversal invariant perturbations. In the photonic crystal considered the topological phase exists due to a pseudo-time-reversal symmetry which is a combination of time-reversal symmetry and the C_6 symmetry of the

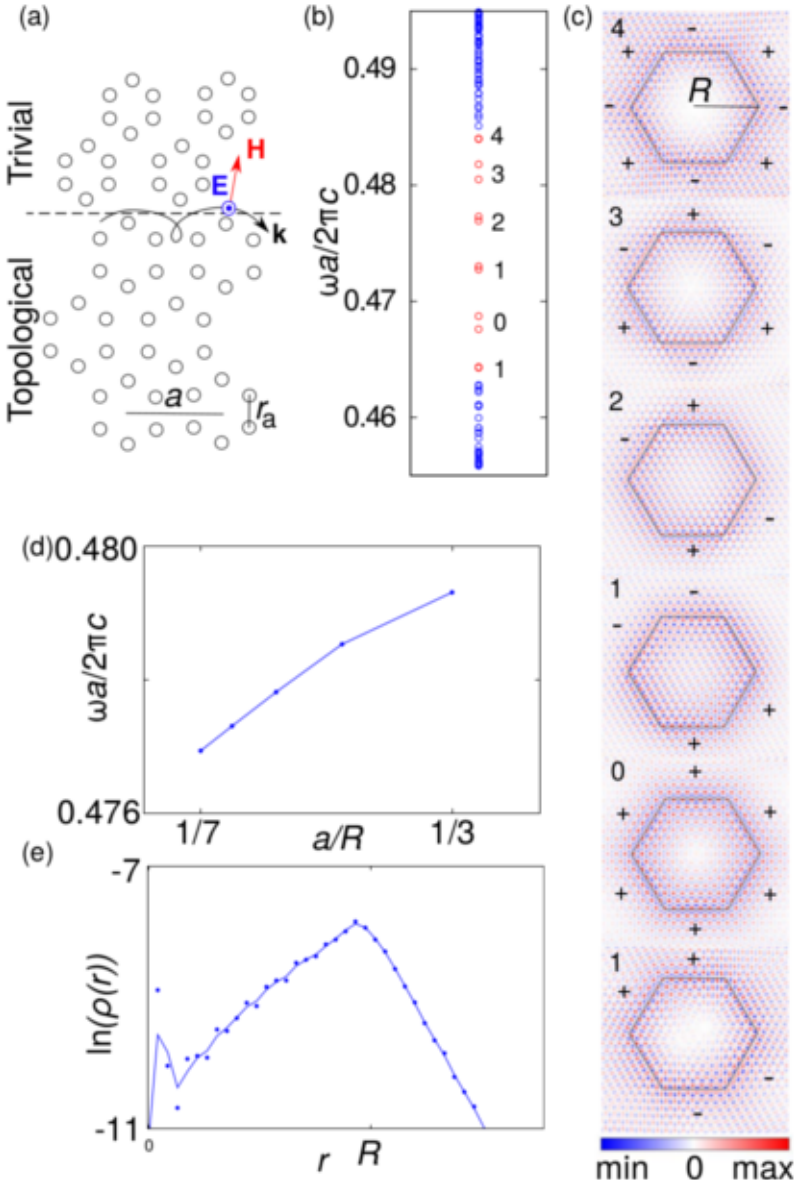

Figure 6.2: (a) The boundary between trivial and topological regions supports edge states. (b) TM spectrum of the photonic TCI particle (169 meta-atoms) embedded in the trivial matrix as obtained with frequency domain simulations. Blue circles show bulk states, red – edge states labelled according to the number of azimuthal nodes. (c) The particle considered hosts 12 edge states. E_z field for half of the states is shown here (see Appendix A.4.1 for the rest). (d) The spacing of the states decreases linearly with the particle's size, R (a – distance between meta-atoms) (e) Radial wavefunction shows that the states are localized at the edges. Figure from [5], 2017, American Physical Society.

crystal. Thus perturbations of these two symmetries act in the same way as a magnetic defect for electronic TIs and localize the states. In the absence of those the edge spectrum consists of states with equal spacing. Each state is doubly degenerate and decays exponentially away from the edge. The degeneracy is required by the time reversal symmetry – at any frequency there should be two states supporting propagation in opposite directions (the splitting of frequencies for each pair seen in Fig. 6.2(b) is a numerical issue and does not occur with FDTD simulations as will be seen below). According to Eq. 6.1 the pairs in the edge spectrum are equidistant. As R grows we expect additional

edge states to emerge from the "valence" and "conduction" bands. Eventually they form a Dirac crossing ($m/R \to k_\phi$) which has a constant density of states as a function of frequency.

Note that according to the analytical model 6.2 there are two states that do not have any nodes – $(+, m = -2)$ and $(-, m = 2)$ – both of which have frequency $w_0 - 3|A|/2R$ [5]. This agrees well with the results in Fig. 6.2(b,c) and Appendix A.4.1. The states immediately above and below in frequency have one node (which is indeed observed with simulations) and so on. Overall, the analytical model of a circular particle agrees well with numerical simulations. The edge states however, exist for particles of many different shapes.

6.2 Varying particle's shape

As discussed previously, the crucial feature of TIs is that because the edge states are imposed by the bulk band structure, they are less sensitive to the edge details provided the relevant symmetries are satisfied. For the photonic TCI considered, the relevant symmetries (time-reversal and C_6) hold, for example, in particles with triangular and rhombic cross section. These also have edge states as seen in Figs. 6.3(c,d) though their profiles are different compared to the hexagonal particle (analogous behaviour was found for infinite samples of electronic TI where the Dirac cone changes depending on the termination of slabs [70] and ribbons [109]). Otherwise they have spectra very similar to that of a hexagonal particle of similar size – see Fig. 6.3(b). The latter is smaller (91 meta-atom) compared to the one shown above in Fig. 6.2 and therefore hosts fewer edge states. Finally, we consider a 'reverse' situation of a trivial particle inside the topological matrix. Analytically the solution is the same except for the radial dependence, Eq. 5.13, which now becomes

$$\rho(r) = e^{-\kappa_1(r-R)} - e^{-\kappa_2(r-R)} \tag{6.3}$$

with R being the radius of the trivial particle. Thus from the model we expect the states to have the same profiles as for the topological particle. This is indeed observed in the simulations – see Fig. 6.3(a). The frequency spectrum is also very similar except for a rigid shift which can be attributed to the slight misalignment of band gaps in bulk TCI and trivial crystals. To conclude, above we have seen how edge states in a photonic TCI particle can bend around sharp corners. Below we investigate this further by studying the effects of structural disorder.

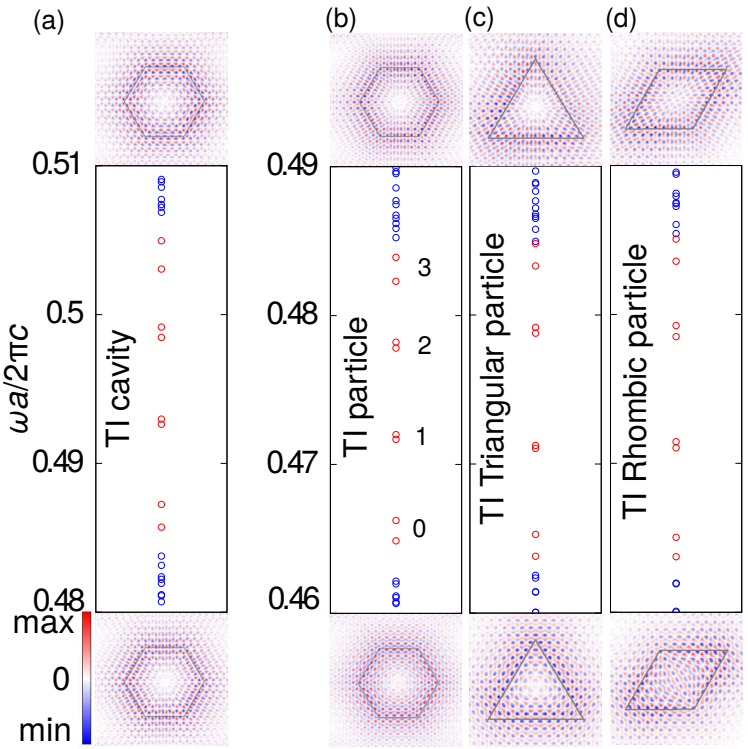

Figure 6.3: Blue circles represent bulk states, red – edge ones. E_z fields of the highest and lowest 'red' states are shown. (a) The 'inverse' case of a trivial cavity (91 meta-atoms) inside a TCI matrix shows practically the same TM spectrum (except for a rigid shift) as (b) The photonic TCI particle of the same size inside the trivial matrix. (c) Triangular and (d) rhombic TCI particles (66 and 64 meta-atoms) also support the edge states which highlights the topological origin of the latter. Figure from [5], 2017, American Physical Society.

6.2.1 Breaking crystal symmetry

The ability of the topological states to bend around corners contrasts sharply with the states of a trivial particle inside a trivial matrix for which Fig. 6.4(a) shows that it has no such edge states spread along the perimeter. As mentioned before, the protection of the states in the photonic TCI considered relies on both time-reversal and crystal C_6 symmetries. This becomes evident when we inflict a strong perturbation of the C_6 crystal symmetry by removing three meta-atoms in Fig. 6.4(b). This completely localizes the states breaking the pseudo-time-reversal symmetry – analogously to a magnetic impurity in an electronic TI. By contrast, substituting the three topological meta-atoms with trivial ones constitutes a relatively weak perturbation of the crystal symmetry as witnessed by Fig. 6.4(c). This immunity of the states to trivial defects can be seen as another example of insensitivity to the particle's shape shown before. Finally, we study the effects of positional disorder by randomly moving rods within each topological meta-atom by 10% which could occur when fabricating such particles. The results in Fig. 6.4 show that the states are robust against such random positional

disorder. A question arises though whether such disordered photonic TCI particles still can support unidirectional propagation of light.

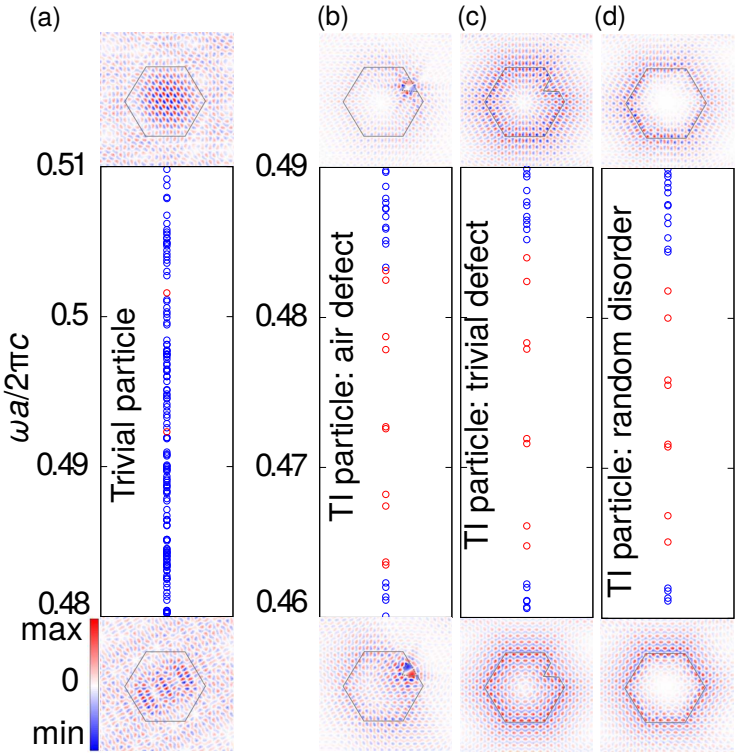

Figure 6.4: Blue circres represent bulk TM states, red – edge ones (except (a)) for a particle of 91 meta-atoms. E_z fields of the highest and lowest 'red' states are shown. (a) Trivial particle inside a trivial matrix does not possess any edge states. (b) For a photonic TCI particle adding an air defect strongly affects the C_6 symmetry and localizes the edge states (acts like a magnetic defect in electronic TIs). (c) Subsituting the three topological atoms with trivial ones practically does not affect the states. (d) The states also survive 10% random disorder in positions of individual rods. The spectra shown can be compared against that of the pristine particleshown in Fig. 6.3(b). Figure from [5], 2017, American Physical Society.

6.3 Unidirectional propagation of a light pulse

6.3.1 Single particle

Above we mentioned that each edge state supports propagation in only one direction. According to the time-reversal symmetry of Maxwell's equations it is required that the two degenerate states in a pair are counterpropagating waves and have opposite pseudo-spins ($H_x \pm iH_y$). To demonstrate this we insert a pulse of light with frequency inside the photonic band gap. The results for the two possible pseudo-spins of the incident pulse are shown in Fig. 6.5(a). It is seen that the pulse propagates either in one or the other direction along the perimeter depending on the pseudo-spin.

The resultant transmission spectrum shown in Fig. 6.5(b) shows discrete peaks [5]. These peaks occur at the frequencies obtained with the MEEP mode solver seen in Fig. 6(c) which in turn agree well with frequency domain results for the particle of the same size seen previously (91 meta-atoms in Fig. 6.3(c)). Note that in the central region of Fig. 6.5(b) the peaks for the opposite pseudo-spins occur at exactly the same frequency which confirms that splitting in each pair observed when using mode solvers is a numerical issue, i.e. in two edge modes in a pair have exactly the same frequency as predicted by 6.1. Fig. 6.5(b) also shows that unidirectional propagation phenomenon sustains a certain degree of disorder and still occurs in the case of randomly shifting the constituent rods by 10%.

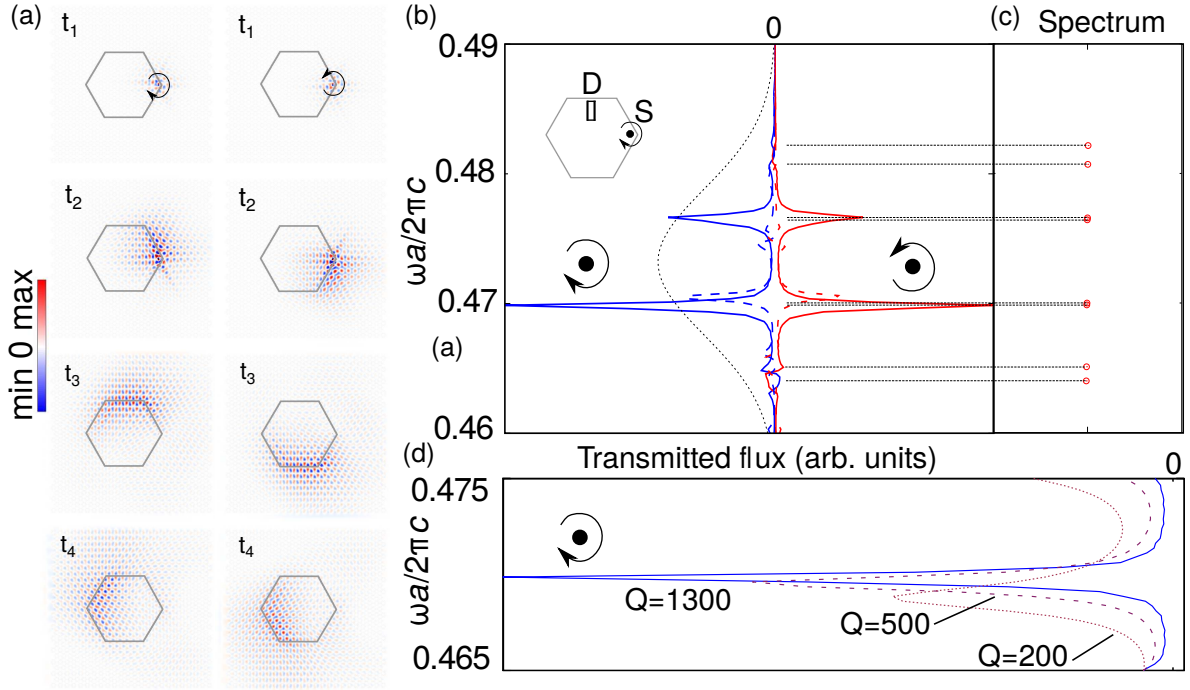

Figure 6.5: (a) Edge states support unidirectional propagation which depends on the pseudo-spin of light ($H_x \pm iH_y$). The TCI particle (91 meta-atoms) is cladded with trivial crystal filling the rest of the simulation cell shown. (b) Each standing wave edge state is made of the counterpropagating waves as required by time-reversal symmetry. The states therefore support propagation in both clockwise (red) and counterclockwise (blue) directions. The height of resultant peaks depends on the distance from the source (S) to the detector (D). The dashed lines show results for particle with positional disorder as in Fig. 6.4(d) and the dotted line – the input Gaussian pulse. (c) The states' frequencies obtained with the FDTD method agree well with those in Fig. 6.3(b). (d) The central peak normalized by the quality factor (Q) broadens as we thin the trivial cladding by two (dashed line) and four atoms (dotted line) compared with that used above. Figure from [5], 2017, American Physical Society.

Finally, we note that the width of the peaks depends on the trivial cladding. In the case of frequency domain simulations seen previously this cladding is infinite and so the frequencies are purely real. For the FDTD simulations here the quality factors of the modes are large – the quality factor, $Q = O(10^3)$

already when the cladding is several atoms thick as seen in Fig. 6.5(d). Note that the pulse used here has the frequency width covering the whole photonic band gap. To probe the nature of individual states we can use a more narrow pulse as done in Fig. 6.6 where Poynting vectors for pulses with two different frequencies are shown.

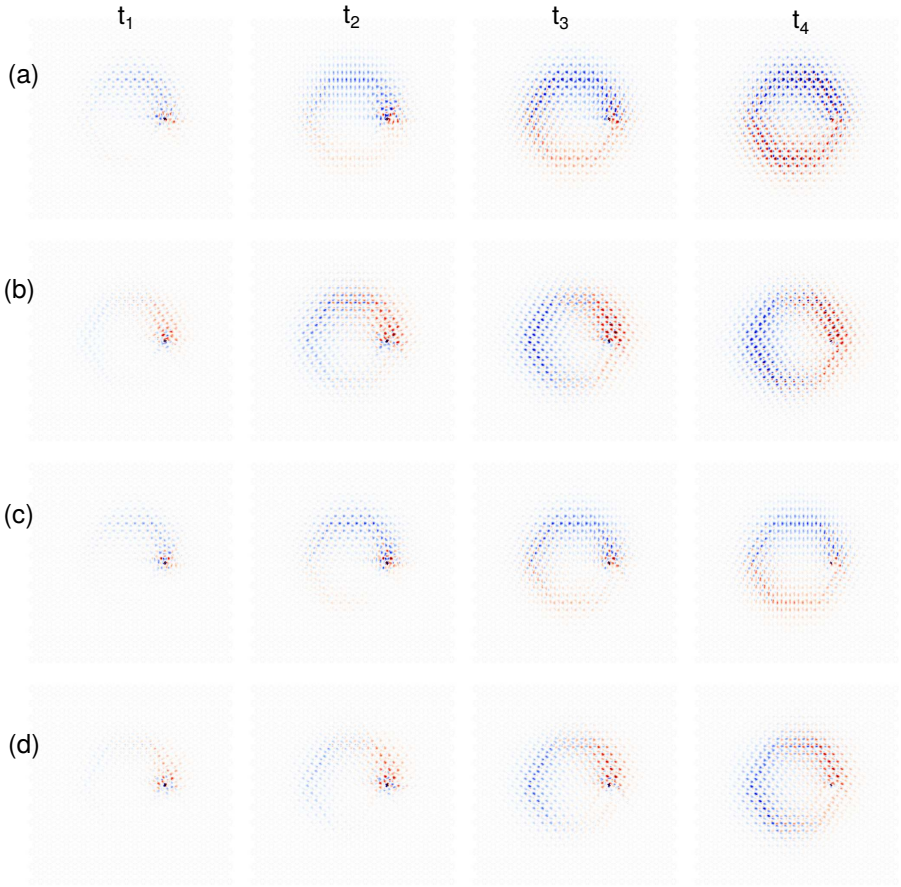

Figure 6.6: Narrow pulse (in frequency) covering only a fraction of the photonic band gap is used to excite individual states (a, b) The x and y components of the Poynting vector for a Gaussian peak centered at $wa/2\pi c = 0.47$. (c, d) Same for $wa/2\pi c = 0.476$. Figure from [5], 2017, American Physical Society.

6.3.2 Crystal made of photonic TI particles

Above we focused on a single topological particle but many of these particles can be brought together to form a coupled resonator optical waveguide. The MPB code with periodic boundary conditions is ideally suited to study such superstructures. To simulate one such waveguide we made the supercell small enough that the periodic images of the particles interact with one another. As a result of this interaction the edge modes on neighbouring particles are no longer independent. The emergent bands obtain dispersion in k-space (are no longer flat) and support propagation of electromagnetic

energy between the particles. This propagation is pseudo-spin dependent as can be seen from Fig. 6.7. Moreover, for the two modes of opposite pseudo-spin in each pair it occurs in the opposite direction.

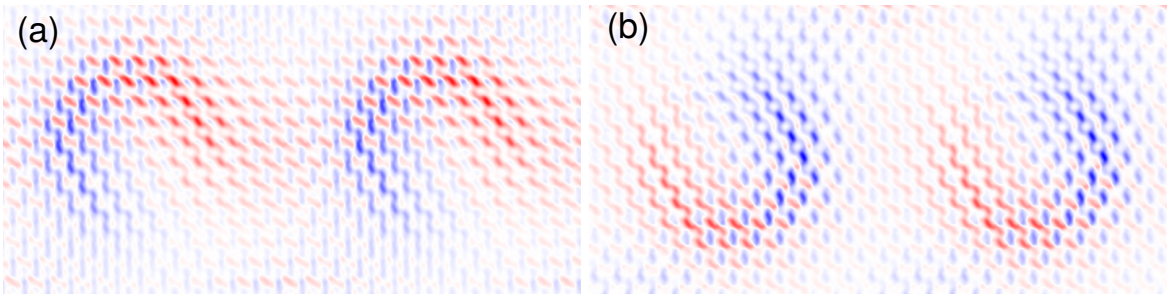

Figure 6.7: Here we consider a particle of size $R/a = 3$ with unit cell size of $11a$ to ensure interaction between the particles. The edge modes are no longer localized and form bands. Each of these edge bands supports unidirectional polarization as from (a) y-component for a single mode and (b) the same for its degenerate counterpart with opposite pseudo-spin (both recorded at $\mathbf{k} = 0.1(\mathbf{G}_1 + \mathbf{G}_2)$).

6.4 Conclusion

We have studied topological photonic particles which possess discrete edge states and obtained their space and frequency characteristics. This has been done using analytical and numerical methods with good agreement between the two. The edge states studied act as topologically protected whispering gallery modes for light. They support unidirectional propagation of light controlled by its pseudo-spin. The present simulations clarify several experimental observations of discrete peaks in transmission [46–48,50,110] which were not explained previously. We believe these peaks occur because the samples of photonic TIs used in these experiments are rather small and are better viewed as particles rather than crystals. For example, typical photonic TIs investigated had $O(10^2)$ atoms which is very far from the numbers involved in studies of electronic TI crystals – $O(10^{23})$, where continuous bands are routinely observed. It is thus important to take finite size effects into account when working with photonic TIs. The present study quantifies the discretization effects and provides guidelines for engineering the topological states. Some possible applications include controlling radiative decay of chiral molecules. The topological particle can also serve as a narrow band filter for one pseudo-spin and perfect mirror - for the other. Furthermore, several particles can be combined in a line to form a coupled resonator optical waveguide which also supports unidirectional propagation.

Chapter 7

Conclusion

"Problems exist to be overcome"

Joseph L. Wheeler

The drive for miniaturization is fueled by several factors – smaller devices are easier to use, they require less materials to produce and consume less energy. These are practical reasons why studying confined topological insulators is important. Because the topological phenomena rely on waves – electronic, light or other, the behavior of TI samples also changes qualitatively somewhat as we reduce the size to a few hundred unit cells. These changes are of fundamental interest and up to date received less than those associated with bulk samples. In addition, they are important to take into account if we want our miniature devices to function properly. In the present the thesis we have shown how confined electronic and photonic TIs display unusual optical properties and the confinement effects need to be taken into account to explain experimental results.

For electronic TIs we considered nanowires and nanoparticles and showed analytically that the discrete surface states in those are protected from elastic backscattering to first order. Analogous results had been previously obtained for continuous states on a planar surface. Furthermore, we related them to a tight binding study of how disorder affects the surface states. The discrete states were found to localize when the strength of disorder potentials becomes comparable to the bulk band gap - the same as for the continuous states in macroscopic samples. The result holds for particles of different shapes as expected from the topological origin of the states. From this we concluded that there is no difference in protection between discrete and continuous TI surface states. Thus, the smallest nanoparticles studied here lie at the opposite end of possible length scales from the bulk samples. More generally,

the protection in the nanoparticles shown here complements that found before for continuous surface states suggesting that the states in particles of intermediate sizes will also be protected. The findings are of importance for application of TI nanoparticles in chemical catalysis as well as for the associated optical effects discussed presently.

After establishing the protection of the surface states, we studied how they affect optical properties of the TI nanostructures. Our main finding was that the surface states in TI nanowires and nanoparticles will interact with bulk optical phonons leading to an extra peak in absorption. This peak will be present in TI nanostructures of different shapes and materials but will be absent for ordinary semiconductors which carry no delocalized surface states. The above suggests that TI nanoparticles can contribute to solving the "THz gap" problem which stands for a region of frequencies where we do not have efficient sources and receivers of radiation. In addition, the states in these nanoparticles may find use as qubits which can be manipulated with polarized light and might show prolonged coherency due to their topological protection. Some of the avenues that require further investigation is the possibility of using the second Dirac cone (existent, e.g. in Bi_2Se_3) to enhance absorption at optical frequencies. At these frequencies the effects of the surface states on the scattering cross-section will be more pronounced. It would also be interesting to investigate the strong coupling regime as well as the effect of the surface states on the local density of photonic states and radiative decay of nearby molecules. Finally, it is worth exploring similar optical effects in 2D TIs such as a single layer of Bi (bismuthene) which are more compact and easier to produce.

Spintronics and quantum information devices are often quoted as likely fields where electronic topological insulators will be used in the future. However, with the even-increasing role of light for information transmission the study of topological effects in photonics appears no less important. The latter include unidirectional propagation of light, polarization dependent filtering as well as an additional degree of freedom which the polarization provides when manipulating light. For these reasons we turned our attention to photonic TIs. Here we suggested a new design of a photonic crystalline TI made of dielectric (infinitely long in z) that supports topological edge states for TE polarization. For practical applications, a more practical design would be a flat topological insulator and therefore we also studied a metallic metasurface and showed that the latter displays band inversion as well as found the associated edge spectrum and polarizations of the states. These results were complemented by the experimental work of our collaborators who have measured the Dirac dispersion and unidirectional propagation in this structure. The planar TCI studied is simple to manufacture being made of thin

metallic wires. The downside is that it relies on crystal symmetry for topological protection and that its edge modes are lossy. Nevertheless, this is an important first step to realizing a scalable planar TI. The main question for further work is how can we do better?

At the moment of writing discrete states in topological nanoparticles are yet to be realised but their photonic analogoues have already made their appearance in man-made topological photonics crystals. In the final chapter we studied the effects of confinement in topological photonics. Using a particular photonic TCI as an example we showed that discrete modes in photonic TIs exist for particles of any shape and support unidirectional propagation. These findings are worth considering in experiments because the photonic TIs made in practice contain about several hundred unit cells and will display confinement effects – this is in contrast to experiments on electronic TIs which involve samples with truly macroscopic numbers of atoms $O(10^{23})$. The derived formulae for the frequencies of the edge states clarify several experimental results and provide guidance to engineer the topological states at will. In future, it would be interesting to study how photonic TI particles modify local density of states and affect emission from chiral molecules.

Overall, topological effects in physics have caused a revolution in the last decade and it was a great privilege to work in this field at the time of making. It is remarkable how classifying bulk band structures of insulators using topological insulators gave rise to so much of new physics which has mostly to do with the boundary states that appear at an interface between a trivial and a topological insulator. Another beautiful thing about TIs is how ideas can be transfered between different subfields – namely, electronic, photonic, acoustic TIs as well as those made of cold atoms. Ultimately this happens as a consequence of the fact that some sort of wave is involved in each of these cases. Moreover, these wave effects in periodic madia can be well captured using the single-particle band structure theory which in many cases provides an accurate description and allows to transfer insights between TI of different types. For example, the protection of continuous states in photonic TIs has not been probed due to a large number of meta-atoms required to make such a sample. However, we expect the continuous states to be protected because we know that discrete states in photonic TIs are and from the electronic TIs we had learned that the protection holds for both discrete and continuous states. On the other hand, light propagation in photonic TI particles provides insight into transport properties of electronic TI nanoparticles where fully first-principles studies are prohibitively expensive. After a decade of research the field still offers many avenues to explore. Particularly, promising is topological photonics due to experimental advances on unidirectional propagation of

light robust against defects. Proof-of-concept designs already exist for microwave and even optical frequencies. Among the benefits will be large savings on scattering losses in such TI waveguides as well as the possibility of building an optical computer. With this in mind, it appears to be a question of time and effort when this problem will be overcome and we will have a simple and scalable photonic TI that could possibly even challenge the historical reign of silicon photonics. As a continuation of the present work it is worth exploring the SToP mode-like behaviour in other topological systems. For example, there appears to be no direct analogy for light (need non-linearity to imitate transitions between edge states) or cold atoms (no phonons because the optical lattice is imposed externally and does not receive feedback) but perhaps other ways exist to achieve it.

Appendix A

Appendices

A.1 Tight-binding studies of topological insulator nanostructures

A.1.1 Schematics of how the particle was constructed

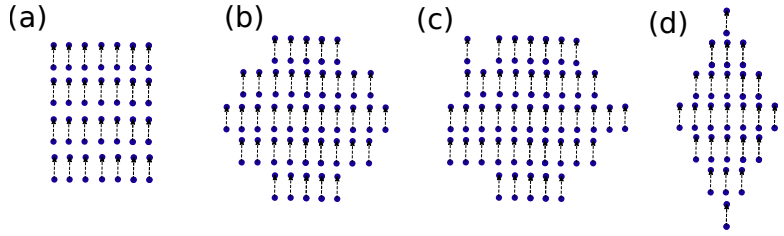

Figure A.1: The objects of the tight-binding simulations are constructed from primitive unit cells oriented along [111] direction. Schematically: (a) slab (b) sphere (c) sphere with surface roughness and (d) rhombohedron. Figure from [2], 2017, American Physical Society.

A.1.2 Particles with different lattice orientations

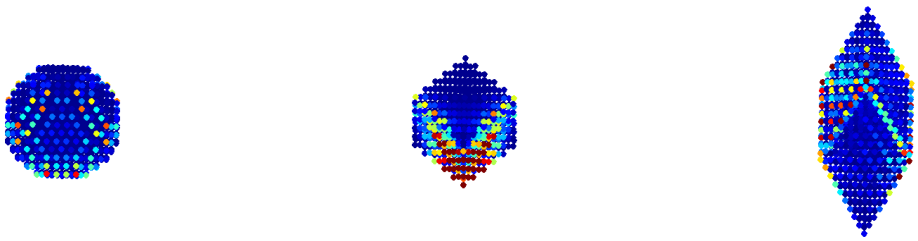

Figure A.2: Particles constructed in the same way as in the main text except the shorter bond for which $t \to t + \delta t$ is now along $[\bar{1}\bar{1}1]$ direction and not [111]. From left to right: spherical, cubic and rhombohedral particle. Figure from [2], 2017, American Physical Society.

A.1.3 Statistical study for surface disorder of strength $V_D = E_G$

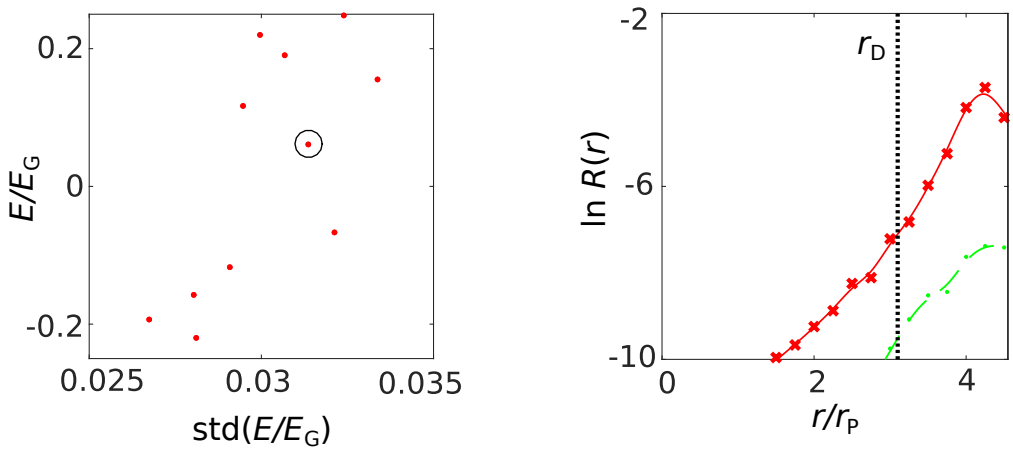

Figure A.3: Mean energy of surface states from 25 disorder realizations with strength $V_D = E_G$ (a) Energy of the state (doubly degenerate) is plotted along the y-axis and its standard deviations – along the x-axis. (b) Mean value of the radial wavefunction (red solid line) for the first state above $E = 0$ (marked with a circle) and its standard deviation (green dashed line). Figure from [2], 2017, American Physical Society.

A.1.4 Topologically trivial particle

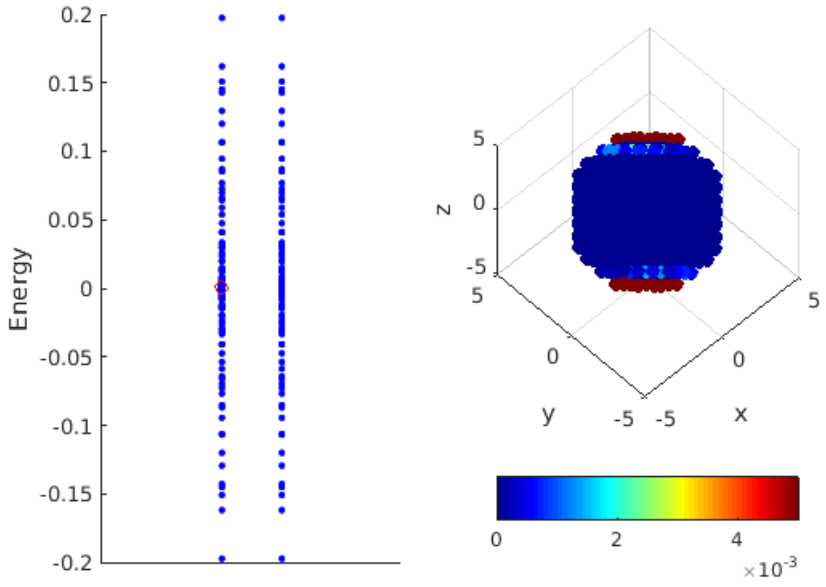

Figure A.4: Spectrum of a spherical TI nanoparticle without spin-orbit coupling contains no topological surface states. Figure from [2], 2017, American Physical Society.

A.1.5 Effects of surface roughness

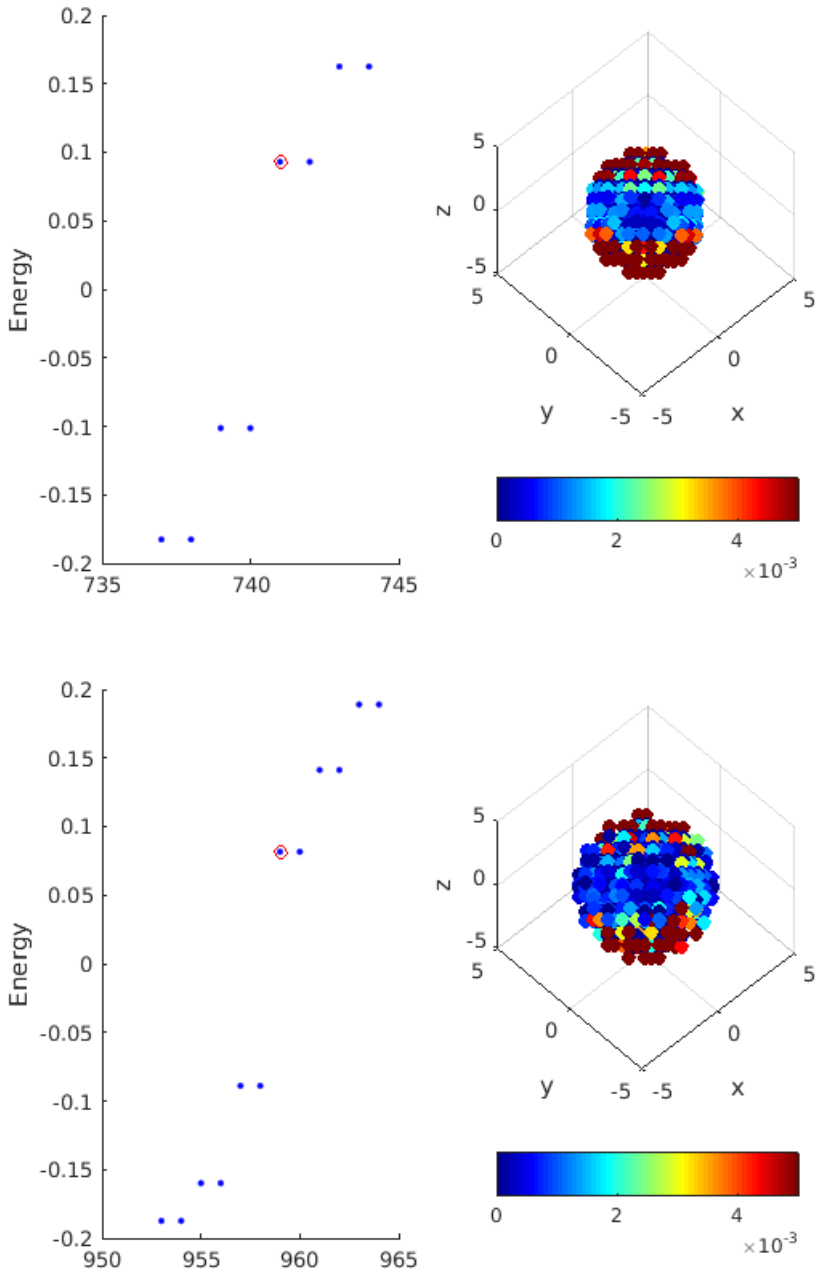

Figure A.5: Top: spherical particle with clean surface. Bottom: the same particle with additional atoms randomly positioned on the surface (in pairs) to imitate surface roughness. Their main effect is to modify the surface states' wavefunctions as well as energies. The energy spacing decreases as the effective radius of the particle grows due to additional atoms. Figure from [2], 2017, American Physical Society.

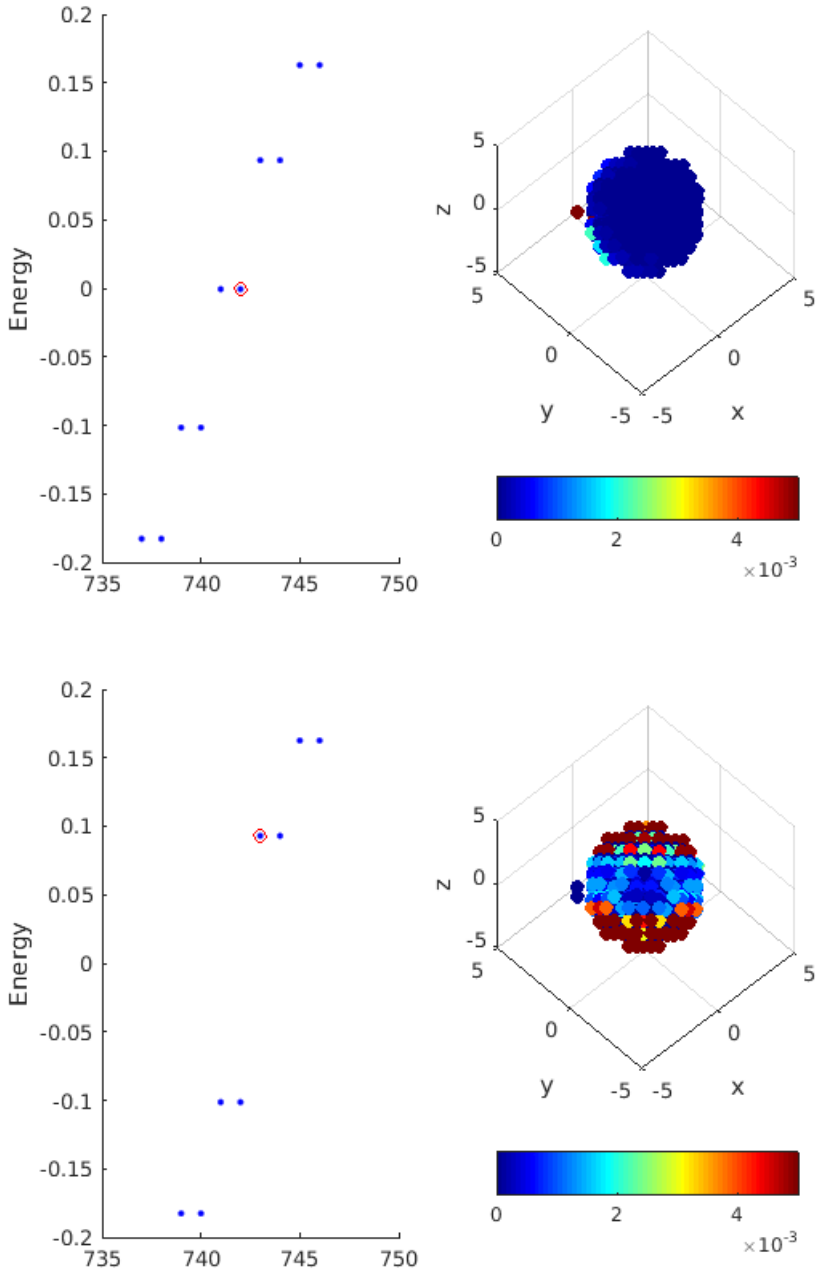

Figure A.6: Top: adding a single atom results in a pair of states close to $E = 0$ (c.f. Fig. A.1). Bottom: adding a unit cell results in two pairs of states – one high above and one – high below in energy (see the eigenvalue number). Figure from [2], 2017, American Physical Society.

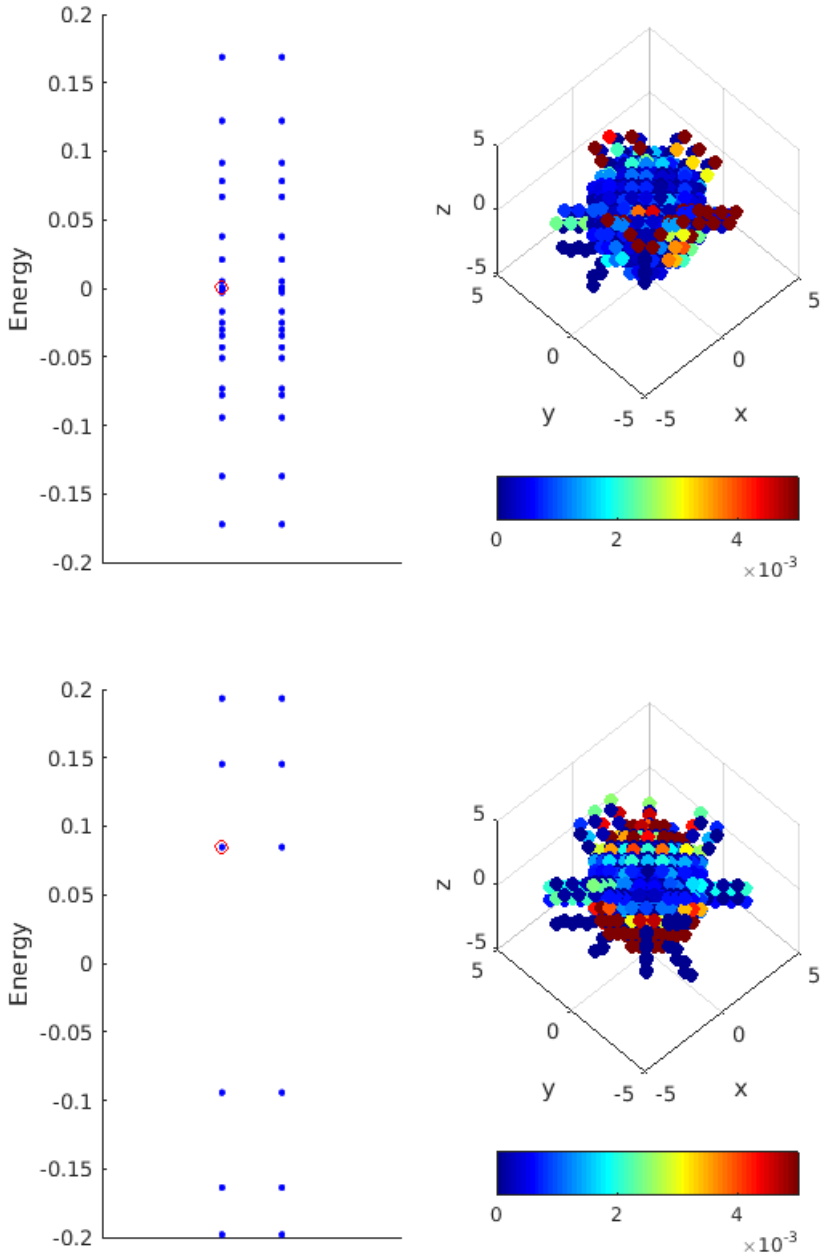

Figure A.7: Demonstrating the unphysical behaviour of the model when adding individual atoms rather than unit cells (pairs of atoms). Top: particle with attached chains of atoms – each containing five atoms. The spectrum and the states change drastically. Bottom: the same particle but now carrying chains of six atoms. When the chains carry an even number of atoms the topological states are practically unaffected as is their energy spectrum. Figure from [2], 2017, American Physical Society.

A.2 Optical properties of topological insulator nanostructures

A.2.1 Light polarisations and degenerate bands

Suppose that we have $V = L\sin\theta\cos(n\phi - wt) + R\sin\theta\cos(n\phi + wt)$, $n \in \mathcal{Z}$. Consider state initial state $|i\rangle = |smk\rangle$ - its resultant surface charge density will have the form

$$LA_1\sin\theta\cos(n\phi - wt) + RA_2\sin\theta\cos(n\phi + wt) \tag{A.1}$$

where A_1, A_2 are some functions of R and w. By symmetry the state $|s(-m)k\rangle$ gives charge density

$$LA_2\sin\theta\cos(n\phi - wt) + RA_1\sin\theta\cos(n\phi + wt) \tag{A.2}$$

so the total density from the two states is

$$(A_1 + A_2)[L\sin\theta\cos(n\phi - wt) + R\sin\theta\cos(n\phi + wt)] \tag{A.3}$$

No matter which polarisation we have $L = 1, R = 0$ or $L = 0, R = 1$ or $L = R = 1/2$ the proportionality constant for the charge density is always $(A_1 + A_2)$. We assume that the states $|smk\rangle$ and $|s(-m)k\rangle$ being degenerate are always simultaneously (un-)occupied.

A.2.2 Dependence of TINW absorption on Fermi energy

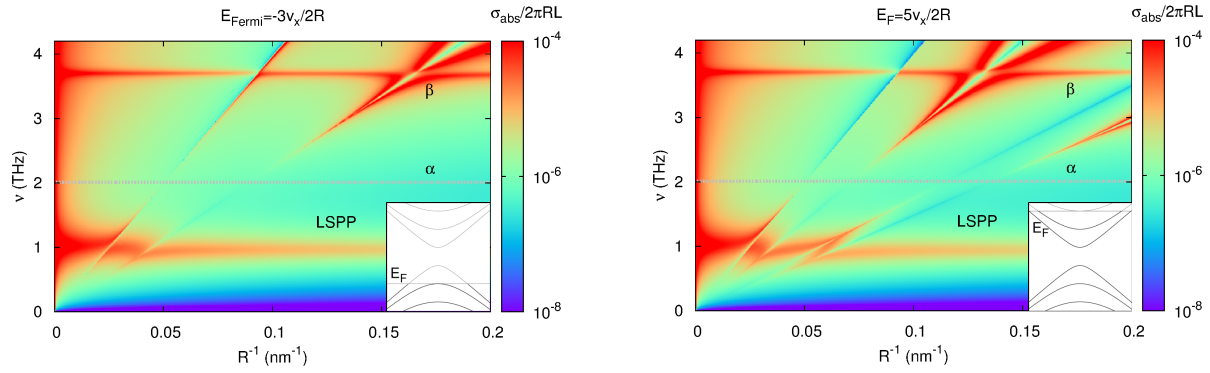

Figure A.8: Absorption cross section for topological insulator nanowire with different Fermi energies.

A.2.3 Surface states of TINP analytically

To find the necessary matrix elements we use the surface states wavefunctions obtained by Imura *et al.* [4] (where wavefunction means the corresponding envelope function). The two-component wavefunctions satisfy the eigenvalue equation

$$\mathcal{H}\psi = \mathcal{H} \begin{pmatrix} c_+ \\ c_- \end{pmatrix} = E \begin{pmatrix} c_+ \\ c_- \end{pmatrix} \tag{A.4}$$

where $\mathcal{H}$ is the Dirac operator on the spherical surface of radius R given by [4]

$$\mathcal{H} = \begin{pmatrix} 0 & \frac{A}{R}(-\partial_\theta + \frac{i\partial_\phi}{\sin\theta} - \frac{\cot\theta}{2}) \\ \frac{A}{R}(\partial_\theta + \frac{i\partial_\phi}{\sin\theta} + \frac{\cot\theta}{2}) & 0 \end{pmatrix} \tag{A.5}$$

It is obtained from the low-energy four-band Hamiltonian of Bi_2Se_3 by projecting it onto two states with momentum along the surface $k_{||} = 0$ [4] (the value of $A = 3.0\,\mathrm{eV}\cdot\text{Å}$ was obtained by averaging the relevant values over x, y and z directions from DFT calculations — see Table IV in [76]). The envelope function $(c_+, c_-)^T$ is an eigenstate and E — the corresponding eigenenergy. The eigenstates are labelled by three quantum numbers - $|s, n, m\rangle$. The "principal" quantum number $n = 0, 1, ...$ and azimuthal quantum number $m = 1/2, 3/2...$ (w.l.o.g. we focus on positive m onwards). The number $s = \pm$ is added for convenience — it denotes whether the state is below or above the Dirac point.

For a particular state $|s, n, m\rangle$ the solution has the form [4]:

$$\psi_{snm}(\theta,\phi) = \frac{e^{im\phi}}{\sqrt{4\pi R^2}} \begin{pmatrix} c_{snm+}(\theta) \\ c_{snm-}(\theta) \end{pmatrix} =$$

$$\frac{e^{im\phi}}{\sqrt{4\pi R^2}} \begin{pmatrix} (1-\cos\theta)^{\frac{1}{2}(m-\frac{1}{2})}(1+\cos\theta)^{\frac{1}{2}(m+\frac{1}{2})}\beta_{nm+}(\cos\theta) \\ -sgn(sm)(1-\cos\theta)^{\frac{1}{2}(m+\frac{1}{2})}(1+\cos\theta)^{\frac{1}{2}(m-\frac{1}{2})}\beta_{nm-}(\cos\theta) \end{pmatrix} \tag{A.6}$$

where $\beta_{nm\sigma}$ are Jacobi polynomials:

$$\beta_{nm\sigma}(x) = N_{nm} J_n^{(m-\frac{\sigma}{2})(m+\frac{\sigma}{2})}(x) \tag{A.7}$$

with N_{nm} being the normalisation constant determined by

$$\int_{-1}^{1} dx(1-x)^{\alpha}(1+x)^{\beta}J_n^{\alpha\beta}J_{n'}^{\alpha\beta} = \delta_{nn'}\frac{2^{\alpha+\beta+1}(n+\alpha)!(n+\beta)!}{(2n+\alpha+\beta+1)(n+\alpha+\beta)!n!} = \delta_{nn'}\frac{1}{N_{nm}^2} \tag{A.8}$$

where $\alpha = m - \sigma/2$ and $\beta = m + \sigma/2$ in our case. The states are normalised over the surface of the particle and satisfy:

$$\langle s, n, m | s', n', m' \rangle = \delta_{s,s'}\delta_{n,n'}\delta_{m,m'} \tag{A.9}$$

Their energy is given by

$$E_{snm} = s\frac{A}{R}\left(n + |m| + \frac{1}{2}\right) \tag{A.10}$$

So the states are equally spaced with degeneracy increasing linearly in energy, i.e. 2, 4, 6, 8 etc.

A.2.4 Surface states of the TINP with coarse-grained tight-binding

Our calculations are based on the model Imura *et al.* [4] who used the four-band low-energy Hamiltonian to obtain tight-binding Hamiltonian using the substitutions:

$$k_i \to \frac{1}{L}\sin k_i L \tag{A.11}$$

$$k_i^2 \to \frac{2}{L^2}(1 - \cos k_i L) \tag{A.12}$$

where $i = x, y, z$. This yields the following Hamiltonian:

$$H = \tau_z(m_0 + \frac{2}{L^2}\sum_i m_2(1 - \cos k_i L)) + \frac{1}{L}A\tau_x\sum_i \sigma_i \sin k_i L \tag{A.13}$$

The Hamiltonian above can be Fourier transformed yielding a nearest neighbour model on cubic lattice in real space:

$$H = \sum_{lmn}(m_0 + \frac{2}{L^2}m_2)\tau_z c_{lmn}^{\dagger}c_{lmn} + \sum_{lmn}[(-\frac{1}{L^2}m_2\tau_z - \frac{i}{2L}A\tau_x\sigma_x)c_{l+1mn}^{\dagger}c_{lmn} + \sigma_y, \sigma_z \text{ terms}] \tag{A.14}$$

For the Hamiltonian above we use values for Bi_2Se_3 from DFT calculations averaged over x, y and z directions [76]: $m_0 = -0.28$ eV, $A = 3.0\,\text{eV}\cdot\text{Å}$, $m_2 = 32\,\text{eV}\cdot\text{Å}^2$. The decay constant of surface states

into the bulk with these parameters is given by Eq. 15 in [4]:

$$\mathrm{Re}[\kappa] = \mathrm{Re}\left[\frac{A \pm \sqrt{A^2 + 4m_0 m_2}}{2m_2}\right] \approx 0.5\,\mathrm{nm}^{-1} \tag{A.15}$$

The only 'fitting' parameter for the tight-binding model is the length between the lattice points, L. We take $L = 29\,\text{Å}$ in accordance with the repeat length of Bi_2Se_3 hexagonal cell along the c-axis (28.64 Å). It also agrees with tight-binding simulations of Egger *et al.* [39] who set $L = 28\,\text{Å}$. Thus our coarse grained model consists of cubic cells each representing several primitive unit cells of the material. This is justified because we are only interested in delocalised surface states lying low in energy. Examples of energy spectra close to the Dirac point for cubic and spherical shapes are shown below in Fig. A.9. The spectrum is symmetric around the Dirac point due to the particle hole symmetry inherent in the initial model Hamiltonian [4]. The states closest to the Dirac point are in best agreement between the analytical and tight-binding models. The deviations further from the Dirac point occur due to the small sizes of the particles than are computationally attainable. Nevertheless, the energy spacing between levels is constant and degeneracy follows the pattern 2, 4, 6, 8... as predicted by the analytical model in Eq. A.10. Similarity of spectra for cubic and spherical shapes highlights the topological nature of the surface states.

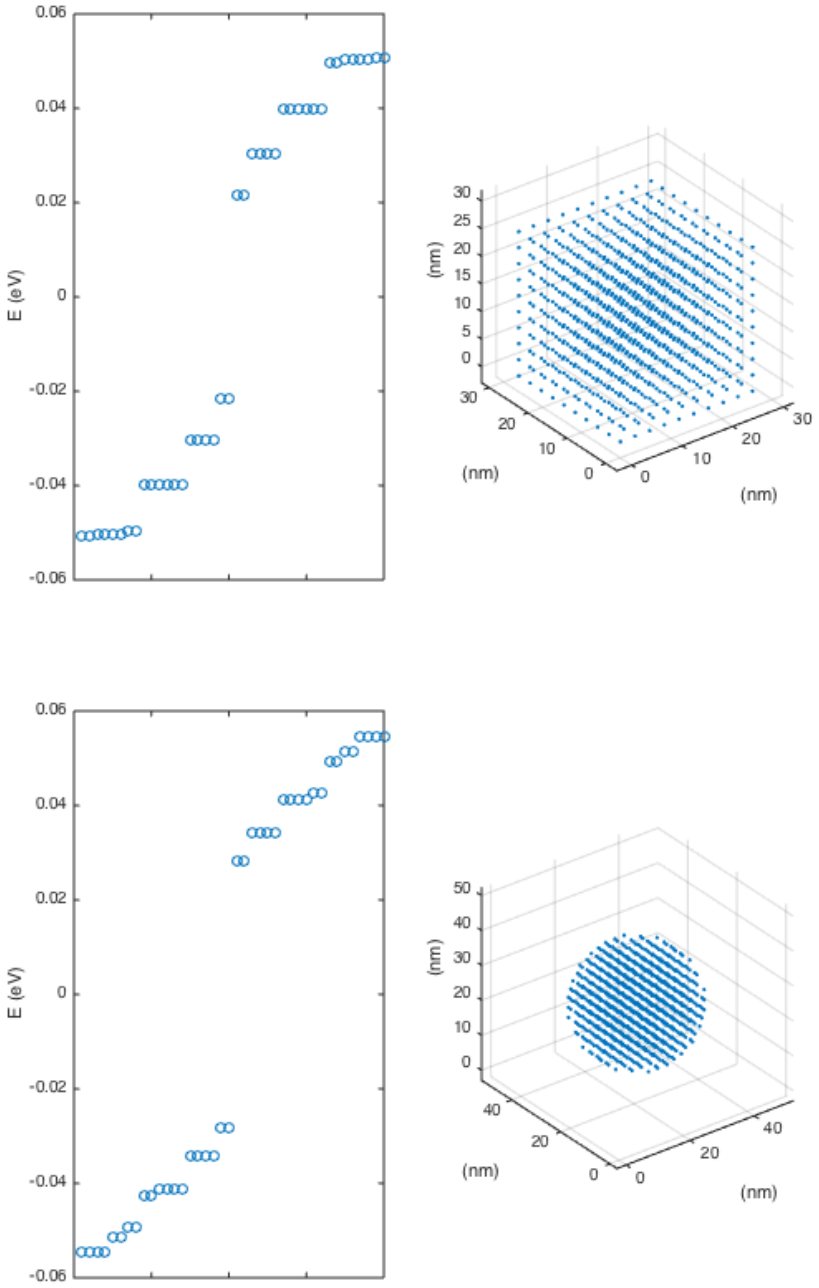

Figure A.9: Left: energy spectrum of a cube made of $N = 1000$ lattice points corresponding to $R = 18\,\text{nm}$ in Fig. 2 of the article ($NL^3 = 4\pi R^3/3$) Right: Same for a sphere made of $N = 895$ lattice points corresponding to $R = 17.4\,\text{nm}$. In both cases the energy levels are equally spaced and degeneracy follows the pattern 2, 4, 6, 8 as predicted by the analytical model.

A.3 Photonic TIs

A.3.1 Parameters for MPB, MEEP and SCUFF-EM

For the simulation of silicon cylinders we used $\epsilon = 11.7$, $d = 2a/9$ where a is the unit cell size. For the topological and trivial phases we used $a/r = 2.9$ and $a/r = 3.125$ respectively.

For the case of hexagonal blocks we also used $\epsilon = 11.7$. The structure is more easily thought of in terms of the air gaps inside each unit cell. These gaps form a hexagon-like star (see red hexagon in Fig. 5.5), i.e. a hexagon such that each corner contains an additional rectangular gap (a ray) going outside. The phase of the crystal is determined by the length of the gaps forming the hexagons vs those forming its rays. When these are both equal to $a/3$ we get a bulk Dirac cone in the 1BZ. For the topological and trivial phase we used lengths $a/2.9$ and $a/3.125$ for the sides of hexagons - the rays connecting the hexagons between the unit cells had length of $1 - 2a/2.9$ and $1 - 2a/3.125$ respectively.

As mentioned in the main text the 2D view of the perfect metal metasurface can be thought of as the inverse of the above structure where the air gaps are instead filled with a perfect conductor (and the structure is thin in z). For this 2D structure of a perfect metal we used $a/2.7$ and $a/3.3$ for the side lengths of "expanded" and "contracted" hexagon structures respectively with the rays between the hexagons adjusted correspondingly. For the MEEP simulations we used a thickness of $a/10$ rather than an infinitely thin structure because the code only supports uniform FDTD meshes and it becomes prohibitively expensive to calculate thinner structures. As a result the Dirac crossing occurs at a $wa/2\pi c \approx 1.11 - 1.14$ which is five per cent higher than that obtained with SCUFF-EM ($1.06 - 1.10$). This can be attributed to the height and meshing differences (SCUFF-EM supports infinitely thin structures and triangular meshing). The MEEP code also allowed us to obtain a band structure for this metasurface. However, the results are somewhat noisy because the code only supports rectangular unit cells (double of the primitive unit cell) - this is partially cured by using two sources within the rectangular unit cell by the delayed Bloch phase such that they only excite the modes within the 1BZ of the primitive unit cell. The result is shown in Fig. A.10.

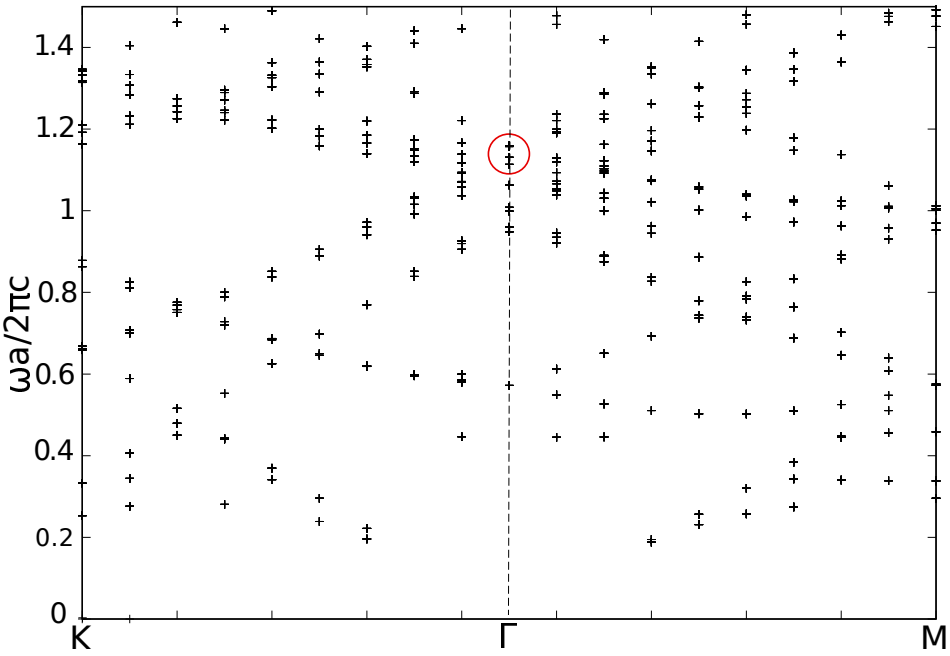

Figure A.10: The band structure for the 2D hexagonal array of metallic wires. The crossing around 1.15 at the Γ point (red circle) leads to a topological band gap by adjusting the structure accordingly.

A.3.2 Coarse grained tight-binding model for photonics

The approach here is the same as that in A.2.4. The tight-binding Hamiltonian can be obtained from the $\mathbf{k} \cdot \mathbf{p}$ Hamiltonian 5.6 with the substitutions:

$$M + Bk^2 \rightarrow M + B\frac{2}{L}(2 - \cos k_x L - \cos k_y L) \tag{A.16}$$

$$Ak_{x,y} \rightarrow A\frac{1}{L}\sin k_{x,y} L \tag{A.17}$$

We simulated a ribbon of ten unit cells in width and used the parameters $A = 2i, B = 1, L = 2$ as well as $M = \pm 1/2$ for the trivial and topological phase respectively.

A.4 Confined photonic TI

A.4.1 Edge states from frequency-domain simulations

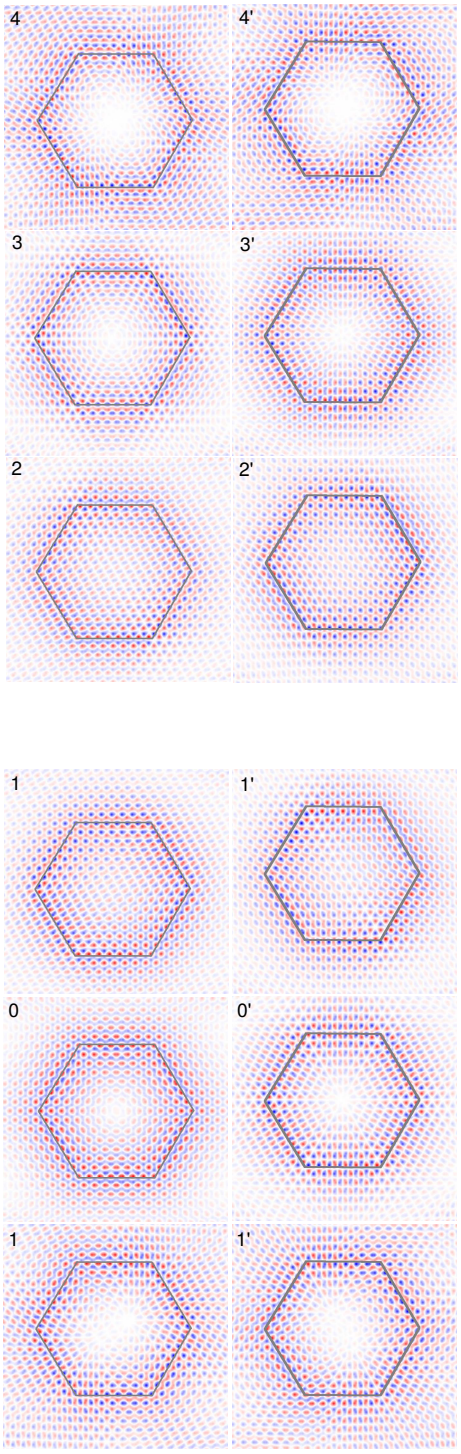

Figure A.11: E_z field for edge states of photonic TI particle $R/a = 7$ (169 meta-atoms). Pairs of states (rows) from bottom to top are arranged according to frequency. Labels denote the number of nodes. Figure from [5], 2017, American Physical Society.

Bibliography

[1] N. P. Butch, K. Kirshenbaum, P. Syers, A. B. Sushkov, G. S. Jenkins, H. D. Drew, and J. Paglione. Strong surface scattering in ultrahigh-mobility Bi2Se3 topological insulator crystals. *Phys. Rev. B*, 81(24):241301, June 2010.

[2] Gleb Siroki, Peter D. Haynes, Derek K. K. Lee, and Vincenzo Giannini. Protection of surface states in topological nanoparticles. *Physical Review Materials*, 1(2):024201, July 2017.

[3] Ken-Ichiro Imura, Yositake Takane, and Akihiro Tanaka. Spin Berry phase in anisotropic topological insulators. *Phys. Rev. B*, 84(19):195406, November 2011.

[4] Ken-Ichiro Imura, Yukinori Yoshimura, Yositake Takane, and Takahiro Fukui. Spherical topological insulator. *Phys. Rev. B*, 86(23):235119, December 2012.

[5] Gleb Siroki, Paloma A. Huidobro, and Vincenzo Giannini. Topological photonics: From crystals to particles. *Physical Review B*, 96(4):041408, July 2017.

[6] A. Femius Koenderink, Andrea Al, and Albert Polman. Nanophotonics: Shrinking light-based technology. *Science*, 348(6234):516–521, May 2015.

[7] M. Z. Hasan and C. L. Kane. Colloquium: Topological insulators. *Rev. Mod. Phys.*, 82(4):3045–3067, November 2010.

[8] Xiao-Liang Qi and Shou-Cheng Zhang. Topological insulators and superconductors. *Rev. Mod. Phys.*, 83(4):1057–1110, October 2011.

[9] Yoichi Ando. Topological Insulator Materials. *J. Phys. Soc. Jpn.*, 82(10):102001, September 2013.

[10] Carlo Sirtori. Applied physics: Bridge for the terahertz gap. *Nature*, 417(6885):132–133, May 2002.

[11] Daniel M. Mittleman. Frontiers in terahertz sources and plasmonics. *Nature Phot*, 7(9):666–669, September 2013.

[12] C. L. Kane and E. J. Mele. $\mathcal{Z}_2$ Topological Order and the Quantum Spin Hall Effect. *Phys. Rev. Lett.*, 95(14):146802, September 2005.

[13] D. J. Thouless, M. Kohmoto, M. P. Nightingale, and M. den Nijs. Quantized Hall Conductance in a Two-Dimensional Periodic Potential. *Phys. Rev. Lett.*, 49(6):405–408, August 1982.

[14] Haijun Zhang, Chao-Xing Liu, Xiao-Liang Qi, Xi Dai, Zhong Fang, and Shou-Cheng Zhang. Topological insulators in Bi2Se3, Bi2Te3 and Sb2Te3 with a single Dirac cone on the surface. *Nat Phys*, 5(6):438–442, June 2009.

[15] Binghai Yan, Martin Jansen, and Claudia Felser. A large-energy-gap oxide topological insulator based on the superconductor BaBiO3. *Nat Phys*, 9(11):709–711, November 2013.

[16] S. V. Eremeev, I. V. Silkin, T. V. Menshchikova, A. P. Protogenov, and E. V. Chulkov. New topological surface state in layered topological insulators: Unoccupied dirac cone. *Jetp Lett.*, 96(12):780–784, February 2013.

[17] Oleg V. Yazyev, Joel E. Moore, and Steven G. Louie. Spin Polarization and Transport of Surface States in the Topological Insulators Bi2Se3 and Bi2Te3 from First Principles. *Phys. Rev. Lett.*, 105(26):266806, December 2010.

[18] D. Hsieh, Y. Xia, D. Qian, L. Wray, J. H. Dil, F. Meier, J. Osterwalder, L. Patthey, J. G. Checkelsky, N. P. Ong, A. V. Fedorov, H. Lin, A. Bansil, D. Grauer, Y. S. Hor, R. J. Cava, and M. Z. Hasan. A tunable topological insulator in the spin helical Dirac transport regime. *Nature*, 460(7259):1101–1105, August 2009.

[19] S. R. Park, W. S. Jung, Chul Kim, D. J. Song, C. Kim, S. Kimura, K. D. Lee, and N. Hur. Quasiparticle scattering and the protected nature of the topological states in a parent topological insulator Bi2Se3. *Phys. Rev. B*, 81(4):041405, January 2010.

[20] Fan Zhang, C. L. Kane, and E. J. Mele. Surface states of topological insulators. *Phys. Rev. B*, 86(8):081303, August 2012.

[21] Richard C. Hatch, Marco Bianchi, Dandan Guan, Shining Bao, Jianli Mi, Bo Brummerstedt Iversen, Louis Nilsson, Liv Hornekr, and Philip Hofmann. Stability of the Bi2Se3(111) topolog-

ical state: Electron-phonon and electron-defect scattering. *Phys. Rev. B*, 83(24):241303, June 2011.

[22] Z.-H. Pan, A. V. Fedorov, D. Gardner, Y. S. Lee, S. Chu, and T. Valla. Measurement of an Exceptionally Weak Electron-Phonon Coupling on the Surface of the Topological Insulator Bi2Se3 Using Angle-Resolved Photoemission Spectroscopy. *Phys. Rev. Lett.*, 108(18):187001, May 2012.

[23] Namrata Bansal, Yong Seung Kim, Matthew Brahlek, Eliav Edrey, and Seongshik Oh. Thickness-Independent Transport Channels in Topological Insulator Bi2Se3 Thin Films. *Phys. Rev. Lett.*, 109(11):116804, September 2012.

[24] J. W. McIver, D. Hsieh, H. Steinberg, P. Jarillo-Herrero, and N. Gedik. Control over topological insulator photocurrents with light polarization. *Nat Nano*, 7(2):96–100, February 2012.

[25] D. Hsieh, F. Mahmood, J. W. McIver, D. R. Gardner, Y. S. Lee, and N. Gedik. Selective Probing of Photoinduced Charge and Spin Dynamics in the Bulk and Surface of a Topological Insulator. *Phys. Rev. Lett.*, 107(7):077401, August 2011.

[26] P. Olbrich, L.E. Golub, T. Herrmann, S.N. Danilov, H. Plank, V.V. Belkov, G. Mussler, Ch. Weyrich, C.M. Schneider, J. Kampmeier, D. Grtzmacher, L. Plucinski, M. Eschbach, and S.D. Ganichev. Room-Temperature High-Frequency Transport of Dirac Fermions in Epitaxially Grown Sb2Te3 and Bi2Te3-Based Topological Insulators. *Phys. Rev. Lett.*, 113(9):096601, August 2014.

[27] R. Valds Aguilar, A. V. Stier, W. Liu, L. S. Bilbro, D. K. George, N. Bansal, L. Wu, J. Cerne, A. G. Markelz, S. Oh, and N. P. Armitage. Terahertz Response and Colossal Kerr Rotation from the Surface States of the Topological Insulator Bi2Se3. *Phys. Rev. Lett.*, 108(8):087403, February 2012.

[28] P. Di Pietro, M. Ortolani, O. Limaj, A. Di Gaspare, V. Giliberti, F. Giorgianni, M. Brahlek, N. Bansal, N. Koirala, S. Oh, P. Calvani, and S. Lupi. Observation of Dirac plasmons in a topological insulator. *Nature Nano*, 8(8):556–560, August 2013.

[29] Lukas Zhao, Marcin Konczykowski, Haiming Deng, Inna Korzhovska, Milan Begliarbekov, Zhiyi Chen, Evangelos Papalazarou, Marino Marsi, Luca Perfetti, Andrzej Hruban, Agnieszka Woo,

and Lia Krusin-Elbaum. Stable topological insulators achieved using high energy electron beams. *Nature Commun*, 7:10957, March 2016.

[30] Anthony Vargas, Susmita Basak, Fangze Liu, Baokai Wang, Eugen Panaitescu, Hsin Lin, Robert Markiewicz, Arun Bansil, and Swastik Kar. The Changing Colors of a Quantum-Confined Topological Insulator. *ACS Nano*, 8(2):1222–1230, February 2014.

[31] Jing Wang. Calculation of divergent photon absorption in ultrathin films of a topological insulator. *Phys. Rev. B*, 88(19), 2013.

[32] J.A. Sobota, S.-L. Yang, D. Leuenberger, A.F. Kemper, J.G. Analytis, I.R. Fisher, P.S. Kirchmann, T.P. Devereaux, and Z.-X. Shen. Distinguishing Bulk and Surface Electron-Phonon Coupling in the Topological Insulator bi2se3 Using Time-Resolved Photoemission Spectroscopy. *Phys. Rev. Lett.*, 113(15):157401, October 2014.

[33] Benjamin M. Fregoso, Y. H. Wang, N. Gedik, and Victor Galitski. Driven electronic states at the surface of a topological insulator. *Phys. Rev. B*, 88(15):155129, October 2013.

[34] Y. H. Wang, H. Steinberg, P. Jarillo-Herrero, and N. Gedik. Observation of Floquet-Bloch States on the Surface of a Topological Insulator. *Science*, 342(6157):453–457, October 2013.

[35] Yi Zhang, Ke He, Cui-Zu Chang, Can-Li Song, Li-Li Wang, Xi Chen, Jin-Feng Jia, Zhong Fang, Xi Dai, Wen-Yu Shan, Shun-Qing Shen, Qian Niu, Xiao-Liang Qi, Shou-Cheng Zhang, Xu-Cun Ma, and Qi-Kun Xue. Crossover of the three-dimensional topological insulator Bi2Se3 to the two-dimensional limit. *Nat Phys*, 6(8):584–588, August 2010.

[36] L. Brey and H. A. Fertig. Electronic states of wires and slabs of topological insulators: Quantum Hall effects and edge transport. *Phys. Rev. B*, 89(8):085305, February 2014.

[37] P. G. Silvestrov, P. W. Brouwer, and E. G. Mishchenko. Spin and charge structure of the surface states in topological insulators. *Phys. Rev. B*, 86(7):075302, August 2012.

[38] J. H. Bardarson, P. W. Brouwer, and J. E. Moore. Aharonov-Bohm Oscillations in Disordered Topological Insulator Nanowires. *Phys. Rev. Lett.*, 105(15):156803, October 2010.

[39] R. Egger, A. Zazunov, and A. Levy Yeyati. Helical Luttinger Liquid in Topological Insulator Nanowires. *Phys. Rev. Lett.*, 105(13):136403, September 2010.

[40] Yi Zhang and Ashvin Vishwanath. Anomalous Aharonov-Bohm Conductance Oscillations from Topological Insulator Surface States. *Phys. Rev. Lett.*, 105(20):206601, November 2010.

[41] V. Parente, P. Lucignano, P. Vitale, A. Tagliacozzo, and F. Guinea. Spin connection and boundary states in a topological insulator. *Phys. Rev. B*, 83(7):075424, February 2011.

[42] Titus Neupert, Stephan Rachel, Ronny Thomale, and Martin Greiter. Interacting Surface States of Three-Dimensional Topological Insulators. *Phys. Rev. Lett.*, 115(1):017001, June 2015.

[43] Ling Lu, John D. Joannopoulos, and Marin Soljai. Topological photonics. *Nature Photon.*, 8:821–829, November 2014.

[44] Mikael C. Rechtsman, Julia M. Zeuner, Yonatan Plotnik, Yaakov Lumer, Daniel Podolsky, Felix Dreisow, Stefan Nolte, Mordechai Segev, and Alexander Szameit. Photonic Floquet topological insulators. *Nature*, 496(7444):196–200, April 2013.

[45] M. Hafezi, S. Mittal, J. Fan, A. Migdall, and J. M. Taylor. Imaging topological edge states in silicon photonics. *Nature Photonics*, 7(12):1001–1005, December 2013.

[46] Zheng Wang, Yidong Chong, J. D. Joannopoulos, and Marin Soljai. Observation of unidirectional backscattering-immune topological electromagnetic states. *Nature*, 461(7265):772–775, October 2009.

[47] Scott A. Skirlo, Ling Lu, Yuichi Igarashi, Qinghui Yan, John Joannopoulos, and Marin Soljai. Experimental Observation of Large Chern Numbers in Photonic Crystals. *Phys. Rev. Lett.*, 115(25):253901, December 2015.

[48] Xiaojun Cheng, Camille Jouvaud, Xiang Ni, S. Hossein Mousavi, Azriel Z. Genack, and Alexander B. Khanikaev. Robust reconfigurable electromagnetic pathways within a photonic topological insulator. *Nat. Mater.*, 15(5):542–548, May 2016.

[49] Alexey Slobozhanyuk, S. Hossein Mousavi, Xiang Ni, Daria Smirnova, Yuri S. Kivshar, and Alexander B. Khanikaev. Three-dimensional all-dielectric photonic topological insulator. *Nature Photon.*, 11:130–136, December 2016.

[50] Simon Yves, Romain Fleury, Thomas Berthelot, Mathias Fink, Fabrice Lemoult, and Geoffroy Lerosey. Crystalline metamaterials for topological properties at subwavelength scales. *Nature Communications*, 8:16023, July 2017.

[51] Long-Hua Wu and Xiao Hu. Scheme for Achieving a Topological Photonic Crystal by Using Dielectric Material. *Phys. Rev. Lett.*, 114(22):223901, June 2015.

[52] K. Y. Bliokh, F. J. Rodrguez-Fortuo, F. Nori, and A. V. Zayats. Spin-orbit interactions of light. *Nature Photon.*, 9(12):796–808, December 2015.

[53] Ling Lu, John D. Joannopoulos, and Marin Soljacic. Topological states in photonic systems. *Nat. Phys.*, 12(7):626–629, July 2016.

[54] Neil W. Ashcroft and N. David Mermin. *Solid State Physics*. Brooks Cole, New York, 1 edition edition, January 1976.

[55] Roald Winlker. *Spin-orbit Coupling Effects in Two-Dimensional Electron and Hole Systems*. Springer, Berlin ; New York, 2003 edition edition, December 2003.

[56] R. Shankar. *Principles of Quantum Mechanics*. Springer, New York, 1994. corr. 2nd edition edition, February 2008.

[57] Lukas Novotny and Bert Hecht. *Principles of Nano-Optics*. Cambridge University Press, Cambridge, 2 edition edition, November 2012.

[58] John D. Joannopoulos, Steven G. Johnson, Joshua N. Winn, and Robert D. Meade. *Photonic Crystals: Molding the Flow of Light, Second Edition*. Princeton University Press, Princeton, second edition edition, March 2008.

[59] Steven G. Johnson and J. D. Joannopoulos. Block-iterative frequency-domain methods for Maxwells equations in a planewave basis. *Opt. Express*, 8(3):173–190, January 2001.

[60] Mildred S. Dresselhaus, Gene Dresselhaus, and Ado Jorio. *Group Theory: Application to the Physics of Condensed Matter*. Springer, Berlin, 2008 edition edition, December 2007.

[61] Teturo Inui, Yukito Tanabe, and Yositaka Onodera. *Group Theory and Its Applications in Physics*. Springer Series in Solid-State Sciences. Springer-Verlag, Berlin Heidelberg, 1990.

[62] Jeffrey C. Y. Teo, Liang Fu, and C. L. Kane. Surface states and topological invariants in three-dimensional topological insulators: Application to Bi1-xSbx. *Physical Review B*, 78(4):045426, July 2008.

[63] Liang Fu. Topological Crystalline Insulators. *Physical Review Letters*, 106(10):106802, March 2011.

[64] Yoichi Ando and Liang Fu. Topological Crystalline Insulators and Topological Superconductors: From Concepts to Materials. *Annual Review of Condensed Matter Physics*, 6(1):361–381, March 2015.

[65] Timothy H. Hsieh, Hsin Lin, Junwei Liu, Wenhui Duan, Arun Bansil, and Liang Fu. Topological crystalline insulators in the SnTe material class. *Nature Communications*, 3:ncomms1969, July 2012.

[66] F. D. M. Haldane and S. Raghu. Possible Realization of Directional Optical Waveguides in Photonic Crystals with Broken Time-Reversal Symmetry. *Phys. Rev. Lett.*, 100(1):013904, January 2008.

[67] Alexander B. Khanikaev, S. Hossein Mousavi, Wang-Kong Tse, Mehdi Kargarian, Allan H. MacDonald, and Gennady Shvets. Photonic topological insulators. *Nat Mater*, 12(3):233–239, 2013.

[68] Tomoki Ozawa, Hannah M. Price, Alberto Amo, Nathan Goldman, Mohammad Hafezi, Ling Lu, Mikael Rechtsman, David Schuster, Jonathan Simon, Oded Zilberberg, and Iacopo Carusotto. Topological Photonics. *arXiv:1802.04173*, February 2018.

[69] Gerald Schubert, Holger Fehske, Lars Fritz, and Matthias Vojta. Fate of topological-insulator surface states under strong disorder. *Physical Review B*, 85(20):201105, May 2012.

[70] David Soriano, Frank Ortmann, and Stephan Roche. Three-Dimensional Models of Topological Insulators: Engineering of Dirac Cones and Robustness of the Spin Texture. *Physical Review Letters*, 109(26):266805, December 2012.

[71] Vincent Sacksteder, Tomi Ohtsuki, and Koji Kobayashi. Modification and Control of Topological Insulator Surface States Using Surface Disorder. *Physical Review Applied*, 3(6):064006, June 2015.

[72] Pedram Roushan, Jungpil Seo, Colin V. Parker, Y. S. Hor, D. Hsieh, Dong Qian, Anthony Richardella, M. Z. Hasan, R. J. Cava, and Ali Yazdani. Topological surface states protected from backscattering by chiral spin texture. *Nature*, 460(7259):1106–1109, August 2009.

[73] Sungjae Cho, Brian Dellabetta, Ruidan Zhong, John Schneeloch, Tiansheng Liu, Genda Gu, Matthew J. Gilbert, and Nadya Mason. Aharonov-Bohm oscillations in a quasi-ballistic three-dimensional topological insulator nanowire. *Nat. Commun.*, 6:7634, July 2015.

[74] Liang Fu, C. L. Kane, and E. J. Mele. Topological Insulators in Three Dimensions. *Phys. Rev. Lett.*, 98(10):106803, March 2007.

[75] Naunidh Virk and Oleg V. Yazyev. Dirac fermions at high-index surfaces of bismuth chalcogenide topological insulator nanostructures. *Scientific Reports*, 6:20220, February 2016.

[76] Chao-Xing Liu, Xiao-Liang Qi, HaiJun Zhang, Xi Dai, Zhong Fang, and Shou-Cheng Zhang. Model Hamiltonian for topological insulators. *Phys. Rev. B*, 82(4):045122, July 2010.

[77] Wen-Yu Shan, Hai-Zhou Lu, and Shun-Qing Shen. Effective continuous model for surface states and thin films of three-dimensional topological insulators. *New Journal of Physics*, 12(4):043048, 2010.

[78] Gerd Bergmann. Physical interpretation of weak localization: A time-of-flight experiment with conduction electrons. *Physical Review B*, 28(6):2914–2920, September 1983.

[79] Adam C. Durst. Disorder-induced density of states on the surface of a spherical topological insulator. *Physical Review B*, 93(24):245424, June 2016.

[80] G. Siroki, D. K. K. Lee, P. D. Haynes, and V. Giannini. Single-electron induced surface plasmons on a topological nanoparticle. *Nat. Commun.*, 7:12375, August 2016.

[81] Virk, Naunidh Singh. Phd thesis: A Theoretical Investigation of Topological Insulator Nanostructures. 2016.

[82] Arijit Kundu, Alex Zazunov, Alfredo Levy Yeyati, Thierry Martin, and Reinhold Egger. Energy spectrum and broken spin-surface locking in topological insulator quantum dots. *Phys. Rev. B*, 83(12):125429, March 2011.

[83] Patrick A. Lee and Daniel S. Fisher. Anderson Localization in Two Dimensions. *Physical Review Letters*, 47(12):882–885, September 1981.

[84] Hua Chen, Wenguang Zhu, Di Xiao, and Zhenyu Zhang. CO Oxidation Facilitated by Robust Surface States on Au-Covered Topological Insulators. *Physical Review Letters*, 107(5):056804, July 2011.

[85] Jianping Xiao, Liangzhi Kou, Chi-Yung Yam, Thomas Frauenheim, and Binghai Yan. Toward Rational Design of Catalysts Supported on a Topological Insulator Substrate. *ACS Catalysis*, 5(12):7063–7067, December 2015.

[86] J. M. Fitzgerald, P. Narang, R. V. Craster, S. A. Maier, and V. Giannini. Quantum Plasmonics. *Proceedings of the IEEE*, 104(12):2307–2322, December 2016.

[87] Vincenzo Giannini, Antonio I. Fernndez-Domnguez, Susannah C. Heck, and Stefan A. Maier. Plasmonic Nanoantennas: Fundamentals and Their Use in Controlling the Radiative Properties of Nanoemitters. *Chemical Reviews*, 111(6):3888–3912, June 2011.

[88] M. S. Tame, K. R. McEnery, K. zdemir, J. Lee, S. A. Maier, and M. S. Kim. Quantum plasmonics. *Nat Phys*, 9(6):329–340, June 2013.

[89] K. Rzzewski and R. W. Boyd. Equivalence of interaction hamiltonians in the electric dipole approximation. *J Mod Opt*, 51(8):1137–1147, May 2004.

[90] D. Bauer, D. B. Miloevi, and W. Becker. Strong-field approximation for intense-laser atom processes: The choice of gauge. *Phys. Rev. A*, 72(2):023415, August 2005.

[91] Michael Klaiber, Karen Z. Hatsagortsyan, and Christoph H. Keitel. Gauge-invariant relativistic strong-field approximation. *Phys. Rev. A*, 73(5):053411, May 2006.

[92] E. Prodan, C. Radloff, N. J. Halas, and P. Nordlander. A Hybridization Model for the Plasmon Response of Complex Nanostructures. *Science*, 302(5644):419–422, October 2003.

[93] Shin-ichi Uchida, Setsuko Tajima, Atsushi Masaki, Shunji Sugai, Koichi Kitazawa, and Shoji Tanaka. Infrared Phonons in Semiconducting Phase of BaPb1-xBixO3. *J. Phys. Soc. Jpn.*, 54(11):4395–4409, November 1985.

[94] S. Tajima, S. Uchida, A. Masaki, H. Takagi, K. Kitazawa, S. Tanaka, and A. Katsui. Optical study of the metal-semiconductor transition in BaPb(1-x)BixO3. *Phys. Rev. B*, 32(10):6302–6311, November 1985.

[95] D. E. Cox and A. W. Sleight. Crystal structure of Ba2Bi3+Bi5+O6. *Solid State Communications*, 19(10):969–973, August 1976.

[96] Eli Yablonovitch. Inhibited Spontaneous Emission in Solid-State Physics and Electronics. *Phys. Rev. Lett.*, 58(20):2059–2062, May 1987.

[97] Sajeev John. Strong localization of photons in certain disordered dielectric superlattices. *Phys. Rev. Lett.*, 58(23):2486–2489, June 1987.

[98] Emil Prodan and Camelia Prodan. Topological Phonon Modes and Their Role in Dynamic Instability of Microtubules. *Phys. Rev. Lett.*, 103(24):248101, December 2009.

[99] Alexander B. Khanikaev, Romain Fleury, S. Hossein Mousavi, and Andrea Al. Topologically robust sound propagation in an angular-momentum-biased graphene-like resonator lattice. *Nat. Commun.*, 6:8260, October 2015.

[100] Cheng He, Xu Ni, Hao Ge, Xiao-Chen Sun, Yan-Bin Chen, Ming-Hui Lu, Xiao-Ping Liu, and Yan-Feng Chen. Acoustic topological insulator and robust one-way sound transport. *Nat. Phys.*, 12(12):1124–1129, 2016.

[101] N. Goldman, G. Juzeliunas, P. Ohberg, and I. B. Spielman. Light-induced gauge fields for ultracold atoms. *Rep. Prog. Phys.*, 77(12):126401, 2014.

[102] Joel Yuen-Zhou, Semion K. Saikin, Tony Zhu, Mehmet C. Onbasli, Caroline A. Ross, Vladimir Bulovic, and Marc A. Baldo. Plexciton Dirac points and topological modes. *Nat. Commun.*, 7:11783, June 2016.

[103] Dafei Jin, Thomas Christensen, Marin Soljai, Nicholas X. Fang, Ling Lu, and Xiang Zhang. Infrared Topological Plasmons in Graphene. *arXiv:1702.02553*, February 2017.

[104] Deng Pan, Rui Yu, Hongxing Xu, and F. Javier Garca de Abajo. Topologically protected Dirac plasmons in graphene. *arXiv:1702.00036*, January 2017.

[105] A.V. Nalitov, D.D. Solnyshkov, and G. Malpuech. Polariton z Topological Insulator. *Phys. Rev. Lett.*, 114(11):116401, March 2015.

[106] A. Slobozhanyuk, A. V. Shchelokova, X. Ni, S. H. Mousavi, D. A. Smirnova, P. A. Belov, A. Al, Y. S. Kivshar, and A. B. Khanikaev. Near-field imaging of spin-locked edge states in all-dielectric topological metasurfaces. *arXiv:1705.07841*, May 2017.

[107] M. T. Homer Reid and S. G. Johnson. Efficient Computation of Power, Force, and Torque in BEM Scattering Calculations. *ArXiv e-prints*, July 2013.

[108] Ardavan F. Oskooi, David Roundy, Mihai Ibanescu, Peter Bermel, J. D. Joannopoulos, and Steven G. Johnson. Meep: A flexible free-software package for electromagnetic simulations by the FDTD method. *Comput. Phys. Commun.*, 181(3):687–702, March 2010.

[109] Z. F. Wang, Li Chen, and Feng Liu. Tuning Topological Edge States of Bi(111) Bilayer Film by Edge Adsorption. *Nano Letters*, 14(5):2879–2883, May 2014.

[110] Yuting Yang, Yun Fei Xu, Tao Xu, Hai-Xiao Wang, Jian-Hua Jiang, Xiao Hu, and Zhi Hong Hang. Visualization of unidirectional optical waveguide using topological photonic crystals made of dielectric material. *arXiv:1610.07780*, October 2016.